MAGNETOM Flash

The Magazine of MR

Issue Number 2/2010
CMR Edition
Not for distribution in the US.

SIEMENS

Clinical

How-I-do-it

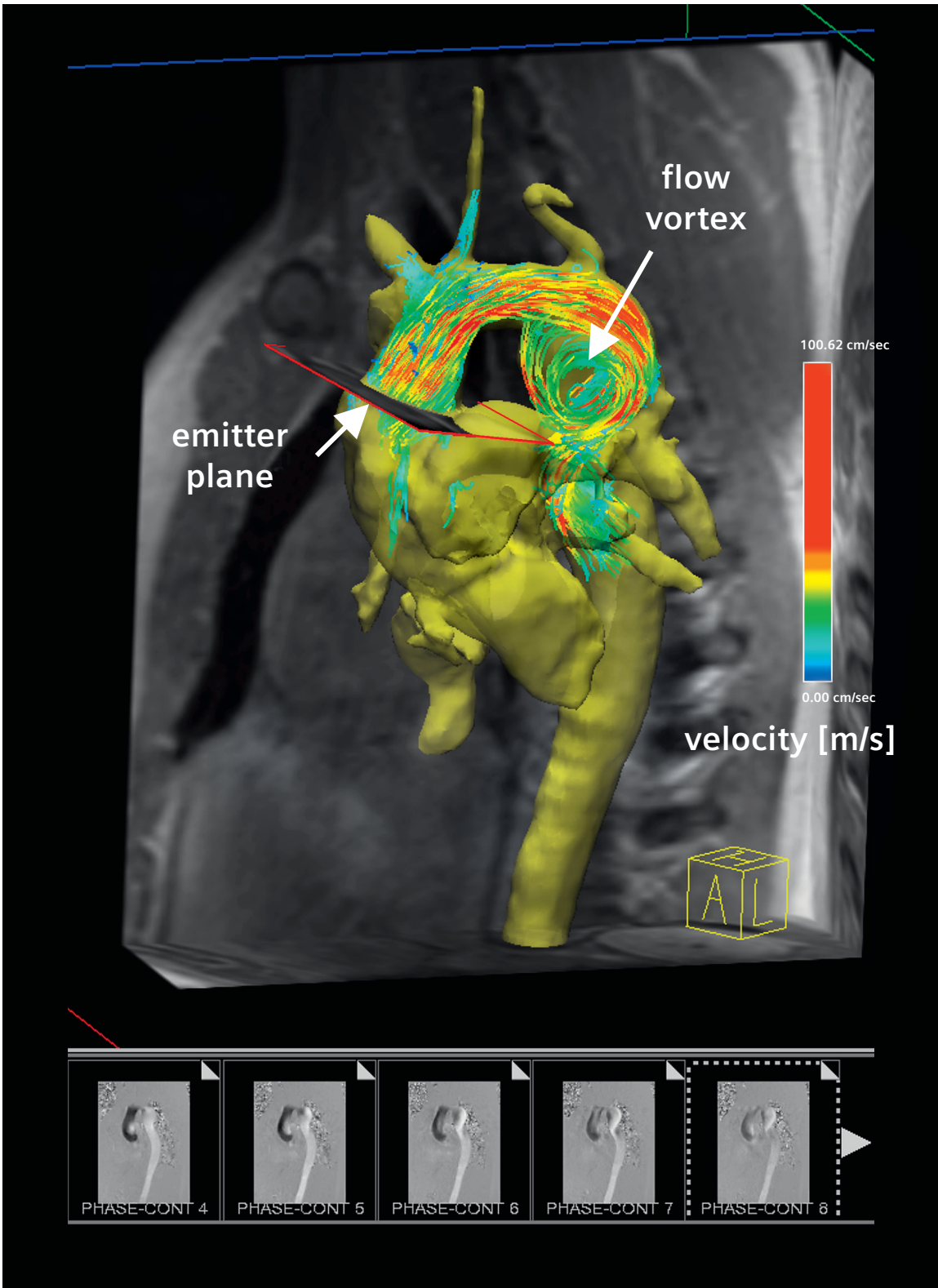

Matthias Lichy, M.D.

Dear MAGNETOM user,

Even before the introduction of MR imaging, the visualization of vessels was an integral part of the daily routine of a radiology department. Since MRI, however – compared to conventional DSA or CTA – we can now acquire detailed information about the vessels without the need to expose the patient to radiation. And by dispensing with previously undertaken interventions we can thereby avoid their associated risks.

It's true that radiation-free (and also contrast-media free) assessment of the vessels can easily be performed with ultrasound. However, its high dependency on the experience of the performing physician, compromised diagnostic accuracy for certain regions of the body (and clinical condition e.g. after surgical intervention), and its limitations in evaluating large areas of interest within a short timeframe do compromise its clinical usability. With the introduction of the Tim technology, MRI is now able to scan the vessels over large areas of interest or even as a whole-body scan, reflecting the systemic aspect of most cardiovascular diseases and – more importantly – with the highest diagnostic accuracy. Furthermore, all this information can be assessed within the shortest examination time and one single exam.

For most of our older patients, however, radiation exposure is only a relative threat. On the other hand, the impairment of renal function in this patient cohort and other practical issues have led to MRI using new imaging techniques to provide highest contrast and best timing of the vessel filling with the lowest dosages of contrast media. These techniques, such as echo-sharing MRA sequences (*syngo* TWIST) not only allow a reduction in the amount of applied contrast media but can also be used to provide detailed temporal information. The combination of high temporal and spatial resolution without the need for a risky intervention and radiation exposure is perhaps the most appealing aspect of such an imaging technique and is one of the reasons why temporal resolved MRA is nowadays playing an increasingly important role in, for example, therapy planning in cases of peripheral vessel disease, assessment of vessel malformations, detailed understanding of tumor perfusion and vessel supply. This issue of MAGNETOM Flash offers you an insight into ongoing developments in imaging aspects of vessel diseases e.g. the evaluation of haemodynamics.

We have yet to mention the biggest advantage of MRI: its ability to provide information about the tissue itself and its functional state e.g. for evaluation of brain damage in case of stroke or heart muscle viability in case of coronary artery disease. This is beyond what any other clinically available imaging method can achieve.

One important focus of this issue is the practical implementation of cardiac MRI. Back in 2007 we reported about the current clinical status of cardiac MRI and distributed the recommended protocols of the Society of Cardiovascular Magnetic Resonance for your MR scanner. This latest issue contains an update of these protocols for the syngo MR B17 and also a selection of new clinical information which will surely influence our daily routine in cardiac imaging.

Matthias Lichy, M.D.

The Editorial Team

We appreciate your comments.
Please contact us at magnetomworld.med@siemens.com

Antje Hellwich
Associate Editor

Okan Ekinci, M.D.
Center of Clinical Competence – Cardiology, Erlangen, Germany

Peter Kreisler, Ph.D.
Collaborations & Applications, Erlangen, Germany

Heike Weh,
Clinical Data Manager, Erlangen, Germany

Bernhard Baden,
Clinical Data Manager, Erlangen, Germany

Ignacio Vallines, Ph.D.,
Applications Manager, Erlangen, Germany

Wellesley Were
MR Business Development Manager
Australia and New Zealand

Milind Dhamankar, M.D.
Sr. Director, MR Product Marketing, Malvern, USA

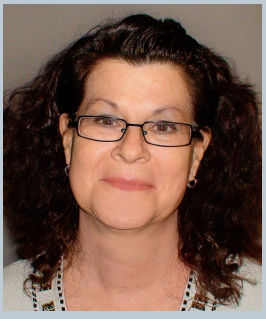

Michelle Kessler, US
Installed Base Manager, Malvern, PA, USA

Gary R. McNeal, MS (BME)
Advanced Application Specialist, Cardiovascular MR Imaging
Hoffman Estates, USA

Dr. Sunil Kumar S.L.
Senior Manager Applications, Canada

Content

Content

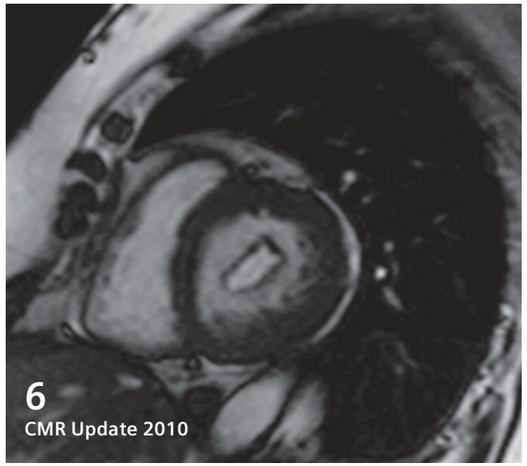

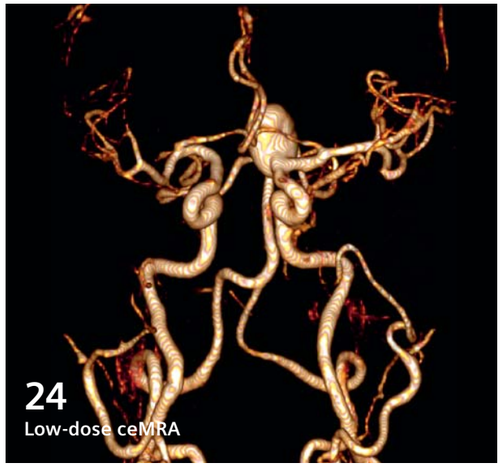

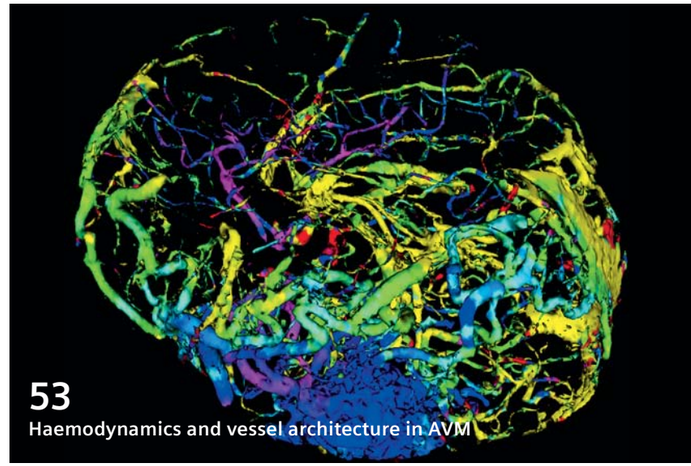

Further clinical information

Visit the MAGNETOM World Internet pages at **www.siemens.com/magnetom-world** for further clinical information and talks by international experts.
Here you will find application tips such as positioning videos, short videos on software applications, case reports, protocols and much more.
From basic MRI information up to research there is relevant clinical information right at your fingertips.

Clinical Cardiovascular MRI

Clinical Abdomen/Pelvis

Clinical → How I do it

Cardiovascular Magnetic Resonance – Update 2010

A Selection of Interesting new Data

Florian von Knobelsdorff-Brenkenhoff, M.D.; Jeanette Schulz-Menger, M.D.

Experimental and Clinical Research Center, Medical University Berlin, Charité Campus Buch and HELIOS Klinikum Berlin Buch, Dept. of Cardiology and Nephrology, Berlin, Germany

The CMR issue of MAGNETOM Flash (no. 36, 2007) is available online at www.siemens.com/magnetom-world (International version, select MAGNETOM Flash under Publications in the upper left-hand corner)

Introduction

In 2007, MAGNETOM Flash devoted a complete issue (#36) to Cardiovascular Magnetic Resonance Imaging (CMR). Since then, the acceptance of CMR as a unique and valuable imaging tool in clinical cardiology and research has further increased. Very recently, large international societies launched an update of the expert consensus document on CMR that provides a perspective on the current state of this evolving technique [1]. Furthermore, attempts to standardise CMR training, protocols, examinations and reports have been published within the last years to achieve a homogeneous high-level of diagnostic testing world-wide [2, 3, 4]. Moreover, a large German registry including about 11,000 CMR studies underlined that the information gained by CMR has strong impact on patient management [5]. Finally, more and more data regarding the prognostic impact of CMR are published [6].
Many innovations have entered clinical routine, and many more ideas are looming on the (pre-)clinical horizon. It would be beyond the scope of the present article to deal with all the news in all the various CMR fields since 2007 (we recommend an excellent recently-published review article [7]). Rather, we intend to give a short overview of some important highlights and studies, and to touch on some fascinating future trends that may further emphasize the significance of CMR over the next few years.

News on cardiac chamber quantification

Whereas the assessment and quantification of ventricular function has not significantly changed since MAGNETOM Flash #36, new and more detailed normal-values have been published during recent years. Particularly, normal values for children were missing, even though the interest and the need for CMR in children were growing. In 2009, Buechel et al. published left and right ventricular parameters in 50 children [8]. Sarikouch et al. showed gender differences when normalized for height or body surface area in a group of 114 healthy children and adolescents [9]. In our own experience, the number of referred adolescents from thoracic surgery (e.g. in case of pectus excavatum) or for the assessment of the right ventricle (e.g. mucoviscidosis) is growing due to frequently impaired ultrasound conditions. Investigations of young patients are underlining the need for fast and robust CMR protocols and reliable post-processing and interpretation. Finally, it should be stressed that whenever normal values are applied, the user must consider that they should have been obtained with the same CMR protocol that is applied in the user's institution.

News on ischemic heart disease

CMR stress testing

CMR stress tests, both using the analysis of first-pass perfusion during adenosine infusion, and of wall motion abnormalities during dobutamine infusion, have entered clinical routine and are nowadays accepted as very accurate methods (also see a state-of-the-art paper regarding perfusion imaging [10]). The imaging techniques and protocols are widely unchanged from those described in the articles by Markus Jochims et al. and by Andrea Arai in MAGNETOM Flash #36. However, important data regarding the diagnostic performance and the prognostic implication have been published since then. Nandalur et al. published a large meta-analysis in 2007 including 1516 patients with perfusion imaging and 754 patients with wall motion abnormality imaging. They found a sensitivity/specificity of 91% / 81% and 83% / 86%, respectively, to detect relevant coronary artery stenosis on a patient level [11].
Moreover, in 2008 Schwitter et al. published the first multi-centre multi-vendor study comparing CMR stress perfusion imaging with SPECT (single-photon emission computed tomography) stress perfusion imaging (called "MR-IMPACT"). This important study demonstrated that CMR is either equivalent or superior to SPECT regarding the diagnostic accuracy to detect coronary artery stenosis ≥50% assessed by invasive coronary angiography [12].
Regarding CMR stress perfusion imaging, most studies had excluded patients with coronary artery bypass grafts due to potentially altered myocardial contrast kinetics owing to more complex myocardial perfusion and different distances of the contrast bolus through different bypasses and native coronary vessels. Recently, two larger studies demonstrated that even for patients after surgical revascularization, stress perfusion CMR yields good diagnostic accuracy for the detection and localization of significant stenoses, even though sensitivity is reduced compared with published data in patients without coronary bypass [13, 14].
Regarding the prognostic impact of CMR stress testing, Jahnke et al. reported that the 3-year event-free survival was 99.2% for patients with normal stress CMR (both adenosine and dobutamine) and 83.5% for those with abnormal tests. Univariate analysis showed ischemia identified by CMR to be predictive of cardiac events (hazard ratio 12.5) [15].
The addition of late gadolinium enhancement (LGE) imaging to stress perfusion further improves the risk stratification for patients with symptoms of ischemia. Steel et al. showed that the presence of a perfusion deficit or myocardial scar both maintained a >3-fold association with cardiac death or acute myocardial infarction, whereas in patients without a history of myocardial infarction, who had negative stress CMR, LGE presence was associated with a >11-fold hazards increase in death and myocardial infarction [16].
CMR stress testing can be regarded as a very safe method. In 3474 stress tests (both adenosine and dobutamine) included in the German CMR registry, only five severe (defined as death, resuscitation, or any other condition related to the CMR procedure that required monitoring as an inpatient for at least 1 night after the CMR scan) adverse events occurred (0.14%). These data are in the range of other stress imaging modalities, like dobutamine stress echocardiography (potentially life-threatening complications in 0.2% in a recent review [17]).
The differentiation of true perfusion defects and dark-rim artefacts during CMR stress testing is still sometimes challenging. Apart from using interpretation algorithms – such as proposed by the team from the Duke University [18] – one future solution to facilitate the correct diagnosis may be the use of novel accelerated high spatial-resolution imaging techniques, and the step towards higher B_0 field strength, like 3T [19, 20]. Thus, future innovations are expected to further increase the diagnostic accuracy of CMR stress testing and promote its widespread use in clinical routine.

CMR in acute myocardial infarction

CMR has also obtained an important role in patients with acute myocardial infarction. Recent review articles summarized

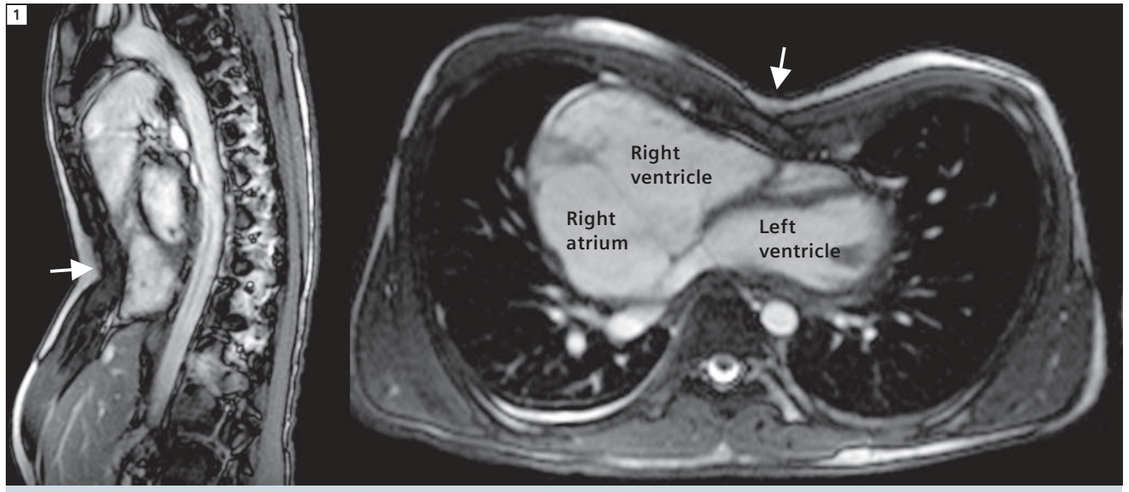

1 A 21-year-old man was referred to CMR before elective surgical correction of severe pectus excavatum. CMR illustrated the pectus excavatum (white arrows). Furthermore, it newly detected right heart enlargement and severe tricuspid regurgitation due to tricuspid prolapse. The patient underwent concomitant tricuspid valve repair and sternal correction.

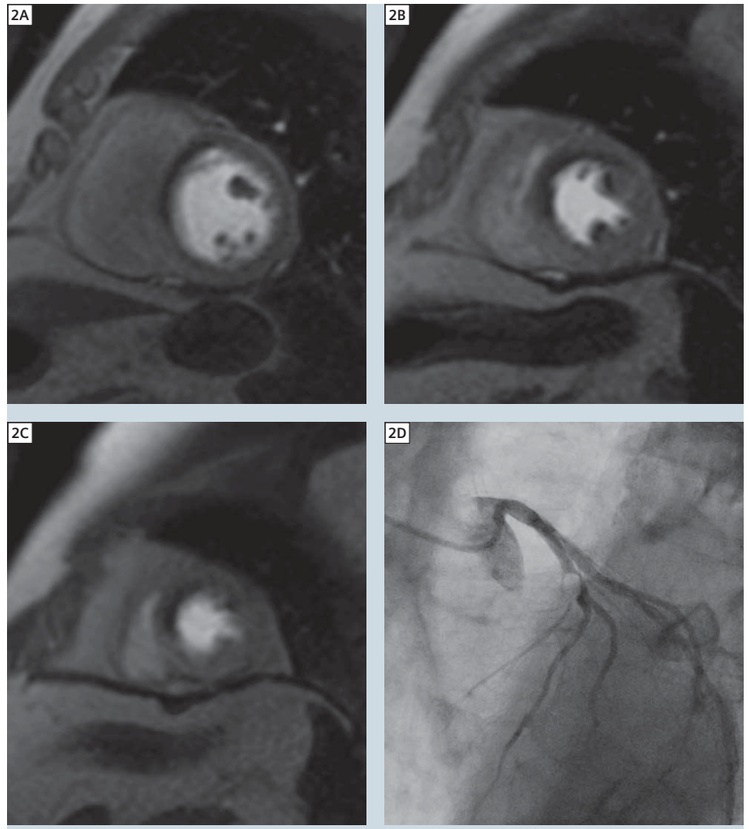

2A–D A 59-year-old man complained about dyspnoea and chest pain after mild physical exertion. CMR with adenosine stress perfusion showed a perfusion deficit predominantly in the septum **(2A–C)**. Coronary angiography revealed a significant stenosis of the left anterior descending coronary artery **(2D)**, which was treated by stent implantation.

the capabilities of CMR in acute coronary syndrome [21], and in myocardial infarction in general [22]. Apart from demonstrating motion abnormalities of the infarcted wall with high blood-tissue contrast for all 17 left ventricular segments in standardized planes, CMR provides novel information about the tissue alterations during acute myocardial infarction by use of T2 and T1-weighted imaging.
T1-weighted imaging: late enhancement imaging after intravenous administration of gadolinium contrast depicts irreversibly injured tissue. The principles and the imaging technique (segmented inversion recovery TurboFlash) are still widely unchanged from the report by Igor Klem in MAGNETOM Flash #36. The technique is commonly regarded as robust, very accurate and observer-independent for the detection of infarction in both the acute and chronic setting; this has recently been confirmed in a large multi-centre study [23].
T2-weighted imaging: Abdel-Aty et al. recently gave the evidence in an animal model that T2-weighted imaging of edema detects acute ischemic myocyte injury before the onset of irreversible injury [24]. The bright area in T2-weighted imaging represents the area-at-risk during myocardial infarction. By combining T2-weighted imaging with LGE, CMR offers the unique possibility to depict both reversible and irreversible injury with very high sensitivity and specificity. This allows for quantifying the extent of the salvaged area after revascularization as an important parameter for clinical decision making and research [25].
By using these techniques, Francone et al. demonstrated that in patients with ST-elevation myocardial infarction (STEMI) treated with primary percutaneous coronary intervention, the time to reperfusion determines the extent of reversible and irreversible myocardial injury. In particular, salvaged myocardium was markedly reduced when reperfusion occurred >90 min of coronary occlusion [26]. Eitel et al. showed that the so-called myocardial salvage index, which is calculated as area at risk minus infarct size divided by the area at risk, predicts the outcome in acute reperfused STEMI [27]. Even in patients with N(non)-STEMI, T2-weighted imaging seems to add prognostic information. In a study by Raman et al., patients with edema showed a higher hazard of a cardiovascular event or death within 6 months compared with those without edema [28]. T2-weighted imaging has also been introduced as a method to assess the presence of myocardial haemorrhage, visible as hypointense core within the hyperintense edema. In a study by Ganame et al., myocardial haemorrhage was an independent predictor of adverse left ventricular remodelling at four months, independent of the initial infarct size [29]. The presence of microvascular obstruction, visible as hypointense core within the bright zones of LGE, or by early gadolinium enhancement imaging at 1 to 2 minutes after injection, has also turned out to be a marker for unfavourable cardiac remodelling and prognosis. Nijveldt et al. showed that in patients after revascularized acute myocardial infarction, the presence or absence of microvascular obstruction proved a more powerful predictor of global and regional functional recovery than other characteristics like TIMI flow grade, myocardial blush grade, ST-segment resolution and even infarct size and transmural extent as assessed by CMR [30].
In addition, studies investigated the value of CMR in emergency patients. Here, T2-weighted imaging seems to be helpful in patients presenting with acute chest pain to the emergency room to decide whether coronary angiography should be performed or not [31]. Finally, CMR has been proven to be a valuable tool to identify the underlying disease in patients presenting with acute coronary syndrome, but exhibit normal coronary arteries during heart catheterization – this is a non-trivial proportion of up to 10% of patients initially diagnosed with STEMI, and 32% with acute coronary syndrome [22]. CMR helps to find the correct diagnosis: some suffer from Takotsubo cardiomyopathy with its typical reversible wall motion abnormalities and the absence of LGE; some have myocarditis with its typical subepicardial and intramural LGE lesions, and some exhibit LGE lesions fitting to myocardial infarction, possibly indicating spontaneous lysis [32, 33].

3A–E A 67-year-old man with known coronary artery disease presented with acute chest pain. Three years ago, stents were inserted into the left anterior descending, a marginal branch, and the right coronary artery. Coronary angiography revealed late stent thrombosis with occluded left anterior descending artery **(3A)**, which was treated by emergent percutaneous coronary intervention. After two days, CMR was performed, showing corresponding wall motion abnormalities on SSFP cine images, regional edema and wall thickening on T2-weighted images **(3B–C)**, and LGE with microvascular obstruction on T1-weighted images after contrast media administration **(3D–E)**.

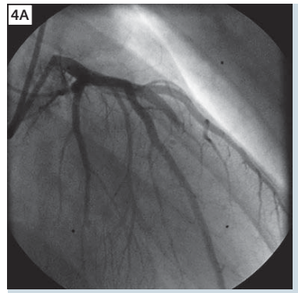

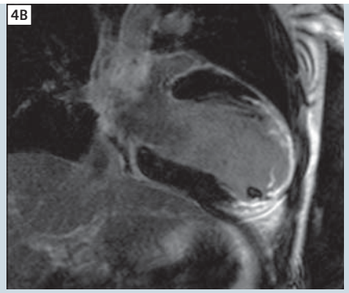

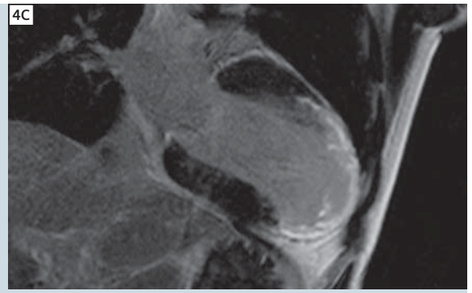

4A–C A 27-year-old man presented 5 years after severe embolic myocardial infarction during aortic endocarditis. Two-chamber view with LGE technique depicted transmural scarring of the anterior wall and the apex and an apical thrombus. Two months following oral anticoagulation, the thrombus had disappeared.

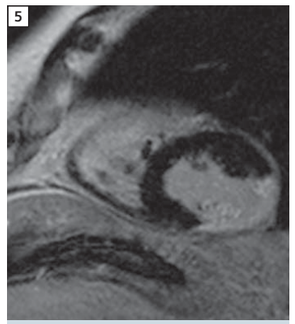

5 A 69-year-old man with chronic myocardial infarction and moderate mitral regurgitation. LGE imaging showed transmural infarction of the lateral wall with total scarring of the inferoseptal papillary muscle.

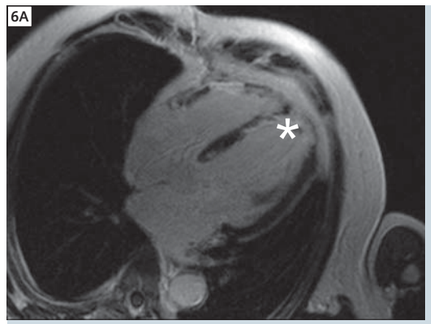

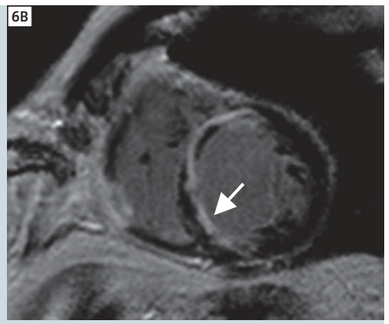

6A–B A 70-year-old man with ischemic cardiomyopathy after anterior and posterior infarction underwent CMR. LGE imaging showed extensive myocardial scarring, including the free wall of the right ventricle (arrow). Furthermore, a thrombus in the left ventricle is visible (asterisk).

CMR in chronic myocardial infarction

In chronic myocardial infarction the importance of CMR is mainly based on the LGE imaging sequence. The prediction of functional recovery in ischemic disease by CMR via assessing the transmurality of LGE has widely replaced dobutamine echocardiography and nuclear medicine and become accepted as the clinical gold standard [34]. Given that quantification of infarct size by LGE is highly reproducible, this technique provides a useful surrogate end point for clinical trials comparing various infarction therapies [22, 35].

The association of myocardial scar detected by LGE and increased mortality has already been reported in 2006 by Kwong et al. The mere presence of scar resulting from myocardial infarction conferred nearly a 6-fold increased risk for major cardiac events – even if only about 1% of the left ventricle is affected [36, 37]. The more scar, the higher the risk for major cardiac adverse events: Kwon et al. found that in patients with ischemic cardiomyopathy and severely reduced ejection fraction, a greater extent of myocardial scar, delineated by LGE CMR, was associated with increased mortality [38]. Furthermore, the composition of LGE seems to influence the incidence of ventricular arrhythmia and prognosis in general following myocardial infarction. Roes et al. performed a contrast-enhanced CMR study in patients with ischemic cardiomyopathy before ICD implantation and determined the infarct core, total infarct size and the infarct gray zone, which is an admixture of viable and nonviable myocytes, calculated as total infarct size minus infarct core, and is regarded as a measure of infarct tissue heterogeneity. The latter was the strongest predictor of spontaneous ventricular arrhythmia with subsequent ICD therapy (as surrogate of sudden cardiac death) among other clinical and CMR variables [39]. Similar results were reported by Schmidt et al. regarding enhanced susceptibility to programmed electrical stimulation [40]. In addition, papillary muscles that lie within an infarct zone might give rise to ventricular

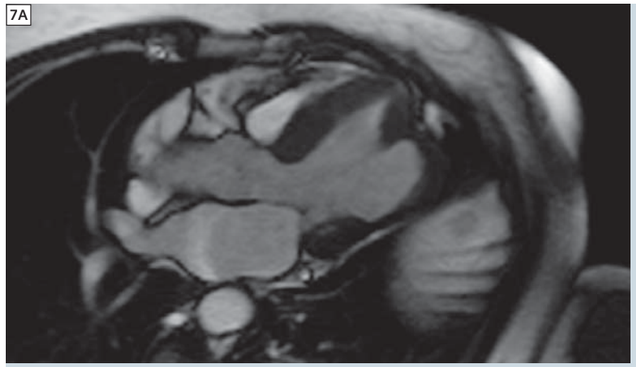

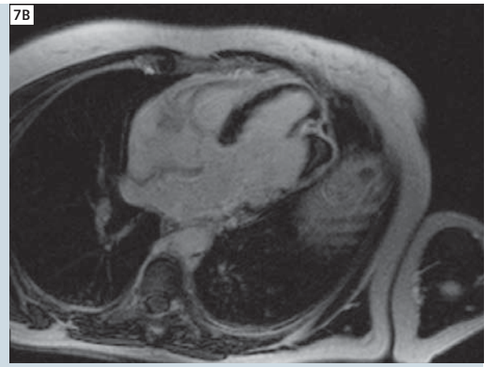

7A–B A 65-year-old woman complained of chest pain, which started quite strongly two years before, and since then appeared repeatedly during exertion. CMR showed a large aneurysm of the inferolateral wall **(7A)**. LGE imaging **(7B)** depicted thrombotic material in the aneurysm, which is identified less clear by SSFP **(7A)**.

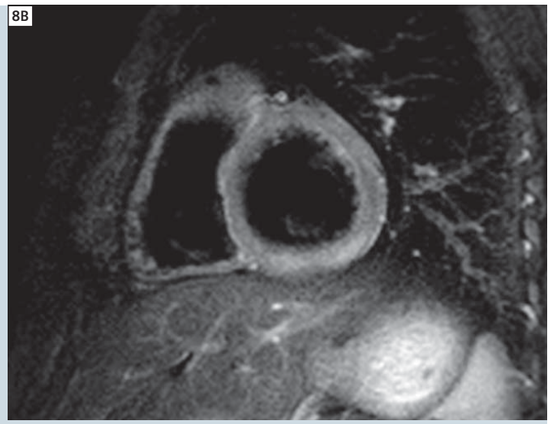

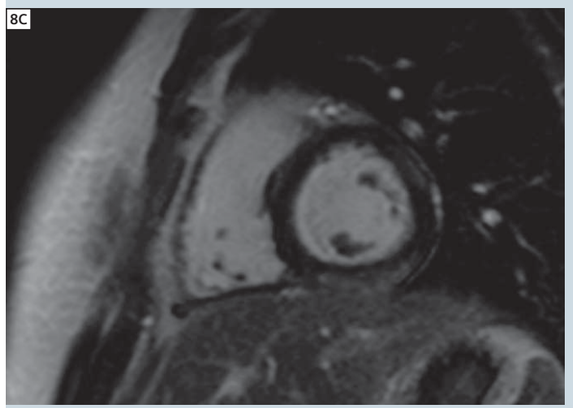

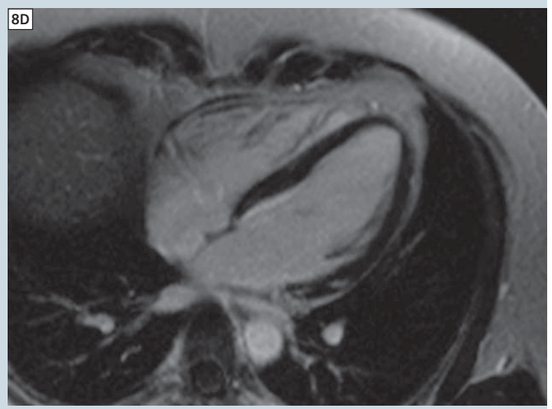

8 A 23-year-old subject presented with severe chest pain and ST-elevation in all leads, but no risk-factors for coronary artery disease. The immediately performed CMR showed a typical pattern for acute myocarditis. **8A** Short axis SSFP in enddiastole. **8B** Short axis T2-weighted image. **8C** Short axis with late enhancement. **8D** Four-chamber view with late enhancement.

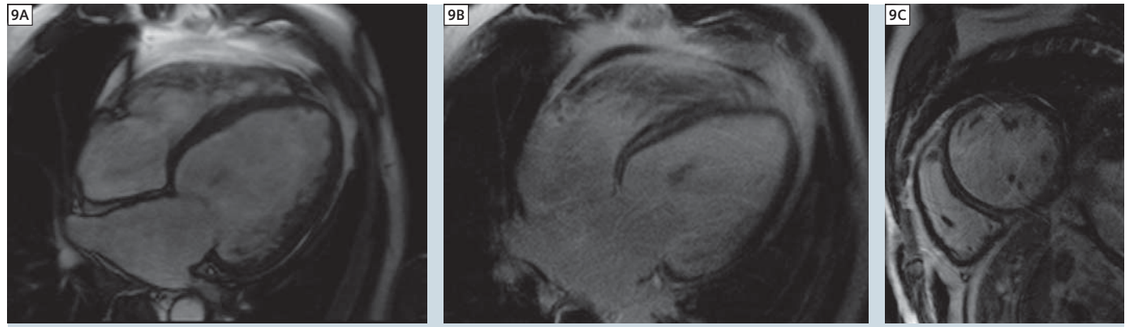

9 A 51-year-old man complained about dyspnea at mild exertion. CMR revealed a markedly dilated left ventricle with severely depressed systolic function on SSFP images **(9A)**. Late enhancement images **(9B, 9C)** depicted intramural fibrosis in the interventricular septum, indicating dilated cardiomyopathy.

arrhythmias. Bogun et al. reported that heterogeneous uptake of gadolinium might be predictive of arrhythmogenic papillary muscles [41]. Thus, LGE imaging can improve risk stratification following myocardial infarction and help to identify those subjects who benefit most from prophylactic ICD implantation. Finally, infarction of the papillary muscles detected by LGE is closely related to more severe left ventricular remodeling and functional mitral regurgitation [42], which may have impact on surgical valvular considerations.

News on non-ischemic heart disease

Although cardiomyopathies (CMP) account for a considerable proportion of heart failure cases, both, diagnosis and treatment as well as the management of these patients still remain challenging. CMR offers a comprehensive assessment of heart failure patients and is now the gold standard imaging technique to assess myocardial anatomy, regional and global function, and viability [43]. The method has the unique potential to differentiate myocardial injury and is expected to be of prognostic value. Therefore, a substantial number of papers (nearly 600 during the last 2 years) were published regarding CMR and non-ischemic CMP. The following paragraph can only highlight a minority.
LGE imaging is established in ischemic heart disease, and is playing an increasing role in the assessment of CMP. Due to the intrinsic properties of the method, LGE shows only focal fibrosis, whereas it is well-known from (patho-)physiology, that diffuse fibrosis plays an important role for disease progression. Flett et al. recently introduced an interesting new equilibrium approach, based on a contrast-infusion, to quantify diffuse fibrosis [44]. T2-weighted images provide useful incremental diagnostic and prognostic information in a variety of clinical settings associated with suspected acute myo cardial injury. A detailed review was given recently by Matthias Friedrich [45]. Especially the capability to differentiate reversible and irreversible injury by using T2-weighted images in combination with contrast-enhanced CMR underlines the unique possibility of CMR.
The impact of such a comprehensive approach could be shown for myocarditis [46]. Based on this comprehensive approach, consensus criteria to assess myocarditis by CMR (Lake-Louise-Criteria) were published in 2009 [47]. Myocardial injury could also be detected by using CMR in various inflammatory diseases and circumstances, like Churg-Strauss syndrome, Lupus erythematosus

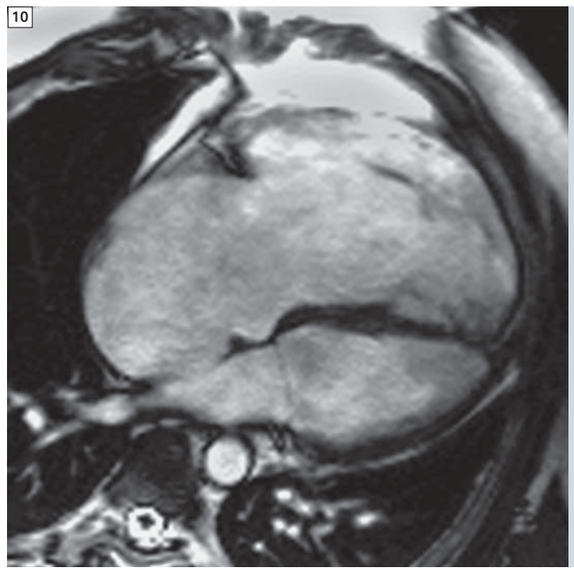

10 A 45-year-old man was referred to CMR with suspicion for ARVC due to enlargement of the right ventricle as assessed by echocardiography. Using CMR, right heart enlargement was confirmed. Interestingly, the diagnostic criteria for ARVC were not fulfilled in the 3D-assessment. The explanation for the right heart enlargement was a significant tricuspid insufficiency due to tricuspid valve prolapse. (4-chamber view, enddiastole, SSFP).

or following heart transplantation [48-50]. Moreover, there are first results that the combined use of CMR and endomyocardial biopsy yields a diagnostic synergy in troponine-positive patients with normal coronary arteries [51].
Dilated cardiomyopathy is one common cause for heart failure. Comprehensive noninvasive imaging combining CMR and PET (positron emission tomography) may give new insights into pathophysiology [52]. Furthermore, Hombach et al. reported that the cardiac index and right ventricular enddiastolic volume index derived from CMR provided prognostic impact for cardiac death in addition to QRS prolongation from conventional surface ECG and diabetes mellitus in patients with dilated cardiomyopathy. That finding underlines the impact of cine-based right ventricular quantification [53].
The three-dimensional quantification of the right ventricle is also a new, clearly defined criteria in the diagnostic guidelines for arrhythmogenic right ventricular cardiomyopathy (ARVC) published in 2010, whereas the CMR-driven tissue characterization failed to be included [54]. Nevertheless, there are different publications investigating the relation between scar-related right ventricular tachycardia and long-term outcome [55], underlining the need for a robust technique of LGE-sequences with fat-suppression, as recently described by Peter Kellman [56]. The systematic review of the phenotype will improve the understanding of the disease and will open the door to an earlier diagnosis also in case of relatives [57].
A large amount of papers discuss the differentiation of left-ventricular hypertrophy using CMR with the focus on hypertrophic cardiomyopathy (HCM). It is well-known that LGE already occurs in asymptomatic HCM-patients. However, such focal findings are also present in patients with other types of left ventricular hypertrophy and normal coronary arteries, like arterial hypertension, aortic stenosis or Fabry's disease [58]. A different pattern of LGE is described in patients with increased left ventricular mass caused by amyloidosis. Thereby, the gadolinium kinetics seems to reflect the severity of the cardiac amyloid burden [59].
Regarding HCM, Rubinstein et al. demonstrated that LGE was more prevalent in gene-positive HCM-patients. Furthermore, they found a strong association between LGE and surrogates of arrhythmia [60]. Several other studies demonstrated a correlation between the presence of LGE and mortality [61]. O'Hanlon et al. recently reported that HCM-patients with LGE have a higher mortality due

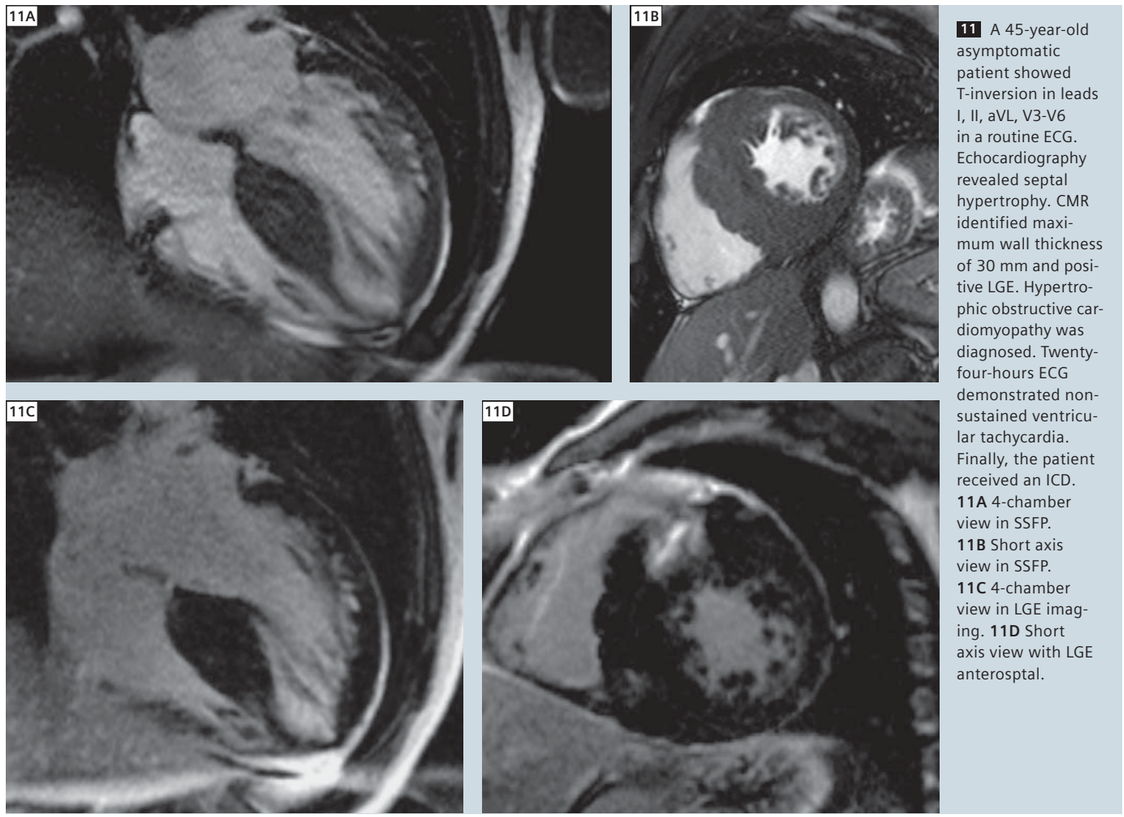

11 A 45-year-old asymptomatic patient showed T-inversion in leads I, II, aVL, V3-V6 in a routine ECG. Echocardiography revealed septal hypertrophy. CMR identified maximum wall thickness of 30 mm and positive LGE. Hypertrophic obstructive cardiomyopathy was diagnosed. Twenty-four-hours ECG demonstrated non-sustained ventricular tachycardia. Finally, the patient received an ICD. **11A** 4-chamber view in SSFP. **11B** Short axis view in SSFP. **11C** 4-chamber view in LGE imaging. **11D** Short axis view with LGE anterosptal.

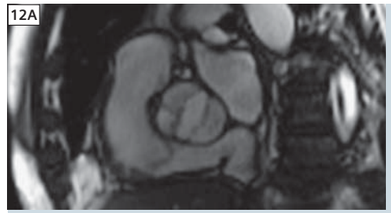

12A Bicuspid aortic valve (SSFP cine in systole).

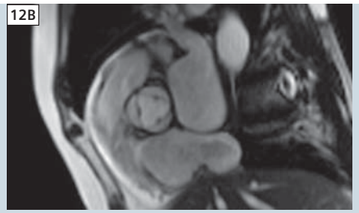

12B Tricuspid aortic valve with prominent Noduli arantii (SSFP cine in systole).

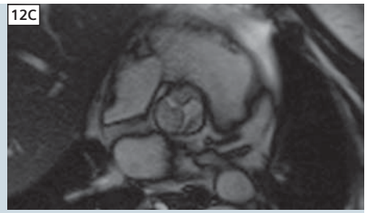

12C Mild aortic stenosis (SSFP cine in systole).

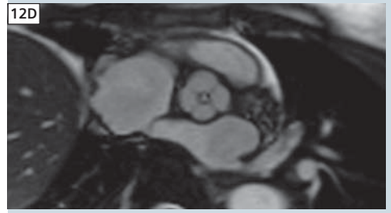

12D Quadricuspid aortic valve with central regurgitation (SSFP cine in diastole).

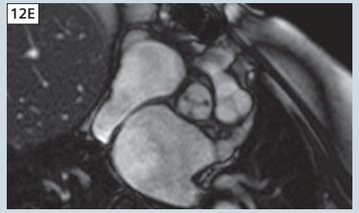

12E Aortic bioprosthesis (SSFP cine in diastole).

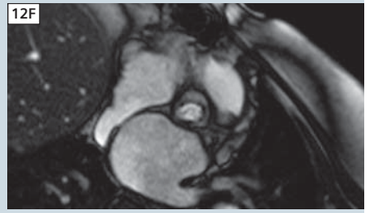

12F Aortic bioprosthesis (SSFP cine in systole).

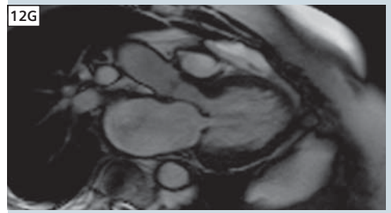

12G Moderate mitral valve stenosis (SSFP cine in diastole).

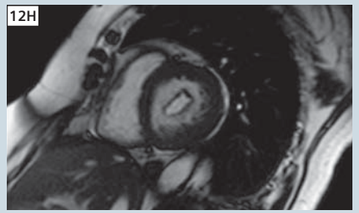

12H Moderate mitral valve stenosis (Short axis view in diastole).

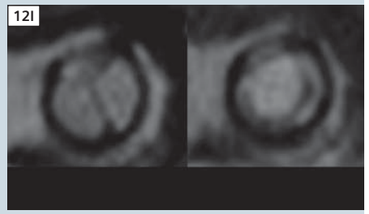

12I Mitral bioprosthesis (SSFP cine in systole and diastole).

to development of heart failure [62]. Nevertheless, at present the data regarding LGE and sudden cardiac death are still conflicting. In the near future, the results of ongoing and planned multicentre trials, like one project integrated in the EuroCMR registry [63], will clarify this important question. Regarding risk stratification in HCM in general and with respect to LGE, an actual excellent review by Barry J. Maron is worth reading [64]. Finally, already cine-CMR alone is helpful in HCM, especially in case of family-screening, because CMR identifies regions of left ventricular hypertrophy in which the extent of wall thickness is underestimated with traditional two-dimensional echocardiography [65].

News on valvular heart disease

The assessment of valvular heart disease using CMR is still mainly based on valvular visualization using cine imaging, and flow measurements using phase-contrast, as already described by Brett Cowan et al. in MAGNETOM Flash #36. Recently, Cawley et al. published a review article regarding this topic [43]. In addition, there are some important new aspects: Rudolph et al. found focal LGE in the left ventricular myocardium in 62% of patients with left ventricular hypertrophy caused by aortic stenosis [44]. Weidemann et al. reported that subjects with aortic stenosis, who exhibited severe myocardial fibrosis as detected by CMR, showed less improvement in NYHA functional class and higher mortality after aortic valve replacement compared to those with mild or no myocardial fibrosis [45]. Azevedo et al. reported similar results for patients with aortic stenosis and aortic regurgitation undergoing aortic valve replacement [46]. Thus, LGE CMR may be a novel tool for risk stratification and optimal timing of surgery in aortic valve disease. Regarding the mitral valve, Chan et al. published a valuable article on how to assess mitral regurgitation using CMR [47]. Han et al. reported that CMR can identify mitral valve prolapse by the same echocardiographic criteria. Furthermore, they found myocardial fibrosis involving the papillary muscle associated with complex ventricular arrhythmias in a subgroup of subjects [48]. The severity of posterior papillary muscle region scarring as assessed by LGE seems to impact on the surgical success after mitral repair. Flynn et al. therefore propose that preoperative scar assessing using CMR may help to find the best surgical approach in patients undergoing mitral valve operation [49]. Moreover, with increasing use of transcatheter interventions to treat mitral valve disease, the exact visualization of the complex mitral anatomy will be of enormous importance in achieving satisfactory results, as recently outlined by van Mieghem et al. CMR is regarded as part of that preparation [50]. Following aortic or mitral valve replacement with a biological heart valve device, CMR is as accurate as transthoracic and transesophageal echocardiography in assessing prosthetic function, as recently shown by our group [51, 52].
Nevertheless, it should be taken into account when applying phase-contrast sequences to assess valve disease that this technique is prone to significant background error. Gatehouse et al. demonstrated in a multi-centre, multi-vendor study that breathhold through-plane retrospectively ECG-gated phase contrast acquisitions showed significant velocity offset error, potentially causing about 5% miscalculation of cardiac output and up to 10% error in shunt measurement [53]. To omit such errors, users are encouraged to measure within the isocenter of the magnet, where the error is less, and manufacturers are currently working on improved technologies and correction algorithms.

Future trends in Cardiovascular Magnetic Resonance

Today's visions may be tomorrow's routine. CMR is a very active field of research, and many innovations in hardware, software and new clinical applications are under investigation. The following examples are just a small selection of current developments in CMR.

1.5 Tesla, SSFP, 7 mm slice thickness

7 Tesla, FGRE, 4 mm slice thickness

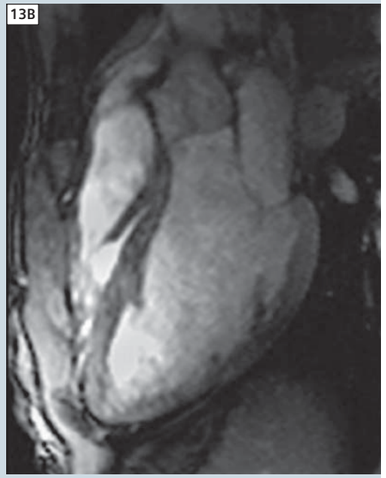

13 Three-chamber view obtained using the gold-standard, SSFP cine imaging at 1.5 Tesla, and using fast gradient echo (FGRE) cine imaging in combination with a 4-element coil and acoustic cardiac triggering at 7 Tesla, demonstrating the principal feasibility of cine imaging at 7 Tesla with high spatial resolution and satisfactory tissue-blood contrast. These images, and the research in the field of CMR at 7T as a whole, were realized within close cooperation between the working group of CMR of the Charite Medical University Berlin, and the Berlin Ultrahigh Field Facility (B.U.F.F), headed by Prof. Thoralf Niendorf, located at the Max-Delbrueck-Centre.

CMR at 7 Tesla

Increasing the field strength comes along with increases in signal- and contrast-to-noise ratio. This benefit is expected to be translated into higher spatial and temporal resolution and faster imaging techniques. However, increasing the field strength also means dramatically increasing the technological challenges, e.g. to achieve sufficient homogeneity of the magnetic field within the scanner. Therefore, human cardiac imaging at ultra-high field, (currently 7T), is still experimental and requires close cooperation between physicists and physicians to find innovative technical solutions and develop novel software and hardware components. Nevertheless, the first steps of CMR at 7T have been successful: Cine imaging and cardiac chamber quantification can be realized in a robust and accurate mode, and the first images with impressive blood-tissue contrast despite very small slice thickness offers the promise that CMR at 7T may provide new insights into pathophysiological processes [54-56].

BOLD at 3 Tesla

Blood oxygen level dependent (BOLD) imaging (principle: increased oxyhemoglobin and decreased deoxyhemoglobin tissue content result in higher T2* or T2 values, leading to corresponding signal enhancement on T2* or T2-weighted imaging) clearly benefits from higher field strength. While at 1.5T widely impractical, stress BOLD imaging seems to work at 3T with adequate quality and sufficient diagnostic accuracy to detect relevant coronary artery disease [57, 58]. Further technical developments may promote this promising method in the future, and with BOLD an additional tissue marker – complementary to the T1 and T2-weighted images described above – may arise.

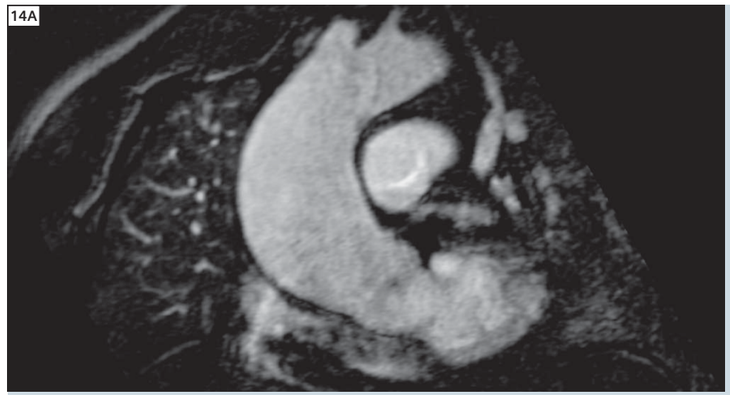

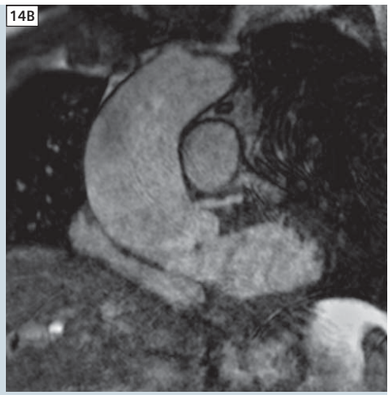

14 A 69-year-old man with aortic dilatation detected by transthoracic echocardiography was sent to CMR to assess the thoracic aorta. CMR cine imaging identified bicuspid aortic valve. Contrast-enhanced 3D angiography **(14A)** showed a loss of the typical sinutubular silhouette and a maximal diameter of 57 mm. Non-contrast enhanced SSFP and navigator-based 3D angiography with spatial resolution of 1.3 x 1.3 x 1.5 mm^3, which took 7:05 minutes to acquire, depicted the aorta with similar quality and led to the same geometric results **(14B)**. The left coronary artery is clearly visible. The patient was referred to cardiovascular surgery.

Non-contrast-enhanced 3D angiography
Non-contrast-enhanced three-dimensional (3D) angiography is desired, as contrast media is associated with the risk for nephrogenic systemic fibrosis, requires venous puncture, and is expensive. Navigator-based, ECG triggered, 3D, SSFP-based non-contrast angiography seems to achieve the diagnostic accuracy of the gold standard, contrast-enhanced 3D magnetic resonance angiography, in first clinical trials, and may enter clinical routine in the near future [59].

4D flow imaging
Time-resolved, 3D phase-contrast flow imaging has been investigated and introduced – particularly by the group of Michael Markl from Freiburg, Germany – as a novel technology to visualize both velocity and direction of the flowing blood and to quantify hemodynamic parameters like wall shear stress [60]. This application may be extremely helpful in understanding the pathomechanisms and flow turbulences of diseases of the aortic valve and the aorta, and furthermore in comprising the complex blood flow in congenital heart disease before and after surgery [61]. At present, both visualization and quantification of 4D flow imaging require complex post-processing using specific software. However, commercially available platforms with optimized workflow are currently on the way to integrate such analyses into clinical practice.
"4D Flow MR Imaging" by Alex Barker, Michael Markl et al. starts on page 46 of this issue.

Elastography
Today the quantification of diastolic dysfunction is one of the main challenges in cardiology. The accepted gold-standard is the invasive quantification of pressure-volume-curves. Nevertheless, that complex and expensive method is not common in clinical routine. Therefore, a non-invasive procedure allowing the quantification of cardiac elasticity and contractility is warranted. Recently Elgeti et al. [62] published first results in pigs applying CMR elastography and compared the results to left ventricular pressure. The promising results suggested that there is a potential for non-invasive assessment of pressure-volume function of the heart using CMR.

Conclusion

In conclusion, many important CMR studies regarding cardiac chamber quantification, ischemic, non-ischemic and valvular heart disease have been published during the past years. The compacted selection summarized in the present article represents just a small proportion of the intensive research that is performed in the wide field of CMR. Nevertheless, it underlines the increasing significance of CMR both in clinical routine, and as a research tool. In particular, studies providing prognostic data are increasingly available. In combination with trials about new CMR applications and innovative CMR techniques, these data will help to promote the acceptance of CMR as a very important imaging tool complementary to other imaging modalities, providing unique morphologic and functional cardiovascular information.

References

1 Hundley WG, Bluemke DA, Finn JP, Flamm SD, Fogel MA, Friedrich MG, Ho VB, Jerosch-Herold M, Kramer CM, Manning WJ, Patel M, Pohost GM, Stillman AE, White RD, Woodard PK. ACCF/ACR/AHA/NASCI/SCMR 2010 expert consensus document on cardiovascular magnetic resonance: a report of the American College of Cardiology Foundation Task Force on Expert Consensus Documents. Circulation 2010;121:2462-2508.

2 Kim RJ, de Roos A, Fleck E, Higgins CB, Pohost GM, Prince M, Manning WJ. Guidelines for training in Cardiovascular Magnetic Resonance (CMR). J Cardiovasc Magn Reson 2007;9:3-4.

3 Kramer CM, Barkhausen J, Flamm SD, Kim RJ, Nagel E. Standardized cardiovascular magnetic resonance imaging (CMR) protocols, society for cardiovascular magnetic resonance: board of trustees task force on standardized protocols. J Cardiovasc Magn Reson 2008;10:35.

4 Hundley WG, Bluemke D, Bogaert JG, Friedrich MG, Higgins CB, Lawson MA, McConnell MV, Raman SV, van Rossum AC, Flamm S, Kramer CM, Nagel E, Neubauer S. Society for Cardiovascular Magnetic Resonance guidelines for reporting cardiovascular magnetic resonance examinations. J Cardiovasc Magn Reson 2009;11:5.

5 Bruder O, Schneider S, Nothnagel D, Dill T, Hombach V, Schulz-Menger J, Nagel E, Lombardi M, van Rossum AC, Wagner A, Schwitter J, Senges J, Sabin GV, Sechtem U, Mahrholdt H. EuroCMR (European Cardiovascular Magnetic Resonance) registry: results of the German pilot phase. Journal of the American College of Cardiology 2009;54:1457-1466.

6 Flett AS, Westwood MA, Davies LC, Mathur A, Moon JC. The prognostic implications of cardiovascular magnetic resonance. Circ Cardiovasc Imaging 2009;2:243-250.

7 Pennell DJ. Cardiovascular magnetic resonance. Circulation 2010;121:692-705.

8 Buechel EV, Kaiser T, Jackson C, Schmitz A, Kellenberger CJ. Normal right- and left ventricular volumes and myocardial mass in children measured by steady state free precession cardiovascular magnetic resonance. J Cardiovasc Magn Reson 2009;11:19.

9 Sarikouch S, Peters B, Gutberlet M, Leismann B, Kelter-Kloepping A, Koerperich H, Kuehne T, Beerbaum P. Sex-specific pediatric percentiles for ventricular size and mass as reference values for cardiac MRI: assessment by steady-state free-precession and phase-contrast MRI flow. Circ Cardiovasc Imaging 2010;3:65-76.

10 Gerber BL, Raman SV, Nayak K, Epstein FH, Ferreira P, Axel L, Kraitchman DL. Myocardial first-pass perfusion cardiovascular magnetic resonance: history, theory, and current state of the art. J Cardiovasc Magn Reson 2008;10:18.

11 Nandalur KR, Dwamena BA, Choudhri AF, Nandalur MR, Carlos RC. Diagnostic performance of stress cardiac magnetic resonance imaging in the detection of coronary artery disease: a meta-analysis. Journal of the American College of Cardiology 2007;50:1343-1353.

12 Schwitter J, Wacker CM, van Rossum AC, Lombardi M, Al-Saadi N, Ahlstrom H, Dill T, Larsson HB, Flamm SD, Marquardt M, Johansson L. MR-IMPACT: comparison of perfusion-cardiac magnetic resonance with single-photon emission computed tomography for the detection of coronary artery disease in a multicentre, multivendor, randomized trial. European heart journal 2008;29:480-489.

13 Klein C, Nagel E, Gebker R, Kelle S, Schnackenburg B, Graf K, Dreysse S, Fleck E. Magnetic resonance adenosine perfusion imaging in patients after coronary artery bypass graft surgery. Jacc 2009;2:437-445.

14 Bernhardt P, Spiess J, Levenson B, Pilz G, Hofling B, Hombach V, Strohm O. Combined assessment of myocardial perfusion and late gadolinium enhancement in patients after percutaneous coronary intervention or bypass grafts: a multicenter study of an integrated cardiovascular magnetic resonance protocol. Jacc 2009;2:1292-1300.

15 Jahnke C, Nagel E, Gebker R, Kokocinski T, Kelle S, Manka R, Fleck E, Paetsch I. Prognostic value of cardiac magnetic resonance stress tests: adenosine stress perfusion and dobutamine stress wall motion imaging. Circulation 2007;115:1769-1776.

16 Steel K, Broderick R, Gandla V, Larose E, Resnic F, Jerosch-Herold M, Brown KA, Kwong RY. Complementary prognostic values of stress myocardial perfusion and late gadolinium enhancement imaging by cardiac magnetic resonance in patients with known or suspected coronary artery disease. Circulation 2009;120:1390-1400.

17 Geleijnse ML, Krenning BJ, Nemes A, van Dalen BM, Soliman OI, Ten Cate FJ, Schinkel AF, Boersma E, Simoons ML. Incidence, pathophysiology, and treatment of complications during dobutamine-atropine stress echocardiography. Circulation 2010;121:1756-1767.

18 Klem I, Heitner JF, Shah DJ, Sketch MH, Jr., Behar V, Weinsaft J, Cawley P, Parker M, Elliott M, Judd RM, Kim RJ. Improved detection of coronary artery disease by stress perfusion cardiovascular magnetic resonance with the use of delayed enhancement infarction imaging. Journal of the American College of Cardiology 2006;47:1630-1638.

19 Plein S, Schwitter J, Suerder D, Greenwood JP, Boesiger P, Kozerke S. k-Space and time sensitivity encoding-accelerated myocardial perfusion MR imaging at 3.0 T: comparison with 1.5 T. Radiology 2008;249:493-500.

20 Cheng AS, Pegg TJ, Karamitsos TD, Searle N, Jerosch-Herold M, Choudhury RP, Banning AP, Neubauer S, Robson MD, Selvanayagam JB. Cardiovascular magnetic resonance perfusion imaging at 3-tesla for the detection of coronary artery disease: a comparison with 1.5-tesla. Journal of the American College of Cardiology 2007;49:2440-2449.

21 Lockie T, Nagel E, Redwood S, Plein S. Use of cardiovascular magnetic resonance imaging in acute coronary syndromes. Circulation 2009;119:1671-1681.

22 Kim HW, Farzaneh-Far A, Kim RJ. Cardiovascular magnetic resonance in patients with myocardial infarction: current and emerging applications. Journal of the American College of Cardiology 2009;55:1-16.

23 Kim RJ, Albert TS, Wible JH, Elliott MD, Allen JC, Lee JC, Parker M, Napoli A, Judd RM. Performance of delayed-enhancement magnetic resonance imaging with gadoversetamide contrast for the detection and assessment of myocardial infarction: an international, multicenter, double-blinded, randomized trial. Circulation 2008;117:629-637.

24 Abdel-Aty H, Cocker M, Meek C, Tyberg JV, Friedrich MG. Edema as a very early marker for acute myocardial ischemia: a cardiovascular magnetic resonance study. Journal of the American College of Cardiology 2009;53:1194-1201.

25 Friedrich MG, Abdel-Aty H, Taylor A, Schulz-Menger J, Messroghli D, Dietz R. The salvaged area at risk in reperfused acute myocardial infarction as visualized by cardiovascular magnetic resonance. Journal of the American College of Cardiology 2008;51:1581-1587.

26 Francone M, Bucciarelli-Ducci C, Carbone I, Canali E, Scardala R, Calabrese FA, Sardella G, Mancone M, Catalano C, Fedele F, Passariello R, Bogaert J, Agati L. Impact of primary coronary angioplasty delay on myocardial salvage, infarct size, and microvascular damage in patients with ST-segment elevation myocardial infarction: insight from cardiovascular magnetic resonance. Journal of the American College of Cardiology 2009;54:2145-2153.

27 Eitel I, Desch S, Fuernau G, Hildebrand L, Gutberlet M, Schuler G, Thiele H. Prognostic significance and determinants of myocardial salvage assessed by cardiovascular magnetic resonance in acute reperfused myocardial infarction. Journal of the American College of Cardiology 2010;55:2470-2479.

28 Raman SV, Simonetti OP, Winner MW, 3rd, Dickerson JA, He X, Mazzaferri EL, Jr., Ambrosio G. Cardiac magnetic resonance with edema imaging identifies myocardium at risk and predicts worse outcome in patients with non-ST-segment elevation acute coronary syndrome. Journal of the American College of Cardiology 2010;55:2480-2488.

29 Ganame J, Messalli G, Dymarkowski S, Rademakers FE, Desmet W, Van de Werf F, Bogaert J. Impact of myocardial haemorrhage on left ventricular function and remodelling in patients with reperfused acute myocardial infarction. European heart journal 2009;30:1440-1449.

30 Nijveldt R, Beek AM, Hirsch A, Stoel MG, Hofman MB, Umans VA, Algra PR, Twisk JW, van Rossum AC. Functional recovery after acute myocardial infarction: comparison between angiography, electrocardiography, and cardiovascular magnetic resonance measures of microvascular injury. Journal of the American College of Cardiology 2008;52:181-189.

31 Cury RC, Shash K, Nagurney JT, Rosito G, Shapiro MD, Nomura CH, Abbara S, Bamberg F, Ferencik M, Schmidt EJ, Brown DF, Hoffmann U, Brady TJ. Cardiac magnetic resonance with T2-weighted imaging improves detection of patients with acute coronary syndrome in the emergency department. Circulation 2008;118:837-844.

32 Eitel I, Behrendt F, Schindler K, Kivelitz D, Gutberlet M, Schuler G, Thiele H. Differential diagnosis of suspected apical ballooning syndrome using contrast-enhanced magnetic resonance imaging. European heart journal 2008;29:2651-2659.

33 Assomull RG, Lyne JC, Keenan N, Gulati A, Bunce NH, Davies SW, Pennell DJ, Prasad SK. The role of cardiovascular magnetic resonance in patients presenting with chest pain, raised troponin, and unobstructed coronary arteries. European heart journal 2007;28:1242-1249.

34 Morton G, Schuster A, Perera D, Nagel E. Cardiac magnetic resonance imaging to guide complex revascularization in stable coronary artery disease. European heart journal 2010.

35 Thiele H, Kappl MJ, Conradi S, Niebauer J, Hambrecht R, Schuler G. Reproducibility of chronic and acute infarct size measurement by delayed enhancement-magnetic resonance imaging. Journal of the American College of Cardiology 2006;47:1641-1645.

36 Kwong RY, Chan AK, Brown KA, Chan CW, Reynolds HG, Tsang S, Davis RB. Impact of unrecognized myocardial scar detected by cardiac magnetic resonance imaging on event-free survival in patients presenting with signs or symptoms of coronary artery disease. Circulation 2006;113:2733-2743.

37 Kwong RY, Sattar H, Wu H, Vorobiof G, Gandla V, Steel K, Siu S, Brown KA. Incidence and prognostic implication of unrecognized myocardial scar characterized by cardiac magnetic resonance in diabetic patients without clinical evidence of myocardial infarction. Circulation 2008;118:1011-1020.

38 Kwon DH, Halley CM, Carrigan TP, Zysek V, Popovic ZB, Setser R, Schoenhagen P, Starling RC, Flamm SD, Desai MY. Extent of left ventricular scar predicts outcomes in ischemic cardiomyopathy patients with significantly reduced systolic function: a delayed hyperenhancement cardiac magnetic resonance study. Jacc 2009;2:34-44.

39 Roes SD, Borleffs CJ, van der Geest RJ, Westenberg JJ, Marsan NA, Kaandorp TA, Reiber JH, Zeppenfeld K, Lamb HJ, de Roos A, Schalij MJ, Bax JJ. Infarct tissue heterogeneity assessed with contrast-enhanced MRI predicts spontaneous ventricular arrhythmia in patients with ischemic cardiomyopathy and implantable cardioverter-defibrillator. Circ Cardiovasc Imaging 2009;2:183-190.

40 Schmidt A, Azevedo CF, Cheng A, Gupta SN, Bluemke DA, Foo TK, Gerstenblith G, Weiss RG, Marban E, Tomaselli GF, Lima JA, Wu KC. Infarct tissue heterogeneity by magnetic resonance imaging identifies enhanced cardiac arrhythmia susceptibility in patients with left ventricular dysfunction. Circulation 2007;115:2006-2014.

41 Bogun F, Desjardins B, Crawford T, Good E, Jongnarangsin K, Oral H, Chugh A, Pelosi F, Morady F. Post-infarction ventricular arrhythmias originating in papillary muscles. Journal of the American College of Cardiology 2008;51:1794-1802.

42 Okayama S, Uemura S, Soeda T, Onoue K, Somekawa S, Ishigami KI, Watanabe M, Nakajima T, Fujimoto S, Saito Y. Clinical significance of papillary muscle late enhancement detected via cardiac magnetic resonance imaging in patients with single old myocardial infarction. International journal of cardiology 2010.

43 Karamitsos TD, Francis JM, Myerson S, Selvanayagam JB, Neubauer S. The role of cardiovascular magnetic resonance imaging in heart failure. Journal of the American College of Cardiology 2009;54:1407-1424.

44 Flett AS, Hayward MP, Ashworth MT, Hansen MS, Taylor AM, Elliott PM, McGregor C, Moon JC. Equilibrium contrast cardiovascular magnetic resonance for the measurement of diffuse myocardial fibrosis: preliminary validation in humans. Circulation 2010;122:138-144.

45 Friedrich MG. Myocardial edema – a new clinical entity? Nat Rev Cardiol 2010;7:292-296.

46 Zagrosek A, Abdel-Aty H, Boyé P, Wassmuth R, Messroghli D, Utz W, Rudolph A, Bohl S, Dietz R, Schulz-Menger J. Cardiac magnetic resonance monitors reversible and irreversible myocardial injury in myocarditis. J Am Coll Cardiol Img 2009;2:131-138.

47 Friedrich MG, Sechtem U, Schulz-Menger J, Holmvang G, Alakija P, Cooper LT, White JA, Abdel-Aty H, Gutberlet M, Prasad S, Aletras A, Laissy JP, Paterson I, Filipchuk NG, Kumar A, Pauschinger M, Liu P. Cardiovascular magnetic resonance in myocarditis: A JACC White Paper. Journal of the American College of Cardiology 2009;53:1475-1487.

48 Wassmuth R, Gobel U, Natusch A, Schneider W, Kettritz R, Dietz R, Luft FC, Schulz-Menger J. Cardiovascular magnetic resonance imaging detects cardiac involvement in Churg-Strauss syndrome. J Card Fail 2008;14:856-860.

49 Abdel-Aty H, Siegle N, Natusch A, Gromnica-Ihle E, Wassmuth R, Dietz R, Schulz-Menger J. Myocardial tissue characterization in systemic lupus erythematosus: value of a comprehensive cardiovascular magnetic resonance approach. Lupus 2008;17:561-567.

50 Taylor AJ, Vaddadi G, Pfluger H, Butler M, Bergin P, Leet A, Richardson M, Cherayath J, Iles L, Kaye DM. Diagnostic performance of multisequential cardiac magnetic resonance imaging in acute cardiac allograft rejection. Eur J Heart Fail 2010; 12:45-51.

51 Baccouche H, Mahrholdt H, Meinhardt G, Merher R, Voehringer M, Hill S, Klingel K, Kandolf R, Sechtem U, Yilmaz A. Diagnostic synergy of non-invasive cardiovascular magnetic resonance and invasive endomyocardial biopsy in troponin-positive patients without coronary artery disease. European heart journal 2009;30:2869-2879.

52 Masci PG, Marinelli M, Piacenti M, Lorenzoni V, Positano V, Lombardi M, L'Abbate A, Neglia D. Myocardial structural, perfusion, and metabolic correlates of left bundle branch block mechanical derangement in patients with dilated cardiomyopathy: a tagged cardiac magnetic resonance and positron emission tomography study. Circ Cardiovasc Imaging 2010;3:482-490.

53 Hombach V, Merkle N, Torzewski J, Kraus JM, Kunze M, Zimmermann O, Kestler HA, Wohrle J. Electrocardiographic and cardiac magnetic resonance imaging parameters as predictors of a worse outcome in patients with idiopathic dilated cardiomyopathy. European heart journal 2009;30:2011-2018.

54 Marcus FI, McKenna WJ, Sherrill D, Basso C, Bauce B, Bluemke DA, Calkins H, Corrado D, Cox MG, Daubert JP, Fontaine G, Gear K, Hauer R, Nava A, Picard MH, Protonotarios N, Saffitz JE, Sanborn DM, Steinberg JS, Tandri H, Thiene G, Towbin JA, Tsatsopoulou A, Wichter T, Zareba W. Diagnosis of arrhythmogenic right ventricular cardiomyopathy/dysplasia: proposed modification of the task force criteria. Circulation 2010;121:1533-1541.

55 Wijnmaalen AP, Schalij MJ, Bootsma M, Kies P, A DER, Putter H, Bax JJ, Zeppenfeld K. Patients with scar-related right ventricular tachycardia: determinants of long-term outcome. J Cardiovasc Electrophysiol 2009;20:1119-1127.

56 Kellman P, Hernando D, Arai AE. Myocardial Fat Imaging. Curr Cardiovasc Imaging Rep 2010;3:83-91.

57 Dalal D, Tandri H, Judge DP, Amat N, Macedo R, Jain R, Tichnell C, Daly A, James C, Russell SD, Abraham T, Bluemke DA, Calkins H. Morphologic variants of familial arrhythmogenic right ventricular dysplasia/cardiomyopathy a genetics-magnetic resonance imaging correlation study. Journal of the American College of Cardiology 2009;53:1289-1299.

58 Rudolph A, Abdel-Aty H, Bohl S, Boye P, Zagrosek A, Dietz R, Schulz-Menger J. Noninvasive detection of fibrosis applying contrast-enhanced cardiac magnetic resonance in different forms of left ventricular hypertrophy relation to remodeling. Journal of the American College of Cardiology 2009;53:284-291.

59 Maceira AM, Prasad SK, Hawkins PN, Roughton M, Pennell DJ. Cardiovascular magnetic resonance and prognosis in cardiac amyloidosis. J Cardiovasc Magn Reson 2008;10:54.

60 Rubinshtein R, Glockner JF, Ommen SR, Araoz PA, Ackerman MJ, Sorajja P, Bos JM, Tajik AJ, Valeti US, Nishimura RA, Gersh BJ. Characteristics and clinical significance of late gadolinium enhancement by contrast-enhanced magnetic resonance imaging in patients with hypertrophic cardiomyopathy. Circ Heart Fail 2010;3:51-58.

61 Bruder O, Wagner A, Jensen CJ, Schneider S, Ong P, Kispert EM, Nassenstein K, Schlosser T, Sabin GV, Sechtem U, Mahrholdt H. Myocardial scar visualized by cardiovascular magnetic resonance imaging predicts major adverse events in patients with hypertrophic cardiomyopathy. Journal of the American College of Cardiology 2010;56:875-887.

62 O'Hanlon R, Grasso A, Roughton M, Moon JC, Clark S, Wage R, Webb J, Kulkarni M, Dawson D, Sulaibeekh L, Chandrasekaran B, Bucciarelli-Ducci C, Pasquale F, Cowie MR, McKenna WJ, Sheppard MN, Elliott PM, Pennell DJ, Prasad SK. Prognostic significance of myocardial fibrosis in hypertrophic cardiomyopathy. Journal of the American College of Cardiology 2010;56:867-874.

63 Wagner A, Bruder O, Schneider S, Nothnagel D, Buser P, Pons-Lado G, Dill T, Hombach V, Lombardi M, van Rossum AC, Schwitter J, Senges J, Sabin GV, Sechtem U, Mahrholdt H, Nagel E. Current variables, definitions and endpoints of the European cardiovascular magnetic resonance registry. J Cardiovasc Magn Reson 2009; 11:43.

64 Maron BJ. Contemporary insights and strategies for risk stratification and prevention of sudden death in hypertrophic cardiomyopathy. Circulation 2010;121:445-456.

65 Maron MS, Lesser JR, Maron BJ. Management implications of massive left ventricular hypertrophy in hypertrophic cardiomyopathy significantly underestimated by echocardiography but identified by cardiovascular magnetic resonance. The American journal of cardiology 2010;105:1842-1843.

66 Cawley PJ, Maki JH, Otto CM. Cardiovascular magnetic resonance imaging for valvular heart disease: technique and validation. Circulation 2009;119:468-478.

67 Weidemann F, Herrmann S, Stork S, Niemann M, Frantz S, Lange V, Beer M, Gattenlohner S, Voelker W, Ertl G, Strotmann JM. Impact of myocardial fibrosis in patients with symptomatic severe aortic stenosis. Circulation 2009;120:577-584.

68 Azevedo CF, Nigri M, Higuchi ML, Pomerantzeff PM, Spina GS, Sampaio RO, Tarasoutchi F, Grinberg M, Rochitte CE. Prognostic significance of myocardial fibrosis quantification by histopathology and magnetic resonance imaging in patients with severe aortic valve disease. Journal of the American College of Cardiology 2010;56:278-287.

69 Chan KM, Wage R, Symmonds K, Rahman-Haley S, Mohiaddin RH, Firmin DN, Pepper JR, Pennell DJ, Kilner PJ. Towards comprehensive assessment of mitral regurgitation using cardiovascular magnetic resonance. J Cardiovasc Magn Reson 2008;10:61.

70 Han Y, Peters DC, Salton CJ, Bzymek D, Nezafat R, Goddu B, Kissinger KV, Zimetbaum PJ, Manning WJ, Yeon SB. Cardiovascular magnetic resonance characterization of mitral valve prolapse. Jacc 2008;1:294-303.

71 Flynn M, Curtin R, Nowicki ER, Rajeswaran J, Flamm SD, Blackstone EH, Mihaljevic T. Regional wall motion abnormalities and scarring in severe functional ischemic mitral regurgitation: A pilot cardiovascular magnetic resonance imaging study. The Journal of thoracic and cardiovascular surgery 2009;137:1063-1070 e1062.

72 Van Mieghem NM, Piazza N, Anderson RH, Tzikas A, Nieman K, De Laat LE, McGhie JS, Geleijnse ML, Feldman T, Serruys PW, de Jaegere PP. Anatomy of the Mitral Valvular Complex and Its Implications for Transcatheter Interventions for Mitral Regurgitation. Journal of the American College of Cardiology 2010;56:617-626.

73 von Knobelsdorff-Brenkenhoff F, Rudolph A, Wassmuth R, Bohl S, Buschmann EE, Abdel-Aty H, Dietz R, Schulz-Menger J. Feasibility of cardiovascular magnetic resonance to assess the orifice area of aortic bioprostheses. Circ Cardiovasc Imaging 2009;2:397-404, 392 p following 404.

74 von Knobelsdorff-Brenkenhoff F, Rudolph A, Wassmuth R, Schulz-Menger J. Assessment of mitral bioprostheses using cardiovascular magnetic resonance. J Cardiovasc Magn Reson 2010;12:36.

75 Gatehouse PD, Rolf MP, Graves MJ, Hofman MB, Totman J, Werner B, Quest RA, Liu Y, von Spiczak J, Dieringer M, Firmin DN, van Rossum A, Lombardi M, Schwitter J, Schulz-Menger J, Kilner PJ. Flow measurement by cardiovascular magnetic resonance: a multi-centre multi-vendor study of background phase offset errors that can compromise the accuracy of derived regurgitant or shunt flow measurements. J Cardiovasc Magn Reson 2010;12:5.

76 Niendorf T, Sodickson DK, Krombach GA, Schulz-Menger J. Toward cardiovascular MRI at 7 T: clinical needs, technical solutions and research promises. European radiology 2010.

77 Snyder CJ, DelaBarre L, Metzger GJ, van de Moortele PF, Akgun C, Ugurbil K, Vaughan JT. Initial results of cardiac imaging at 7 Tesla. Magn Reson Med 2009;61:517-524.

78 von Knobelsdorff-Brenkenhoff F, Frauenrath T, Prothmann M, Dieringer MA, Hezel F, Renz W, Kretschel K, Niendorf T, Schulz-Menger J. Cardiac chamber quantification using magnetic resonance imaging at 7 Tesla-a pilot study. European radiology 2010.

79 Jahnke C, Gebker R, Manka R, Schnackenburg B, Fleck E, Paetsch I. Navigator-gated 3D blood oxygen level-dependent CMR at 3.0-T for detection of stress-induced myocardial ischemic reactions. Jacc 2010;3:375-384.

80 Karamitsos TD, Leccisotti L, Arnold JR, Recio-Mayoral A, Bhamra-Ariza P, Howells RK, Searle N, Robson MD, Rimoldi OE, Camici PG, Neubauer S, Selvanayagam JB. Relationship between regional myocardial oxygenation and perfusion in patients with coronary artery disease: insights from cardiovascular magnetic resonance and positron emission tomography. Circ Cardiovasc Imaging 2010;3:32-40.

81 Vohringer M, Flewitt JA, Green JD, Dharmakumar R, Wang J, Jr., Tyberg JV, Friedrich MG. Oxygenation-sensitive CMR for assessing vasodilator-induced changes of myocardial oxygenation. J Cardiovasc Magn Reson 2010;12:20.

82 Krishnam MS, Tomasian A, Malik S, Desphande V, Laub G, Ruehm SG. Image quality and diagnostic accuracy of unenhanced SSFP MR angiography compared with conventional contrast-enhanced MR angiography for the assessment of thoracic aortic diseases. European radiology 2010;20:1311-1320.

83 Frydrychowicz A, Berger A, Russe MF, Stalder AF, Harloff A, Dittrich S, Hennig J, Langer M, Markl M. Time-resolved magnetic resonance angiography and flow-sensitive 4-dimensional magnetic resonance imaging at 3 Tesla for blood flow and wall shear stress analysis. The Journal of thoracic and cardiovascular surgery 2008;136:400-407.

84 Markl M, Geiger J, Kilner PJ, Foll D, Stiller B, Beyersdorf F, Arnold R, Frydrychowicz A. Time-resolved three-dimensional magnetic resonance velocity mapping of cardiovascular flow paths in volunteers and patients with Fontan circulation. Eur J Cardiothorac Surg 2010.

85 Elgeti T, Laule M, Kaufels N, Schnorr J, Hamm B, Samani A, Braun J, Sack I. Cardiac MR elastography: comparison with left ventricular pressure measurement. J Cardiovasc Magn Reson 2009; 11:44.

Contact
Jeanette Schulz-Menger, M.D.
Experimental and Clinical Research Center
Medical University Berlin
Charité Campus Buch
and
HELIOS Krankenhaus Berlin-Buch
Dept. of Cardiology and Nephrology
Schwanebecker Chaussee. 50
D-13125 Berlin
Germany
jeanette.schulz-menger@charite.de

SCMR recommended CMR protocols and CMR Users Guide – on CD!

To aid standardization of CMR, the Society for Cardiovascular Magnetic Resonance (SCMR) released CMR exam protocol recommendations for the most frequent CMR procedures, from MR imaging of myocardial infarct and cardiomyopathies, stress MRI, coronary MRA to valvular disease, congenital heart disease and more. In a collaborational effort of Siemens Healthcare and the SCMR we were able to prepare clinically optimized exam protocols for 1.5T and 3T MAGNETOM systems with Tim in accordance to the SCMR recommendations.

The protocols for software version *syngo* MR B17 are available as downloadable EDX files on the attached CD.

The protocols for software versions *syngo* MR B15 and *syngo* MR B13 are available for download at www.siemens.com/scrm-recommended-protocols

Please use the appropriate protocols optimized for your particular scanner type, number of receiver channels and gradient performance. For ease of use, the protocols are organized by exam modules or common cardiac diseases and sub-organized by the patient's cooperative abilities.

For example:
Acute Myocardial Infarct
- Recommended – Breathhold & Triggered Protocol
- Free Breathing & Triggered Protocol
- Extreme Arrhythmia – Free Breathing & Non-Triggered Protocol

The CD also contains a comprehensive CMR Users Guide (90+ pages) for the most frequent CMR indications including illustrations on how to plan the correct orientations. To enable the use in everyday routine, the chapters are closely linked to the EDX protocols provided on the CD.

Acknowledgement: We would like to thank Prof. Stefan Neubauer (University of Oxford, UK; President of SCMR), Prof. Christopher Kramer (University of Virginia, USA; Chair of the CMR Acquisition Protocol Committee at SCMR) and Gary McNeal (Advanced CMR Application Specialist; Siemens Medical Solutions USA) for their tremendous efforts and support.

This is an example of the comprehensive CMR Users Guide for the most frequent CMR indications that you will find on the CD or at **www.siemens.com/scmr-recommended-protocols**

Arrhythmogenic Right Ventricular Cardiomyopathy

1 **Localizer Module** for localization.
2 **LV Function Module** to assess ventricular function.

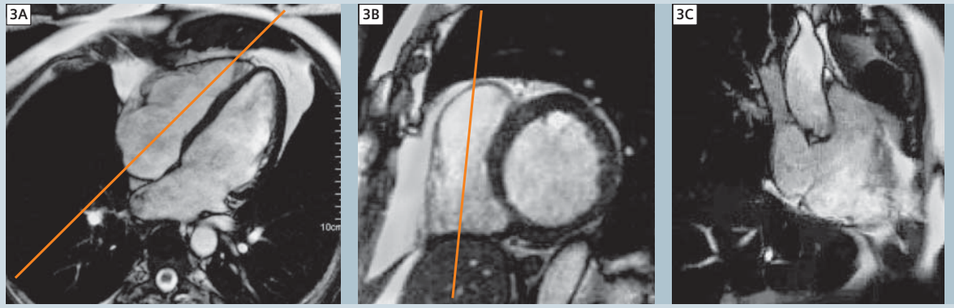

3 **Right Ventricular Vertical Long Axis Cine:** prescribe 1 right ventricular long axis slice from four chamber and basal short axis views, parallel to ventricular septum bisecting tricuspid valve, right atrium, and right ventricle, single breathhold, retrospective gating.

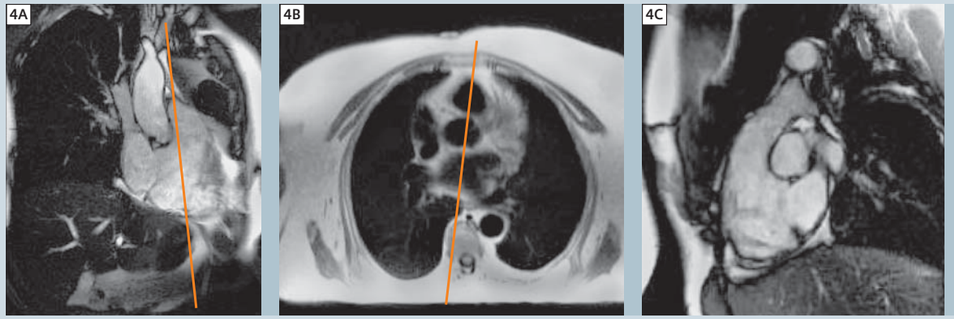

4 **Right Ventricular Outflow Tract Cine:** prescribe 1 slice from right ventricular vertical long axis and axial views, bisect pulmonary outflow tract, pulmonic valve, and main pulmonary artery, single breathhold, retrospective gating.

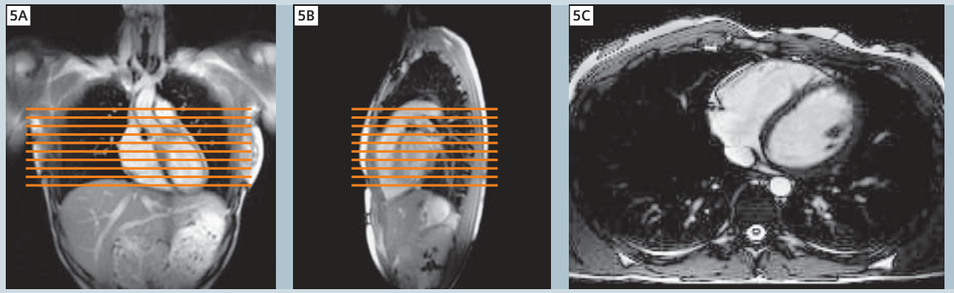

5 **Axial Cine:** prescribe 12 slices, adjust gap to cover entire right ventricle from base to apex, multiple breathholds, retrospective gating.

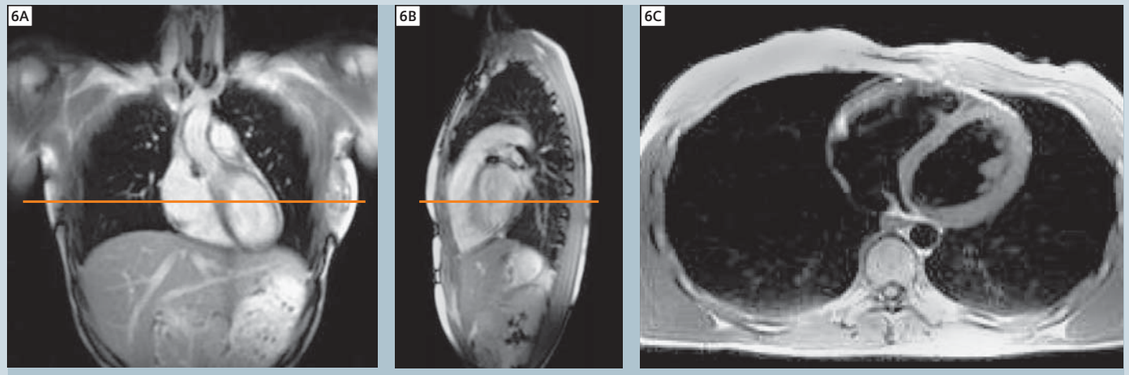

6 Optional Axial TSE Dark Blood T1: for selected slice levels of right ventricle, segmented dark blood tse, single breathhold, trigger on every heartbeat, capture cycle for diastolic gating.

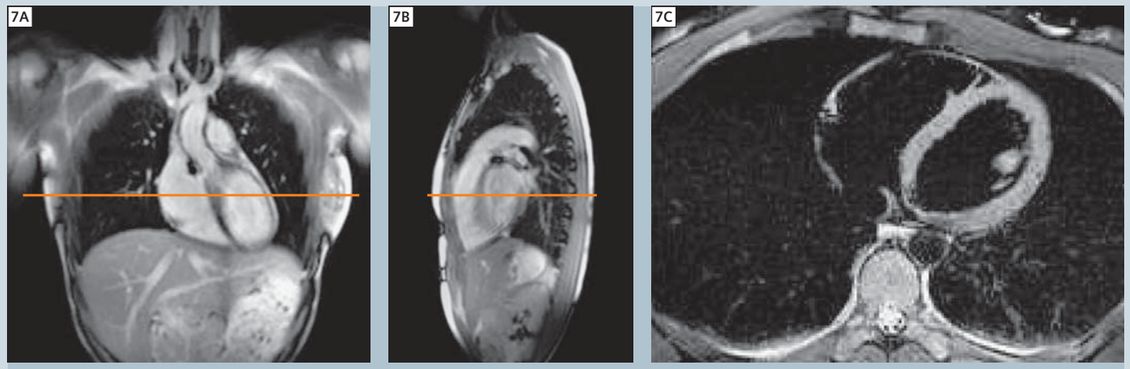

7 Optional Axial TSE Dark Blood T1 Fatsat: for selected slice levels of right ventricle, segmented dark blood tse with fatsat, single breathhold, trigger on every heartbeat, capture cycle for diastolic gating.

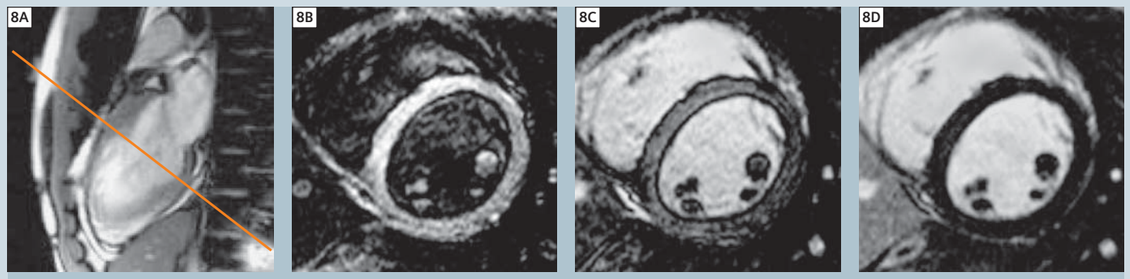

8 Optional TI Scout: determine optimal TI for nulling of normal RV myocardium, prescribe as a mid ventricular short axis slice, rotate FoV to avoid wrap, single breathhold, trigger on every second heartbeat, capture cycle for optimal acquisition window.

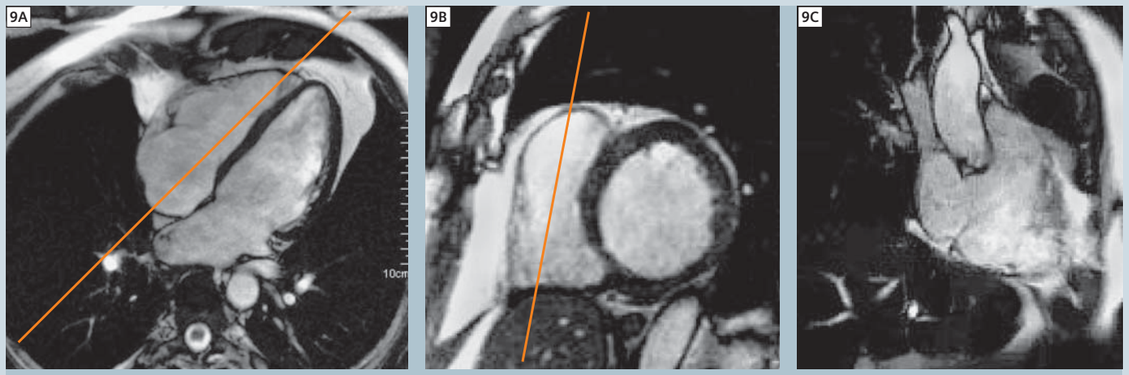

9 Optional Right Ventricular Vertical Long Axis Delayed: 1 slice in 1 breathhold, phase sensitive inversion recovery turboflash technique, provides both magnitude and real images, adjust TI for nulling of normal RV myocardium, trigger on every second heartbeat, capture cycle for diastolic gating.

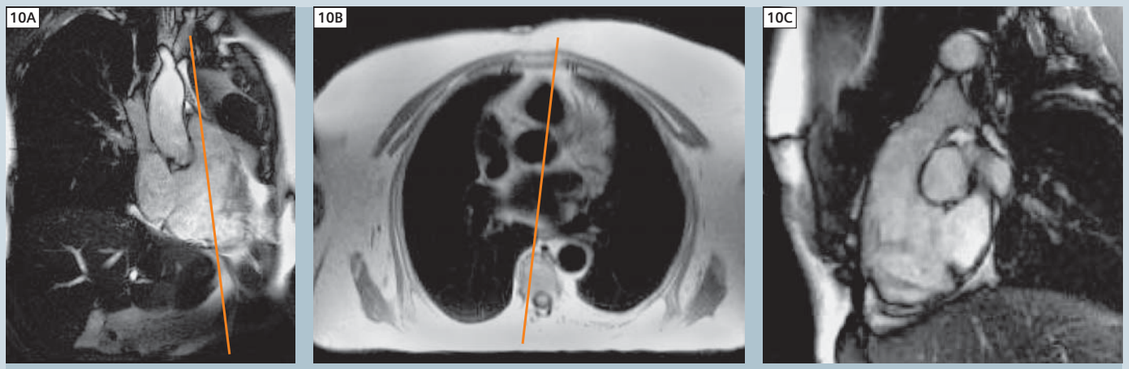

10 Optional Right Ventricular Outflow Tract Delayed: 1 slice in 1 breathhold, phase sensitive inversion recovery turboflash technique, provides both magnitude and real images, adjust TI for nulling of normal RV myocardium, trigger on every second heartbeat, capture cycle for diastolic gating.

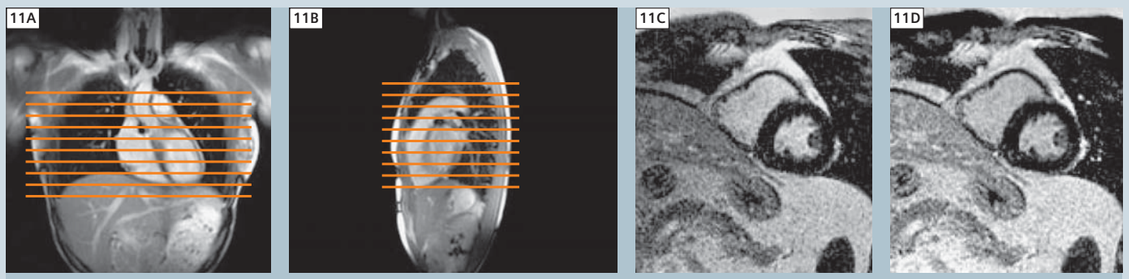

11 Optional Axial Delayed: 12 slices in 12 breathholds, phase sensitive inversion recovery turboflash technique, provides both magnitude and real images, adjust TI for nulling of normal RV myocardium, trigger on every second heartbeat, capture cycle for diastolic gating.

Low-Dose Contrast-Enhanced MR Angiography

Roya Saleh, M.D.[1]; Paul Finn, M.D.[1]; Yutaka Natsuaki, Ph.D.[2]; Gerhard Laub, Ph.D.[2]

[1]*Department of Radiology, University of California at Los Angeles, CA, USA*
[2]*Siemens Healthcare, West Coast Team, MR R&D, Los Angeles, CA, USA*

Introduction

Contrast-enhanced MR angiography (ceMRA) has been firmly established as a very powerful diagnostic tool and is employed worldwide both for routine clinical work and for specialized applications. Gadolinium-DTPA is frequently used in ceMRA for imaging the carotid, thoracic, abdominal, and peripheral circulations. With proper timing and technique, high quality MRA can be performed with sub-millimeter spatial resolution in as little as a breathhold period.

In recent years, the recognition of nephrogenic systemic fibrosis (NSF) has sparked widespread concern within the clinical community and has focused attention on the safe utilization and dosage of contrast agents. Symptoms of NSF first appeared in 1997 [1], but it was not until 2006 that an association with gadolinium (Gd)-based contrast agents was made [2]. While it is still speculative how Gd-based agents can trigger NSF, impairment of renal function is known to be a universal precondition and most cases have been associated with end stage renal failure. With normal kidney function, 90% of the injected dose of extracellular contrast agent is removed via the kidneys within the first 24 hours and in patients with severe renal impairment (not on dialysis) this time can be prolonged up to 7 days to clear 80% of contrast media, depending on the degree of renal function [3]. The process of renal clearance is exponential, such that the higher the injected dose, the faster the rate of renal excretion, but the longer it takes for the blood concentration to fall below a given threshold. In renal impairment, the elimination rate constant for extracellular contrast agents falls proportionately to the degree of renal impairment. So, patients with kidney impairment will have more difficulty clearing the Gd than patients with normal kidneys. It is reasonable to suggest that decreasing the dose of Gd will decrease risk exposure in susceptible patients, and the majority of proven cases of NSF have been associated with high dose Gd administration (often repeated) [4-6]. Abujudeh et al., in a recent study of 36 patients with NSF has shown and concluded that NSF develops in patients with renal impairment after exposure to Gd in a dose- and time-dependent manner [7]. Use of the minimum effective dose of Gd in renal impairment has been recommended by scientific societies and governmental agencies both in the U.S. and in Europe.

At one extreme, MRA can be acquired without any contrast injection (i.e. non-contrast MRA), and numerous successful non-contrast MRA techniques have been reported (e.g. *syngo* NATIVE TrueFISP [8, 9], *syngo* NATIVE SPACE, Time-Of-Flight [10] and 3D SSFP [11-13]). However, all of the non-contrast techniques are to some extent flow-sensitive, and this limitation makes them less robust and often less practical when compared to ceMRA. Also, the majority of non-contrast MRA techniques require longer scan times since multiple arterial and venous phases are necessary to complete the data acquisition.

An alternative approach to non-contrast MRA is to use low Gd doses. By optimizing the ceMRA sequences to match the contrast timing and k-space acquisition, significant reduction in the contrast dose is possible. Moreover, at 3T, dramatic dose reduction can be realized relative to conventional doses at 1.5T. Time resolved 3D MRA with *syngo* TWIST can be performed with less than 2 ml of Gd contrast and high spatial resolution 3D Carotid imaging can be performed reliably with 8 ml or less. In our practice, when we reduce the dose for ceMRA, we do so by dilution of the native gadolinium formulation at the time of administration – sometimes by a factor of four (Table 1, 2). The reason for this is so that the timing and infusion duration of the (diluted) contrast solution is identical to what it would be for an equal volume of the native (undiluted) gadolinium formulation. The result is that the peak intravascular concentration of Gd is lower with the diluted solution, but occurs at the same time as with the original protocol. Therefore, the shape and duration of the curves are identical.

Table 1: Dilution of native Gd contrast solution for MR angiography

	1.5 Tesla			3 Tesla		
	Undiluted contrast volume	Added Saline	Final solution conc.	Undiluted contrast volume	Added Saline	Final solution conc.
Single station MRA (Head & Neck, Chest and Renals)	20 cc	20 cc	50%	10 cc	30 cc	25%
Multi station (Lower Extremity MRA)	30 cc	30 cc	50%	20 cc	40 cc	33%

Table 2: Contrast injection scheme for MR angiography at 1.5 Tesla and 3.0 Tesla

	Methods of MRA	Injection #	Solution vol. (diluted Gd)	Saline flush	Injection rate
Head and Neck MRA	Isotropic Dynamic MRA (Sag & Cor) Static MRA	1 2	6 cc 34 cc	20 cc 20 cc	3 cc/s 2 cc/s
Chest MRA	3D Timing bolus Dynamic MRA Static MRA	1 2 3	2 cc 6 cc 32 cc	20 cc 20 cc 20 cc	2 cc/s 3 cc/s 2 cc/s
Renal MRA*	3D Timing bolus Dynamic MRA Static MRA	1 2 3	2 cc 6 cc 32 cc	20 cc 20 cc 20 cc	2 cc/s 3 cc/s 2 cc/s
Multi Station (Lower Extremity MRA)	3D Timing bolus MRA (Calves) 3D Timing bolus MRA (Abdomen) Static MRA (Calves) Static MRA (Abdomen and thighs)	1 2 3 4	3 cc 3 cc 24 cc 30 cc	20 cc 20 cc 20 cc 20 cc	1.2 cc/s 1.2 cc/s 1.2 cc/s 1.2 cc/s

*For renal MRA at 3.0 T, solution is made of 15 cc contrast and 25 cc saline (37.5% relative Gd conc.) with iPAT x 4.

Background and technique

Image quality and vessel contrast are affected by the contrast dose as well as the timing of the agent passing through the region of interest. A higher dose of contrast agent causes more shortening of the blood T1 and may produce stronger vessel delineation (although the effect is not linear over all dose ranges). A high dose (double or triple dose) of contrast has been used frequently in the past, assuming that MR contrast agents are safe under all conditions. For a 70 kg patient, a double dose of 0.2 mmol/kg of Gd-DTPA corresponds to 30 ml of the contrast formulation while a triple dose of 0.3 mmol/kg corresponds to approximately 45 ml. However, it is possible to produce high quality MR angiograms with a fraction of commonly employed doses [14-16]. Several imaging strategies can be implemented to perform low-dose contrast-enhanced MRA. The common goal of these strategies is to optimally match injection and k space coverage to achieve the best image quality at a reduced dose. Low dose contrast-enhanced MRA can be performed at both 1.5T and 3T. The tradeoff in vascular signal when reducing the contrast dose is less noticeable at 3T. Due to the higher intrinsic blood-to-tissue signal available at 3T compared to at 1.5T, low dose ceMRA is particularly successful at 3T.

The peak concentration of Gd in the blood following intravenous injection is determined by the rate of injection. The duration over which the peak persists (the 'plateau') is determined by the duration of the injection. A high, sustained peak blood concentration implies that the injection rate is fast and that the injection duration is prolonged; both conditions can be met only if the injected dose is high (the product of injection rate and duration). To a first approximation, it is desirable to have the blood concentration constant over the duration of a 3D acquisition. It is conventional wisdom that the most important part of the 3D acquisition is when the center of k-space is acquired and that the peak Gd concentration should coincide with that. This is true, but the rest of k-space is not irrelevant and if the Gd concentration changes dramatically during the data acquisition, a type of image blurring or 'k-space' filtering occurs. If one injects a reduced amount of contrast at the same rate, one can decrease the acquisition time to match the shortened duration of the bolus passage. Using a short TR and a short TE, time-resolved imaging can acquire data dynamically as the contrast passes through the vasculature of interest. In practice, time-resolved acquisitions such as *syngo* TWIST shorten the acquisition time and are well suited for low dose ceMRA. This does require gradient performance and a very short TR. Alternatively, if the acquisition time cannot be shortened, a reduced amount of contrast agent can be diluted to a greater volume to extend the duration of the bolus. There will be less blood T1-shortening related to the lower contrast concentration resulting in a reduction of signal intensities as shown in

1

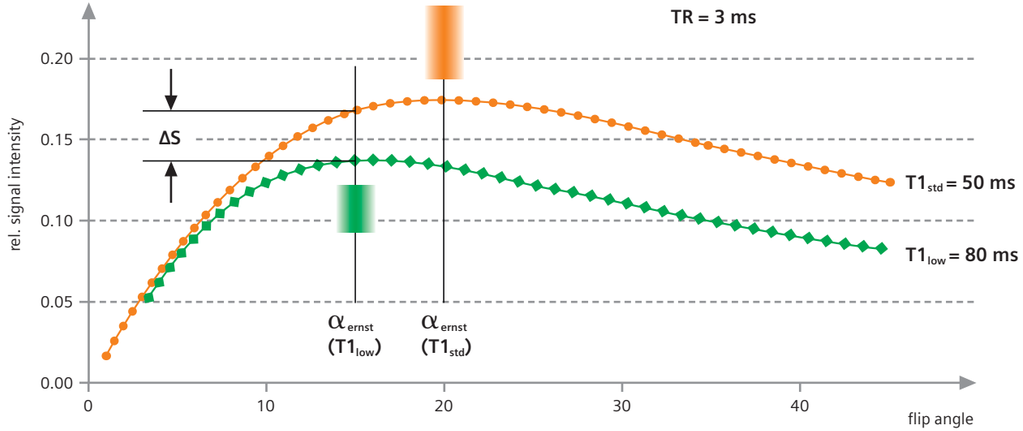

1 A standard dose can shorten the T1 of blood to about 50 ms. For a gradient echo sequence with a TR of 3 ms the optimal flip angle is around 20° (Ernst angle). Due to SAR limitations, particularly at 3T, the flip angle needs to be reduced in practical situations. Alternatively, a lower concentration can be used resulting in longer T1 times (80 ms). The Ernst angle is lower, and will not increase the SAR limits. Effectively, there is only a small loss in signal intensity well tolerable in light of the reduction of overall contrast dose.

2A

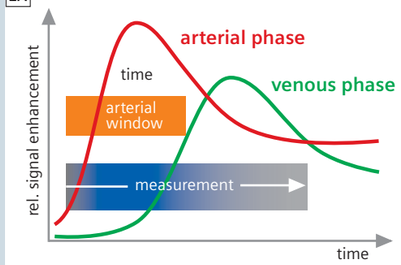

2B

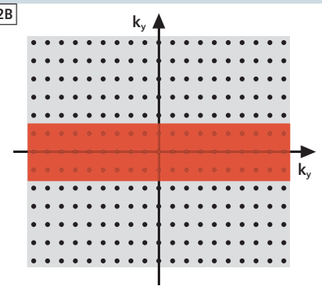

2C

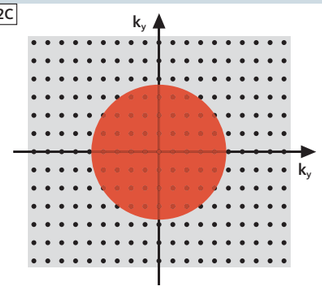

2 A typical enhancement time dynamics for arteries and veins following injection of bolus dose. The time between the arterial and venous enhancement, referred to as arterial window, is usually a fraction of the acquisition window for the MR angiogram (shown in the diagram). Different k-space acquisition order can be used, such as 1) linear or 2) flexible centric. Depending on the phase encode order, the arterial window may cover a different region in k-space, as shown in **B** for linear and **C** for flexible centric respectively. The flexible central phase encode order generates an isotropic coverage of k-space and is well suited for low dose contrast-enhanced MRA.

3

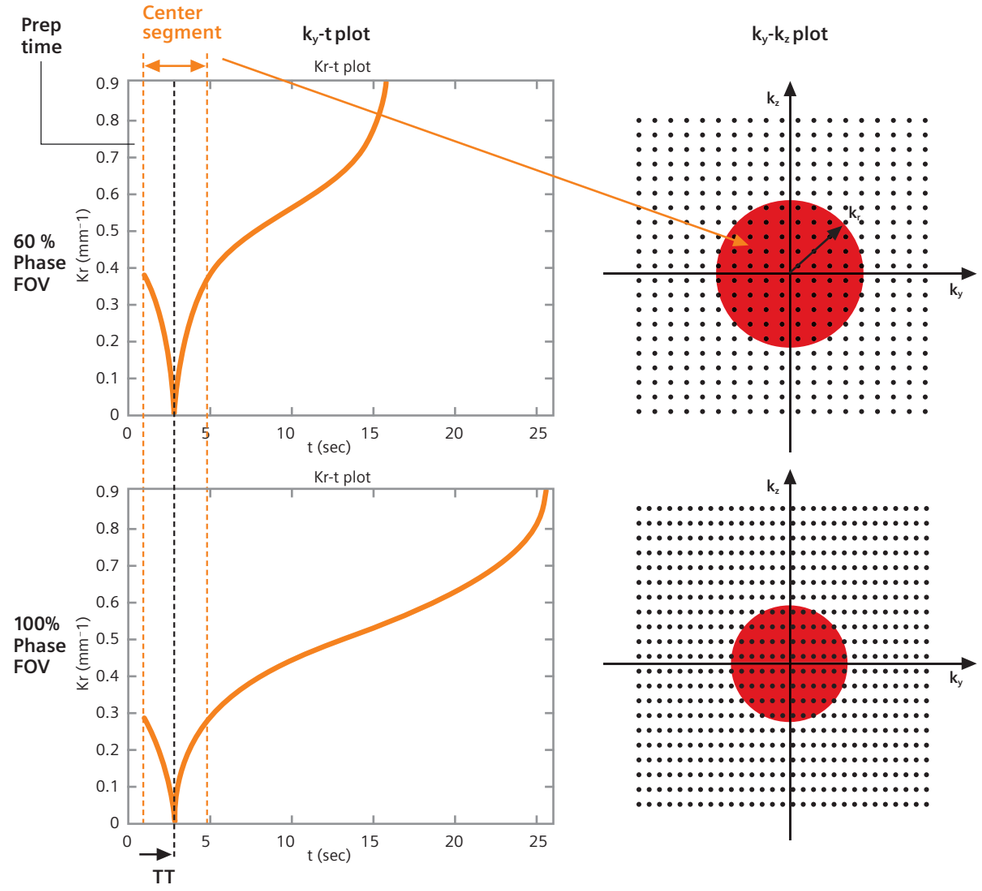

3 A schematic diagram showing delayed centric phase encoding during contrast enhancement. k_r-t plot and correspoding k_y-k_z plot of the spiral centric reordering. Shown here are two examples with 60% phase FOV (top row) and 100% phase FOV (bottom row). The time-to-center (TTC) of 3 seconds stays the same independent of the phase FOV. The sequence (product and WIP) incorporates a 1-second prep time to make sure that the magnetization is in steady state. The duration of the center segment corresponds to (TTC – prep time) x 2, i.e. 4 seconds in the case shown here.

Fig. 1. However, most protocols at 3T are SAR-limited anyway, and flip angles are usually below the Ernst angle for which maximal signal is expected. In this situation, a lower concentration with slightly longer T1 times can be used, and the signal loss compared to the higher concentration case is minimal because the Ernst angle is getting smaller for longer T1 times. Particularly at 3T, low-dose ceMRA with diluted contrast is quite effective. At 1.5T, the RF power is considerably lower, and larger flip angles in combination with higher contrast concentration than at 3T are used. In either case, one needs to take into consideration the matching of the data acquisition to the contrast passage. Careful timing between bolus arrival and k-space coverage is particularly important when performing low dose ceMRA (Fig. 2A). Fig. 1B shows the conventional linear approach in covering k-space whereas Fig. 1C shows the centric approach. Better results are obtained using the centric approach that generates isotropic coverage of the k_y-k_z space during the targeted contrast phase (e.g. the arterial window as shown in Fig. 2A, and the corresponding k_y-k_z space coverage as shown in 2C).

For ceMRA using a test bolus, a delayed measurement of the center of k-space is preferable. The order of k-space points in the centric reordering is changed such that the k-space point at $k_r = 0$ is scanned after a user-defined time called time-to-center (TTC). The delayed centric reordering starts the k-space trajectory at the edge of the center segment moving towards $k_r = 0$, then moves outwards again to acquire the complete center segment in 2 equal length paths. The trajectory then acquires the region outside of the center segment to complete the k-space dataset. The details of the delayed centric reordering are outlined in Fig. 3.

It is important to note that the TTC is independent of other geometric parameters used in the imaging protocol. For example, if the phase field-of-view (FOV) is increased from 60% to 100% as shown in Fig. 3, the TTC will not be changed. What happens instead is a corresponding size (area) reduction of the center segment in k-space, while the number of k-space points in the center segment stays the same, independent of the actual value for the phase FOV.

Similarly, changing other parameters (e.g., phase and slice resolution, or the number of slices) will not change the selected value for TTC. This has important practical implications; the center segment can be adjusted to the arterial window as demonstrated in Fig. 2 independent of the geometric parameters in the protocol.

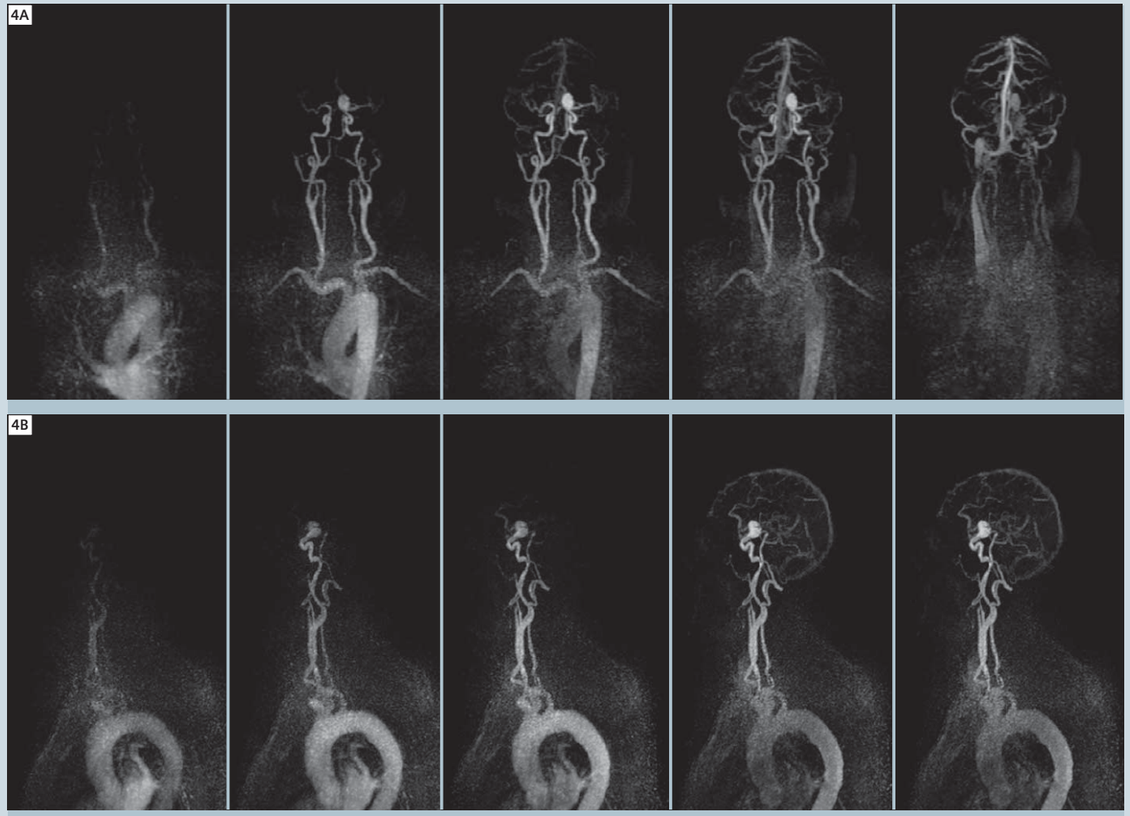

4 Dynamic and static MRA of an 81-year-old woman with unruptured left anterior choroidal artery aneurysm. **A** and **B** are coronal and sagittal maximum intensity projections reconstructed online from the dynamic 3D isotropic dataset acquired every 1.6 seconds with an injection of 1.5 cc contrast (diluted to 6 cc). (TR/TE: 2.03/0.83, FA 13°, GRAPPA × 6).

Table 3: Sample clinical applications of ceMRA

Head and Neck	Chest	Abdominal
■ Atherosclerosis ■ Aneurysm ■ AV Fistula ■ AVM ■ Vasculitis ■ Pre- and Post-Surgical assessment of tumor	■ Assessment of thoracic aorta for atherosclerosis, coarctation, aneurysm, dissection and extravasation ■ Pulmonary HTN ■ Pulmonary AVM ■ Congenital heart diseases ■ Pulmonary perfusion ■ Lung tumors ■ Pulmonary venous mapping ■ Pulmonary embolism	■ Assessment of abdominal aorta and all its branches, coarctation, aneurysm, dissection and extravasation ■ Aneurysm ■ AV Fistula ■ AVM ■ FMD ■ Pre- and Post-Surgical assessment of tumor ■ Vasculitis ■ Vascular graft

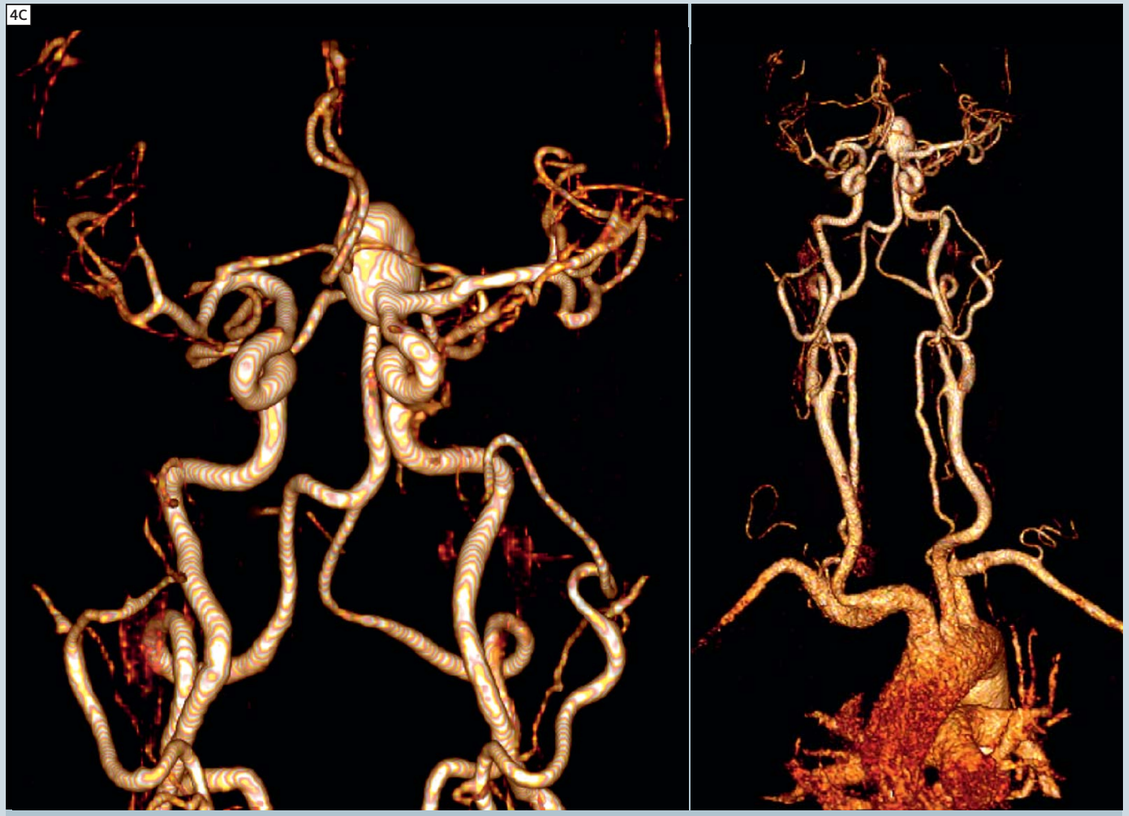

4C Volume rendered reconstructed image from high spatial resolution static MRA. First pass MRA was acquired with infusion of 8.5 cc contrast agent (diluted to 34 cc). (TR/TE: 2.61/1.16, FA 15°).

Protocols

Currently, various institutions perform ceMR angiography differently: using different sequences and parameters, different amounts and concentrations of contrast agent, and different injection and acquisition timing. The key to success is optimal coverage of the central k-space data during maximal contrast enhancement. We have experimented with different approaches and the following have worked well for all clinical application of ceMRA in different vascular territories (Table 3) using low dose ceMRA.

Head and neck low dose ceMRA

We always perform a bolus timing study with *syngo* TWIST and about one ml of Gd as described in detail previously. Fig. 4 shows a head and neck ceMRA in a patient with a body weight of 65 kg. For high spatial resolution ceMRA, a dose of 8.5 ml native Gd solution (Magnevist) was diluted with 25.5 ml of normal saline to a 34 ml bolus solution and injected at 2 ml/s. The infusion duration is therefore, 15 seconds. Typically, we acquire 128 slices with near isotropic resolution (voxel size = 0.8 mm x 0.7 mm x 0.8 mm) in a scan time of 23 seconds. Using the head and neck neurovascular coil, we normally use a FOV of 450 mm x 270 mm. This extended FOV covers the aortic arch, the origins of the great vessels, the carotid arteries, and the intracranial vasculature completely in one single injection. Parallel imaging (iPAT GRAPPA = 4) is used. The best results are obtained with breath-holding, which minimizes respiratory motion in the upper thorax and aortic arch.

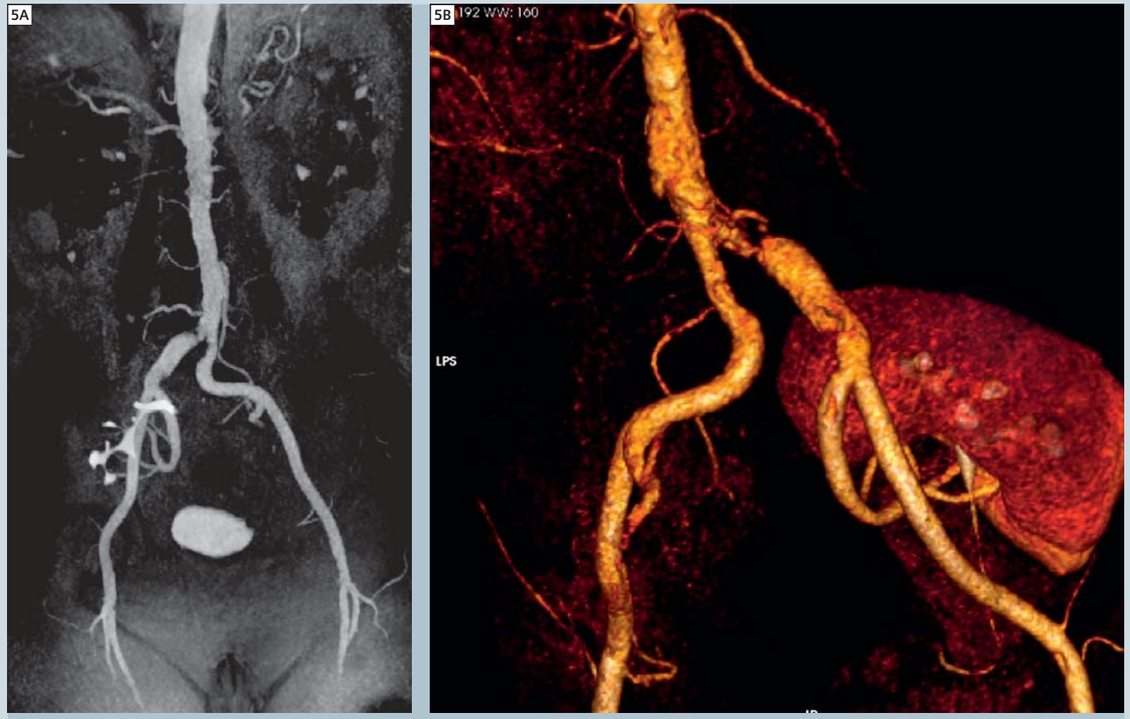

5 "Transplant Renal Artery Pseudo-Stenosis": Full thickness MIP **(A)** and volume rendered **(B)** images were reconstructed from high spatial resolution MRA in a 76-year-old male with hypertension and abnormal Doppler waveform in the transplant kidney. Images were acquired at 3.0 Tesla with infusion of 16 ml of gadolinium diluted with 34 ml of saline. Note right common Iliac artery focal high-grade stenosis with post stenotic dilatation (arrowhead). The transplant renal artery is normal. TR/TE 2.8/1.6, FA 17°, GRAPPA × 4.

Renal low dose ceMRA

For high spatial resolution renal ceMRA at 3.0T, we typically use about 10 ml native Gd formulation, diluted with 30 ml of saline. Fig. 5 shows a renal ceMRA acquired using parallel imaging with an acceleration factor of 4, therefore in this case slightly higher contrast is used. Typically, we acquire 128 slices with near isotropic resolution (voxel size = 0.9 mm x 0.8 mm x 0.9 mm, FOV is 500 mm x 300 mm) in a scan time of 21 seconds. Parallel imaging (iPAT GRAPPA = 3) is used. Patients must hold their breath during the scan to minimize motion artifact in the abdomen.

Peripheral low dose ceMRA

For low dose peripheral ceMRA, we typically acquire 128 slices with a voxel size of 0.9 mm x 0.8 mm x 0.9 mm in a scan time of 26 seconds. Parallel imaging (iPAT GRAPPA = 4) is used. While peripheral MRA is often performed using a single injection, the dual injection scheme is the method of choice at UCLA. The first contrast injection is used to image the calf station and a second injection for abdomen and thighs. This approach guarantees a pure arterial phase with no venous contamination in the calves, regardless of vascular transit times. Patients are positioned feet first into the magnet bore. A three-station, dual-injection protocol is used with image acquisition performed first in the calves before the pelvis and thighs. A 500 mm FOV is used for each station, covering a total length of 1350 mm along the patient axis. There is typically a 10 cm overlap between the abdominal and thigh stations and a 5 cm overlap between the thigh and calf stations. For the abdominal-pelvic station, patients are requested to hold their breath to minimize motion in the lower abdomen. The amount of contrast we typically prepare and use is as shown in tables 1 and 2 for single station as well as multi-station acquisitions. In anticipation of potential asymmetry in contrast arrival in each calf, which can occur with vascular diseases, three sequential post-contrast MRA data sets are acquired routinely per calf station and two sets per thigh station. To eliminate stationary background signal, the pre-contrast images are used as masks and are subtracted from the contrast-enhanced MRA images in the calves and thighs. Subtraction is less successful and less useful in the abdomen. Figs. 6 and 7 show clinical examples of low dose peripheral ceMRA acquired at 3T.

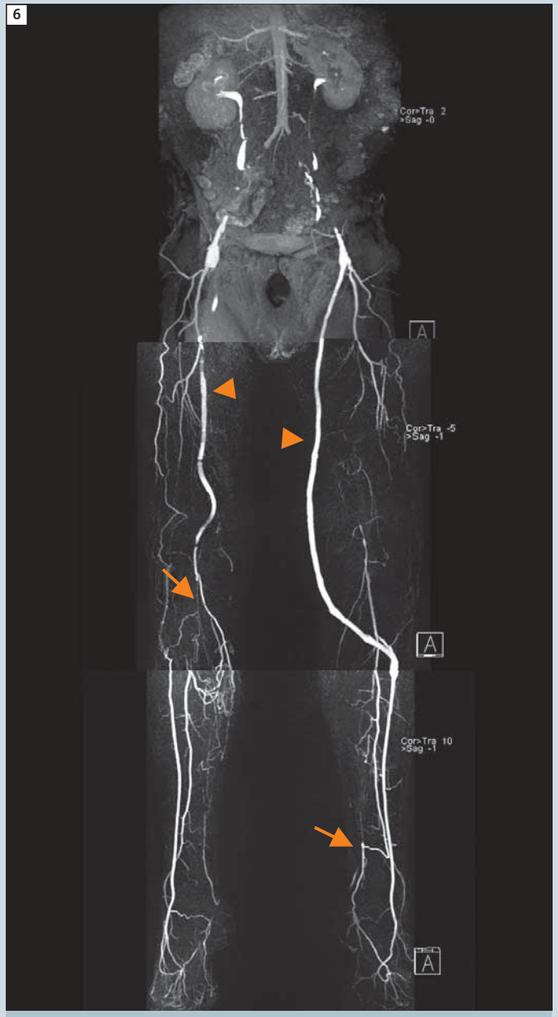

6 Full thickness MIP images from low contrast dose, 3 station MRA in a 64-year-old male patient with extensive severe peripheral vascular disease including: bilateral femoropopliteal bypass (arrowheads), bilateral common iliac stents, bilateral external artery stents and stent-graft placement for occluded right proximal femoral-popliteal graft.
Right Popliteal artery (arrow in thigh station) above the knee joint shows diffuse narrowing with occlusion at knee joint line. Left Popliteal artery is diminutive and widely patent. Right Tibioperoneal Trunk is occluded. Right and left Peroneal gives off collateral vessels, which reconstitute distal posterior tibial arteries (just above the ankle joint). Right and left posterior Tibial arteries are occluded in proximal and mid-calves. Images were acquired at 3.0 Tesla, with a dual injection protocol: 7 ml of contrast agent (21 ml of solution) for the calf station and 11 ml of contrast agent (33 ml of solution) for the thigh and abdominal stations. Sequence parameters: TR/TE 2.53/0.95, FA =13° for abdomen, 3.85/1.2, 36° for the thigh station and 3.13/1.16; 17° for the calf station.

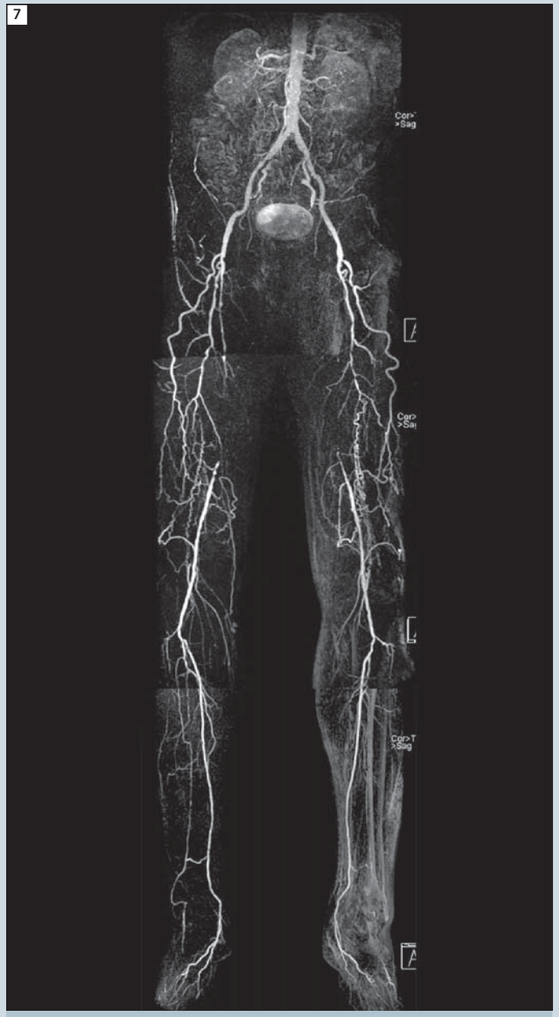

7 Full thickness MIP images from 3.0T low contrast dose, high spatial resolution (static) MRA, in a 69-year-old man with bilateral lower limb claudication. Images were acquired with a dual injection protocol: 7 ml of gadolinium (diluted to 21 ml) for the calves and 11 ml of gadolinium (diluted to 33 ml) for the abdomen-thigh stations. Sequence parameters: TR/TE 2.53/0.95, FA =13° for the abdominal station, 3.74/1.34, 36° for the thigh station and 3.13/1.16; 17° for the calves. Note: bilateral long segment SFA occlusion with extensive collateralization and multiple high-grade stenoses of the left profunda femoris. Furthermore there is single-vessel run-off
in the calves bilaterally with patent posterior tibial arteries.

Chest low dose MRA

Most of our chest MRA studies are performed at 1.5T as they are generally combined with cardiac functional assessment, often in patients with adult congenital heart disease. Figs. 8A–D show a chest ceMRA in a patient with pulmonary atresia and hypoplastic right lung.

Generally we perform a sagittal bolus timing study with *syngo* TWIST using one ml of Gd. Next we perform a coronal time resolved study using the TWIST sequence with an injection of 3 ml contrast at a rate of 3 ml/sec. For high spatial resolution ceMRA, a dose of 16 ml Gd (Magnevist) is diluted with equal amount of normal saline to create a 50% solution and injected at 2 ml/s. Images are acquired during approximately 20 seconds of breath-holding.

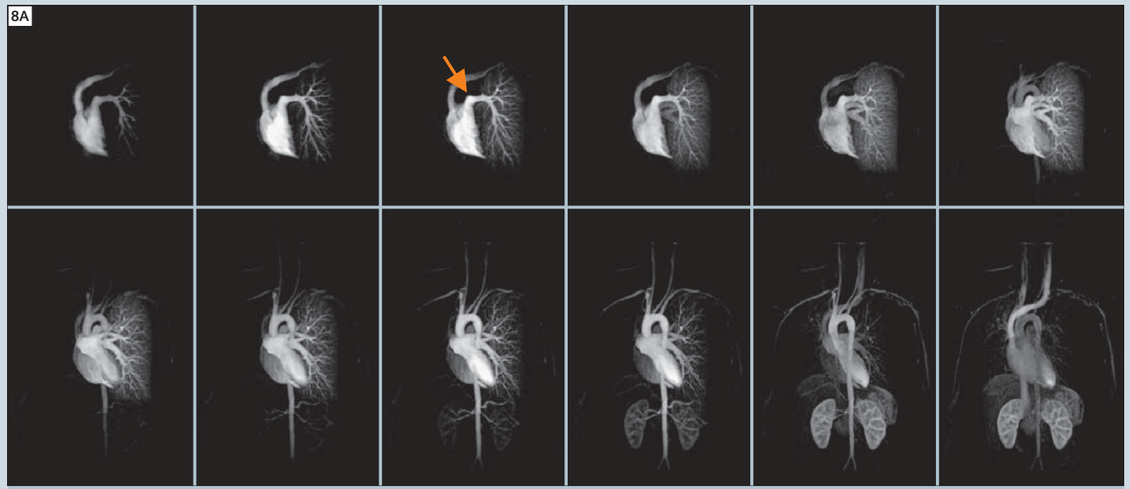

8A Dynamic MRA on the 1.5T MAGNETOM Avanto of an 18-year-old female with hypoplastic right lung and atresia of the right pulmonary artery (arrow points to the single left pulmonary artery). Right pulmonary parenchyma is perfused from an inferior phrenic artery and bronchial arteries. Images were acquired with 6.0 ml of contrast agent (diluted to 12 ml). TR/TE: 2.45/0.92, FA 25°.

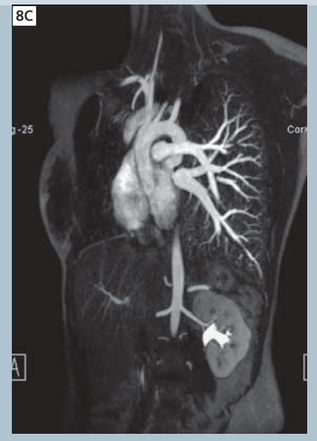

8B–D Left anterior oblique **(B)**, right anterior oblique **(C)** thin MIP images and volume rendered image **(D)** were reconstructed from static high spatial resolution MRA of the above patient with injection of 14 cc of contrast agent. Note complete absence of the right pulmonary artery. TR/TE: 2.28/0.95, FA 30°.

Pediatric body ceMRA

We perform pediatric ceMRA at both systems (1.5 and 3T) under general anesthesia. Fig. 9 is a one-day-old baby with patent ductus arteriosus scanned at 1.5 Tesla with 1.25 ml of contrast diluted with 4.75 ml saline. Fig. 10 is an image of a two-day-old infant with infantile type coarctation, acquired at 3.0 Tesla using 1.25 cc of contrast diluted with 4.75 ml of saline. Although a very small volume of contrast was used, this is still not 'low dose' by adult standards. In these specific cases, the practical challenges of delivering very small volumes through an adult delivery device made it difficult to optimize the injected dose, even when diluted. This shortcoming can be addressed with dedicated, low volume pediatric delivery tubing and devices.

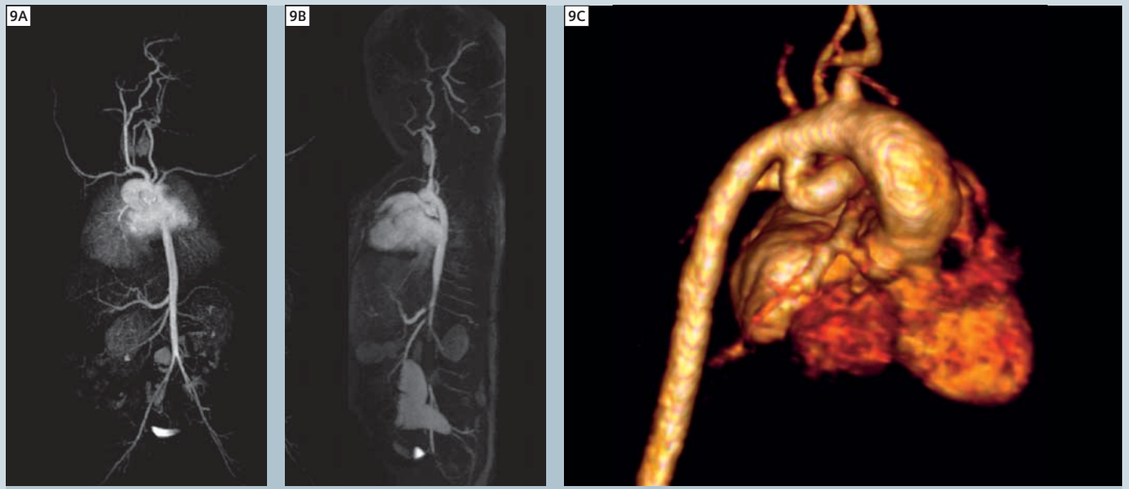

9 Full thickness MIP **(A)**, partial MIP **(B)** and volume rendered **(C)** images were reconstructed from high spatial resolution MRA of a one-day-old infant girl. Images were acquired at 1.5 Tesla system with infusion of 1.25 ml of gadolinium diluted with 4.75 ml of saline). Ascending aorta and arch demonstrate an abnormal posterior course. Note the large patent ductus arteriosus (6.5 mm) in VR image. TR/TE 2.96/1.7 FA 30° GRAPPA × 3.

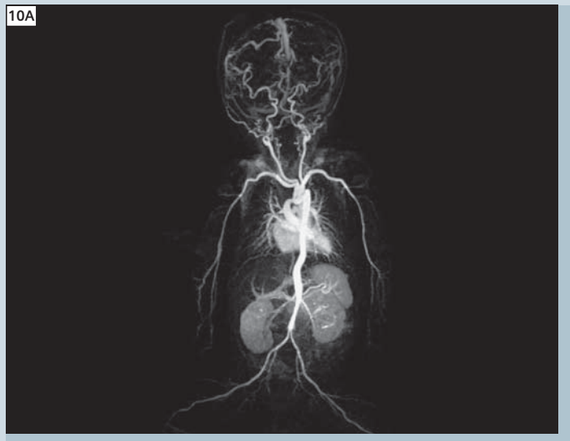

10 Full thickness MIP **(A)** and volume rendered **(B)** images were reconstructed from high spatial resolution MRA of a two-day-old infant boy. Images were acquired at a 3T system with infusion of 1.25 ml of gadolinium diluted with 4.75 ml of saline). Aortic arch and distal ascending aorta are diffusely hypoplastic (infantile-type coarctation). TR/TE 3.02/1.17, FA 20°, GRAPPA × 4.

Image visualization

In addition to data acquisition, image processing and visualization is very important. In situations where there is limited vessel contrast and signal-to-noise ratio (SNR), the thin-MIP (thin maximum-intensity-projection) method is advantageous as it takes MIP projections from a targeted number of thin slices to create a 10-20 mm slab. This minimizes background tissue signal and increases the vessel contrast. This has generated excellent results in different vasculatures.

Summary

Low dose ceMRA can be performed successfully and routinely in clinical practice. The most dramatic dose reduction protocols are possible at 3T, where the trade-off in vascular signal with dose reduction is well tolerated. Low dose ceMRA, using < 10 ml of contrast agent, instead of 30 ml or more, is made practical by diluting the native contrast formulation and leaving the infusion rate unchanged.

Acknowledgement

The authors would like to acknowledge Sergio Godinez, Francine Cobla and Glenn Nyborg for performing the clinical examinations.

Contact
Prof. J. Paul Finn, M.D.
The David Geffen School
of Medicine at UCLA
Chief, Diagnostic
Cardiovascular Imaging Section
Director, Magnetic Resonance Research
Los Angeles, CA
USA
pfinn@mednet.ucla.edu

References

1 Cowper, S.E., et al., Scleromyxoedema-like cutaneous diseases in renal-dialysis patients. Lancet, 2000. 356(9234): p. 1000-1.
2 Grobner, T., Gadolinium – a specific trigger for the development of nephrogenic fibrosing dermopathy and nephrogenic systemic fibrosis? Nephrol Dial Transplant, 2006. 21(4): p. 1104-8.
3 Morcos, S.K., H.S. Thomsen, and J.A. Webb, Dialysis and contrast media. Eur Radiol, 2002. 12(12): p. 3026-30.
4 Kribben, A., et al., Nephrogenic systemic fibrosis: pathogenesis, diagnosis, and therapy. J Am Coll Cardiol, 2009. 53(18): p. 1621-8.
5 van der Molen, A.J., Nephrogenic systemic fibrosis and the role of gadolinium contrast media. J Med Imaging Radiat Oncol, 2008. 52(4): p. 339-50.
6 Othersen, J.B., et al., Nephrogenic systemic fibrosis after exposure to gadolinium in patients with renal failure. Nephrol Dial Transplant, 2007. 22(11): p. 3179-85.
7 Abujudeh, H.H., et al., Nephrogenic Systemic Fibrosis after Gadopentetate Dimeglumine Exposure: Case Series of 36 Patients. Radiology, 2009.
8 Liu, X., et al., Renal transplant: nonenhanced renal MR angiography with magnetization-prepared steady-state free precession. Radiology, 2009. 251(2): p. 535-42.
9 Robert R. Edelman, I.K., Renate Jerecic, Xiaming Bi (Spring 2009) Non-Contrast Renal MR Angiography, a case study. CMRS e-Vision.
10 Du, Y.P., et al., Multi-echo acquisition of MR angiography and venography of the brain at 3 Tesla. J Magn Reson Imaging, 2009. 30(2): p. 449-54.
11 Francois, C.J., et al., Unenhanced MR angiography of the thoracic aorta: initial clinical evaluation. AJR Am J Roentgenol, 2008. 190(4): p. 902-6.
12 Francois, C.J., et al., Pulmonary vein imaging with unenhanced three-dimensional balanced steady-state free precession MR angiography: initial clinical evaluation. Radiology, 2009. 250(3): p. 932-9.
13 Wyttenbach, R., et al., Renal artery assessment with nonenhanced steady-state free precession versus contrast-enhanced MR angiography. Radiology, 2007. 245(1): p. 186-95.
14 Habibi, R., et al., High-spatial-resolution lower extremity MR angiography at 3.0 T: contrast agent dose comparison study. Radiology, 2008. 248(2): p. 680-92.
15 Lohan, D.G., et al., Ultra-low-dose, time-resolved contrast-enhanced magnetic resonance angiography of the carotid arteries at 3.0 tesla. Invest Radiol, 2009. 44(4): p. 207-17.
16 Tomasian, A., et al., Supraaortic arteries: contrast material dose reduction at 3.0-T high-spatial-resolution MR angiography-feasibility study. Radiology, 2008. 249(3): p. 980-90.

Case Report: Cardiac Imaging with MAGNETOM ESSENZA

Cardiac MRI of Anteroapical Infarction in Patient with Left Ventrical Aneurysm with Apical Thrombus/Tako-Tsubo like Syndrome

G. Hadjidekov; G. Tonev

MC "Pro-Vita", Sofia, Bulgaria

Introduction

Left ventricle aneurysm is an uncommon finding on MR cardiac examinations. We describe a case of aneurismal dilatation of the left ventricle with apical thrombus formation and confirmation of this thrombus, suspected on echocardiography by cardiac magnetic resonance imaging (CMR). Perfusion and late enhancement techniques contributed to the detection of chronic anteroapical infarction.

Patient history

42-year-old man with ischemic heart disease, NYHA class II, persistent atrial fibrillation and aneurismal dilatation of the left ventricle with suspicion of thrombus underwent CMR. The patient was admitted to the hospital with cough, roaring and orthopnoe as well as pulmonary edema. Echocardiography revealed a dilated left ventricle with hypokinesis of the anterior wall and the septum, severe apical hypokinesis and a reduced ejection fraction (EF) of 29%, consistent with the diagnosis of tako-tsubo cardiomyopathy (TTC) [1]. Additionally performed coronary angiography did not show significant coronary artery disease. The patient was than referred to CMR for further evaluation.

Sequence details

Images were acquired on our 1.5T MAGNETOM ESSENZA using the 6-element Body Matrix in combination with the integrated IsoCenter Matrix coil. The following sequence parameters have been used:
TrueFISP: TR 54.6 ms, TE 1.6 ms, matrix 256/192, FOV 340 / 276 mm, bandwidth 930 Hz/px, flip angle 80°, resolution 192 / 134.
Dynamic perfusion evaluation using gradient echo sequences: TR 167.48 ms, TE 1.21 ms, matrix 256/192, TI 100 ms, FOV 360 / 293 mm, bandwidth 651 Hz/px, flip angle 12°, resolution 160 / 120.
Late enhancement using psir-single-shot sequences: TR 936 ms, TE 3.39 ms, TI 370 ms, matrix 256 / 192, FOV 340 / 276 mm, bandwidth 140 Hz/px, flip angle 25°, resolution 256 / 179.

Imaging findings

Cardiac MRI shows a dyskinetic aneurismal anterior and apical left ventricular wall on the TrueFISP cine images in diastolic and systolic two-chamber, three-chamber and four-chamber views, as well as the left ventricle outflow tract (Figs. 1A, B, C, D). The presence of an aneurismal dilatation of the left ventricle and a small adjacent thrombus, measuring 11 by 9 mm in diameter, are demonstrated. There is also a small pericardial effusion. The same findings are clearly demonstrated on short-axis (SA) views (Fig. 5) from base to apex. Figures 3 and 4 present the dynamic sequences in four-chamber view (Fig. 3) and short axis and left ventricle long axis views (Fig. 4) with visualisation of the apical thrombus at the level of the anteroapical ventricular aneurysm. The post-contrast acquired inversion recovery images (Fig. 2) show transmural enhancement of the left ventricular apex and part of the anterior wall, which is indicative of a scar. On late enhancement images we observe hyperintense transmural involvement of the segments 17, 14 and partly 13. A dark low-signal-intensity mass is visible adherent to the aneurismal enhanced and scarred myocardium. The left ventricle was dilated and measured 92 by 66 mm in end-diastole and the ejection fraction (EF) was reduced at 32%, which corresponded to the values, measured in echocardiography. The septum thickness is 18 mm.

Discussion

In the past, spoiled gradient-echo (GRE) imaging techniques with the use of flip angles less than 90° offered significantly shorter imaging time than spin echo sequences for cardiac imaging [2]. In TrueFISP sequences the higher signal-to-noise ratio (SNR) allows rapid data acquisitions with very short TR values in the range of 3–5 ms. This sequence provides a high contrast between blood and myocardium with excellent delineation of anatomic structures such as papillary muscles, endocardial trabeculation and valve leaflets, making thus suited for the evaluation of wall-motion abnormalities

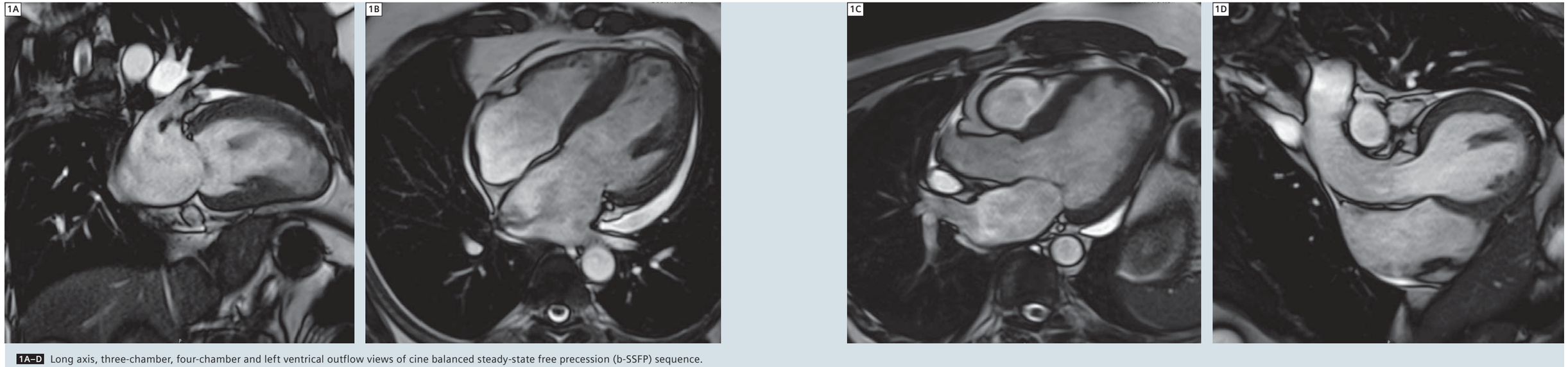

1A–D Long axis, three-chamber, four-chamber and left ventrical outflow views of cine balanced steady-state free precession (b-SSFP) sequence.

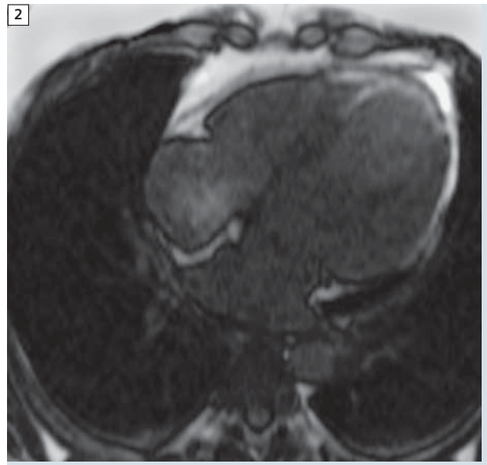

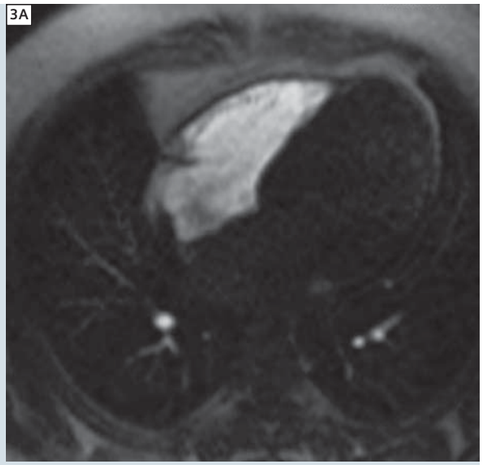

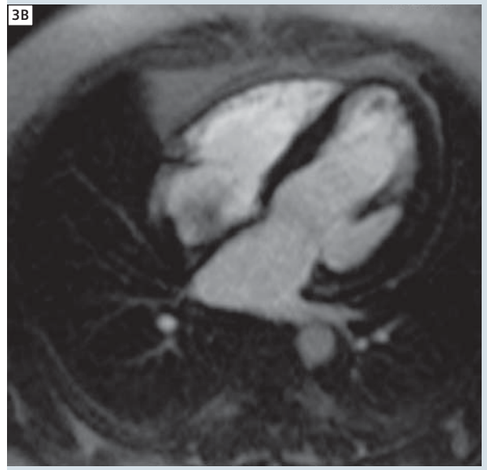

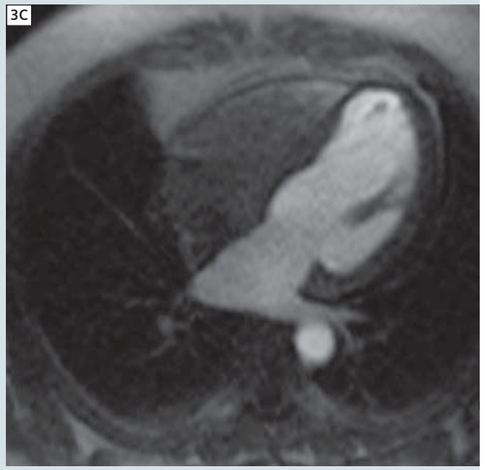

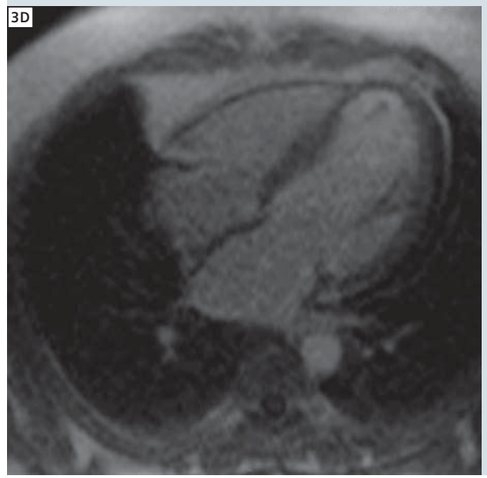

2 Four chamber late enhancement images showing the infracted areas.

3A–D Four-chamber views of the perfusion sequence clearly demonstrating the small apical thrombus at the level of the anteroapical ventricular aneurysm.

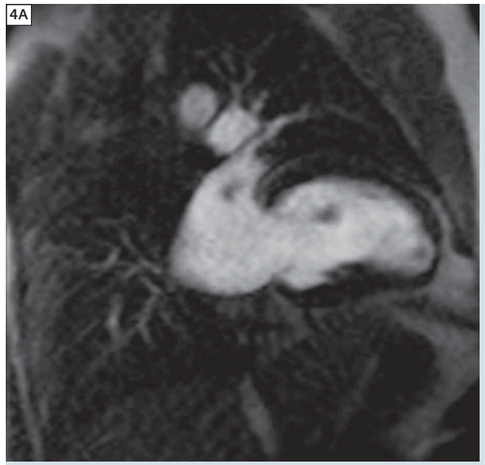

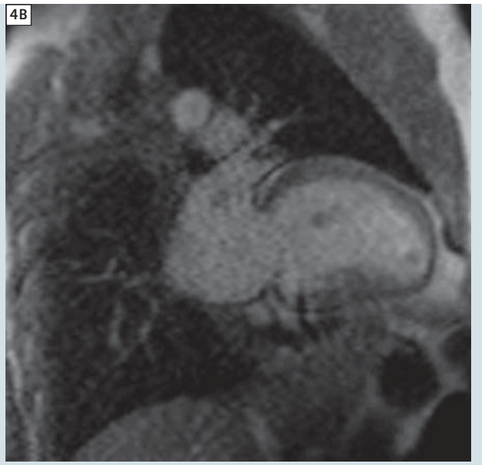

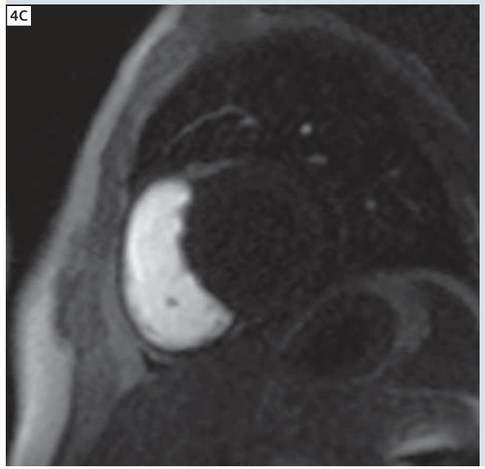

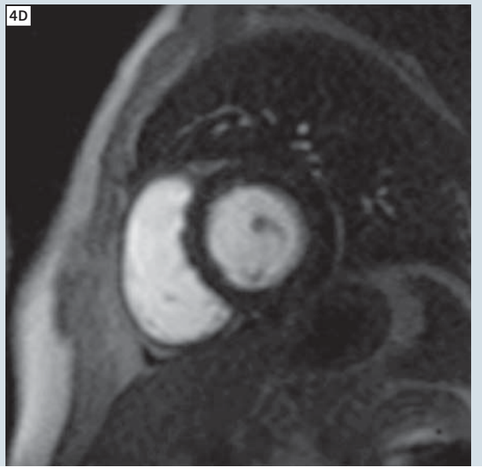

4A–D Left ventricle long axis views demonstrate the aneurysmal dilatation of the left ventricle and the small apical thrombus **(A, B)**. Perfusion sequence at short axis views **(C, D)**.

[3, 4]. Parallel imaging techniques substantially reduce imaging time and therefore are often combined with sequences with high SNR, and the synergistic effect in terms of speed of data acquisition reduces the overall examination time [5, 6]. Real-time cardiac imaging permits examination of patients with cardiac arrythmia and incapable of breath holding without the need of cardiac- or respiratory-motion compensation [7]. Recent studies compare contrast-enhanced cine-MR sequences to pre-contrast cine-MR sequences in the assessment of left ventricular function providing comparable quantitative data upon regional contractile function [8]. The authors suggest the use of contrasts enhanced cine True-FISP sequences between the first-pass and delayed enhancement sequences to reduce the overall examination time. In terms of identification of left ventricular thrombus ceMRI has a higher sensitivity and specificity than transthoracic echocardiography (TTE) and transesophageal echocardiography (TEE) [9, 10, 11]. Delayed enhancement ceMRI techniques using an inversion recovery pulse to suppress signal are particularly beneficial in detecting intracavitary thrombi in addition to being an excellent technique for depicting adjacent myocardial infarction and scars. This imaging technique allows the visualization of small thrombi, which can often be invisible on TEE. In our experience, the presence of slow and turbulent flow patterns in dysfunctional wall segments and a lack of contrast between a small mural thrombus and the adjacent myocardium may obscure the visualization of small thrombi on cine-MRI, even when using the newer TrueFISP techniques [9, 11]. In clinical practice, a combination of cine-MRI using the newer TrueFISP techniques and contrast-enhanced inversion recovery MRI with a careful analysis of the regions at risk – infarct area, aneurismal and dysfunctional wall segments of the ventricles, atrial appendages – is the best way not to miss thrombi.

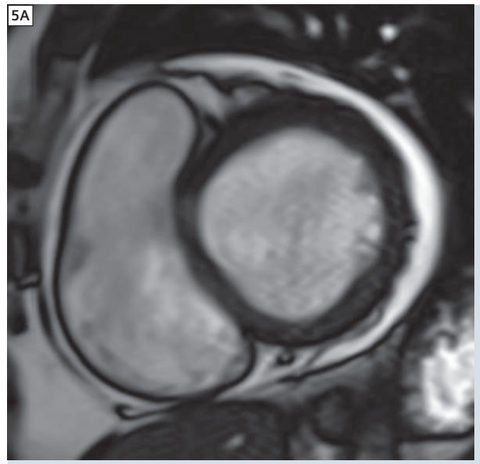

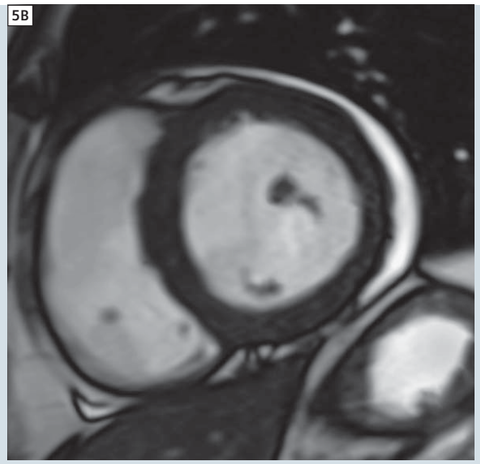

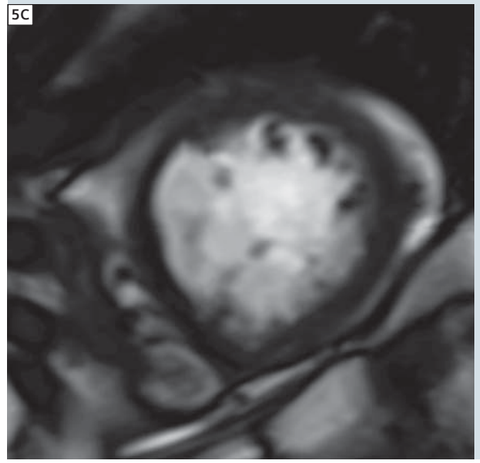

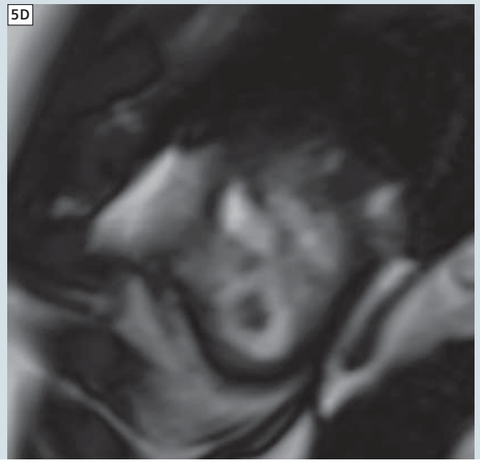

5 Short-axis views from base to apex (cine sequences).

Conclusion

As shown in this case report, cardiac magnetic resonance imaging can be used as a powerful tool in the diagnosis of thrombi and further evaluation of ischemic heart disease.

Contact
Georgi Hadjidekov, M.D.
MC "Pro-Vita"
Montevideo str. N66
Sofia 1632, Bulgaria
jordiman76@yahoo.com

References

1 G. Leurent, A. Larralde, D. Boulmier, C. Fougerou, B. Langella, R. Ollivier, M. Bedossa, H. Le Breton (2009). Cardiac MRI studies of transient left ventricular apical ballooning syndrome (takotsubo cardiomyopathy): A systematic review. International Journal of Cardiology, Volume 135, Issue 2, Pages 146-149

2 Sprung K (2005) Basic techniques of cardiac MR. Eur Radiol 15 (suppl 2): B10-B16

3 Thiele H et al (2001). Functional cardiac MR imaging with steady-state free precession (SSFP) significantly improves endocardial border delienation without contrast agents. J magn Reson Imaging 14(4):362-367

4 Barkhausen J et al. (2001) MR evaluation of ventricular function: true fast imaging with steady-state precession versus fast low-angle shot cine MR imaging: feasibility study. Radiology 219(1): 264-269

5 Pruessmann KP et al. (1999) SENSE: sensitivity encoding for fast MRI. Magn Reson Med 42(5): 952-962

6 Kyriakos WE et al. (2000) Sensitivity profiles from an array of coils for encoding and reconstruction in parallel (SPACE RIP). Magn Reson Med 44(2): 301-308

7 Weiger M, Pruessmann KP, Boesinger P (2000) Cardiac real-time imaging using SENSE. SENSitivity Encoding scheme. Magn Reson Med 43(2): 177-184

8 Lasalarie JC, Serfaty JM, Carre C, Messika-Zeitoun D, Jeannot C, Schouman-Claeys E, Laissy JP (2007) Accuracy of contrast-enhanced cine-MR sequences in the assessment of left ventricular function: comparison with precontrast cine-MR sequences. Results of a bicentric study. Eur Radiol 17(11): 2838-2844

9 Mollet NR, Dymarkowski S, Volders W, et al. (2002) Visualization of ventricular thrombi with contrast-enhanced magnetic resonance imaging in patients with ischemic heart disease. Circulation 106: 2873–2876

10 Srichai MB, Junor C, Rodriguez LL, et al. (2006) Clinical, imaging, and pathological characteristics of left ventricular thrombus: a comparison of contrast-enhanced magnetic resonance imaging, transthoracic echocardiography, and transesophageal echocardiography with surgical or pathological validation. Am Heart J 152:75–84

11 Barkhausen J, Hunold P, Eggebrecht H, et al. (2002) Detection and characterization of intracardiac thrombi on MR imaging. AJR 179:1539–1544

Assessment and Classification of Peripheral Vascular Anomalies by Time-Resolved MRA using TWIST

Ulrich Kramer[1], Ulrike Ernemann[2], Stephan Miller[1]

[1]Diagnostic and Interventional Radiology, University Hospital Tübingen, Germany
[2]Diagnostic and Interventional Neuroradiology, University Hospital Tübingen, Germany

Introduction

Vascular malformations (VM) can be classified into high-flow arteriovenous malformations and/or fistulas (AVM) and low-flow venous or lymphatic malformations. In general, VMs are congenital anomalies, usually caused by an arrest of normal vascular development and failure of resorption of the embryologic primitive vascular elements. VMs can present in any anatomic location, tissue or organ; the most common anatomic locations being the pelvis, extremities (flexor muscles of the forearm and the quadriceps muscle) and the intracranial circulation. Overall prevalence of VMs is estimated to be 1.5% of the general population.
Multiple classifications for vascular abnormalities have been established, but the classification of Mulliken and Glowacki is the most frequently used system [1, 2]. Treatment and prognosis of VMs are based on the type, subtype and architecture of the lesions.
A potential difficulty of making differential diagnoses for the lesions relying only on the above system is that diagnoses may often be incorrect, resulting in turn in inappropriate treatment. Precise imaging evaluation is needed for treatment of the lesions, not only to evaluate the extent of lesions but also to confirm the suspected diagnoses.

Diagnosis and standards of therapy

Magnetic resonance imaging (MRI) and ultrasound (US) are the noninvasive techniques of choice and can be used for the evaluation of VMs. Because of the limitations of US (small field-of-view, restricted penetration, operator dependency), MRI has emerged as an extremely important modality in the assessment of these lesions. The literature, recognizes that the extent of tissue involvement (muscles, nerves, bone, tendons, subcutaneous tissue and skin) can be accurately determined by MRI, the full extent often being underestimated by physical examination. As a consequence, exact categorization of a VM by MRI guides treatment toward percutaneous embolization, transarterial embolization or a surgical approach.
Since the diagnosis of a vascular lesion relies mainly on medical history and clinical examination, diagnostic imaging can be focused on specific structural and functional information required for treatment planning. In general, evaluation of VMs requires delineation of its components:
(1) location, size, and tissue involvement,
(2) origin, orientation, and course of feeding arteries, and
(3) origin, size, and course of the draining veins.
Due to continuous improvements in hard- and software within the last few years, time-resolved MR angiography (MRA) in particular has been gaining acceptance as a practical alternative to digital subtraction angiography (DSA) for the diagnosis and determination of appropriate treatment of VMs [3]. Time-resolved MRA has been shown to be an accurate technique to distinguish the different types of vascular anomalies [4].

MR imaging

Patients with suspicious or known AVM were studied using a 3D time-resolved contrast-enhanced (ce)MRA which incorporates Generalized Autocalibrating Partially Parallel Acquisitions (GRAPPA) and echo sharing schemes, Time Resolved Imaging with Stochastic Trajectories (TWIST). All patients were examined on a 1.5T MR system (MAGNETOM Avanto, Siemens Healthcare, Erlangen, Germany), using a multi-channel phased-array surface coil or dedicated flex extremity coils.
All scans consisted of T1 and fat-suppressed T2-weighted images. Axial conventional spin-echo (SE) and / or turbo spin-echo (TSE) T1-weighted and T2-weighted TSE images were obtained by using 5–10 mm section thickness, 1–2 mm intersection spacing, and variable field-of-view depending on the extremity. Post-contrast images were obtained in axial and sagittal and/or coronal plane following intravenous administration of 0.1 mmol/kg gadobutrol (Gadovist®, Bayer HealthCare, Germany).

Time-resolved MRA using TWIST

The TWIST sequence divides k-space into a central (A) and a peripheral (B) region. The central region (low frequencies) defines the contrast in the image and the peripheral region (high frequencies) accounts for the detail information in

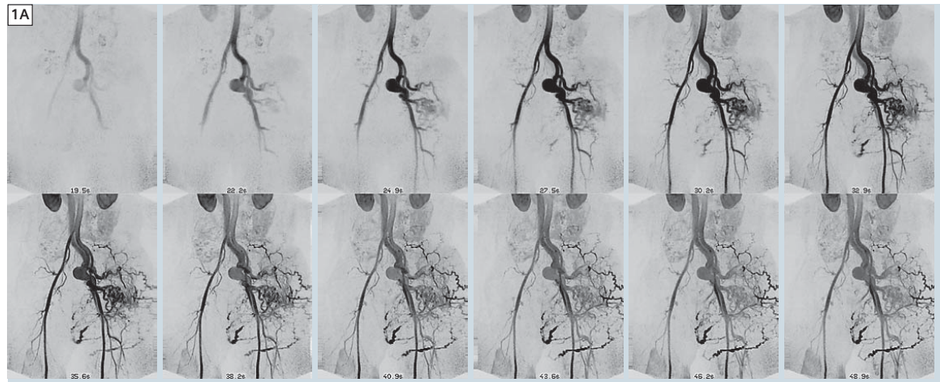

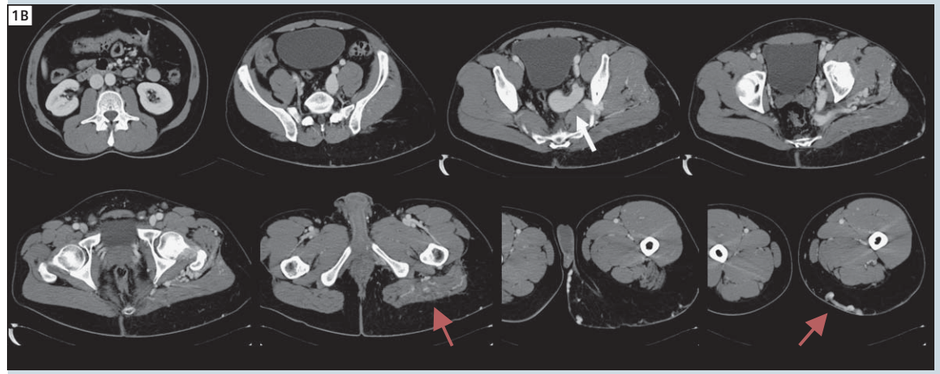

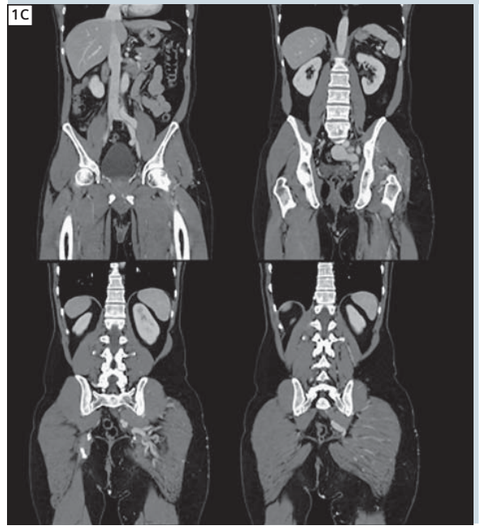

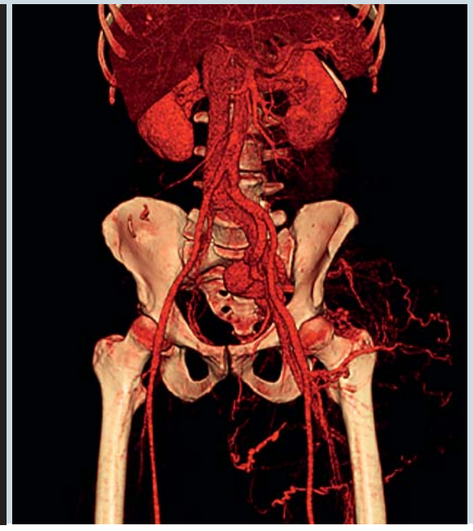

1 39-year-old male patient presented with a painful pulsating mass in the left buttock soft tissue. There is an increase in local skin temperature and a thrill when the lesion is palpated.
(1A): On time-resolved MRA an aneurysm of the intern iliac artery as well as a large VM involving the left upper thigh, buttock and lumbar region is found. Multiple feeding arteries and an early opacification of dilated outflow veins can be seen. Additional CT scan was performed in order to evaluate extent of disease and tissue involvement prior to treatment. CT images in axial **(1B)** and coronal **(1C)** orientation confirmed diagnosis demonstrating a number of prominent arteries and arterioles mainly in the left gluteus muscle and multiple huge dilated and early draining veins in the subcutaneous layer, compatible with a high-flow arteriovenous malformation.

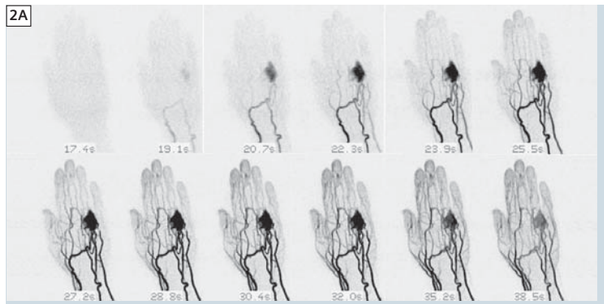

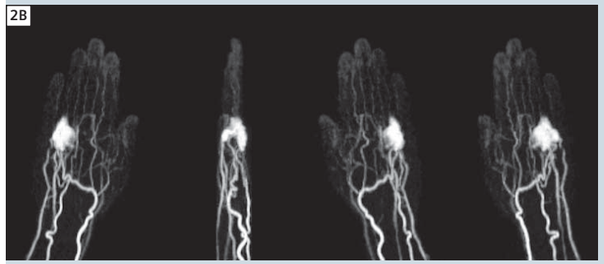

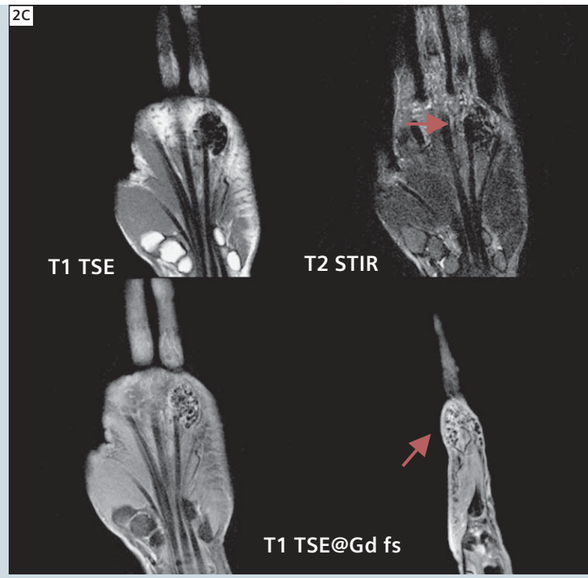

2 46-year-old female patient presenting with a high-flow AVM of the right hand. **(2A)** On time-resolved MRA (2.7 s/frame) feeding arteries of the radial and ulnar artery as well as an enlarged dorsal draining vein can be observed. **(2B)** Due to high-spatial resolution (in-plane resolution (1.3 x 1.3) mm^2, slice thickness 1.3 mm), multiplanar reformatted views obtained from a single dataset allow for more precise evaluation of vascular pathology in addition to viewing the standard MIP in the acquired plane. **(2C)** Morphological images showed subcutaneous hypointens mass on T1w as well as T2w sequences. Fast flow vessels are also identified by the presence of flow voids within the mass (open arrow). There is no enhancement after application of gadobutrol (lower row).

the images. While region A is completely sampled for every measurement repetition, region B is undersampled by a factor of n, which can be varied by the operator. The larger the undersampling factor the shorter the time difference for two consecutive acquisitions of the central region. The k-space trajectory within region B follows a spiral pattern in the k_y-k_z plain with every trajectory in B slightly different, depending on the undersampling factor n. During reconstruction, the missing data points in region B for a particular time frame t_i will be copied from the corresponding k-space trajectories in other time frames. The following sequence parameters were used: TR 2.27-3.46 ms, TE 0.8-1.29 ms (depending on patient adjustment), flip angle (FA) 25°, sampling bandwidth (BW) 650-950 Hz/pixel; in-plane reso lution 1.1 x 0.8 mm^2, slice thickness 1–3 mm. In our study we have used a value of 15% for region A, and an undersampling factor of 25% for region B.

Discussion

The TWIST technique has special advantages for MR imaging of VMs, because it provides information on the hemodynamics of the malformations, demonstrating the early filling of the lesion during the arterial phase of the acquisition as well as – where relevant – the feeding artery. The use of parallel imaging techniques in association with the variable rate k-space sampling allows a reduction of acquisition time, improving the temporal resolution while maintaining and even improving the spatial resolution. In our study protocol the temporal resolution was varying from 4.8 to 1.4 seconds per single frame and the spatial resolution ranged from (1.1 x 0.8 x 1.0) mm^3 to (1.1 x 1.1 x 3.0) mm^3.
A high acceleration factor of 3 was used for parallel imaging in most applications. Thus, we have been able to obtain detailed anatomical and hemodynamic information similar not only to conventional high-spatial resolution MRA but also to that obtained with DSA, but without the risks associated with ionizing radiation exposure, iodizing contrast agents, or catheterization itself.

Clinical implication

In general, whilst differentiation between a vascular malformation and a hemangioma can often be obtained clinically, MRI will be useful in this regard in several cases. Diagnostic imaging is often required for the evaluation of deeper lesions or in the setting of an atypical history to allow differentiation from other malformations or non-malformation lesions. As a result, MRI has become the imaging modality of choice in the assessment of morphological issues of VMs, e.g. extent of the lesion, tissue involvement and flow characteristics (signal voids in high-flow lesions). At our institution, based on these initial results, time-resolved MRA will influence therapeutic decision making by defining the internal architecture of a VM and its

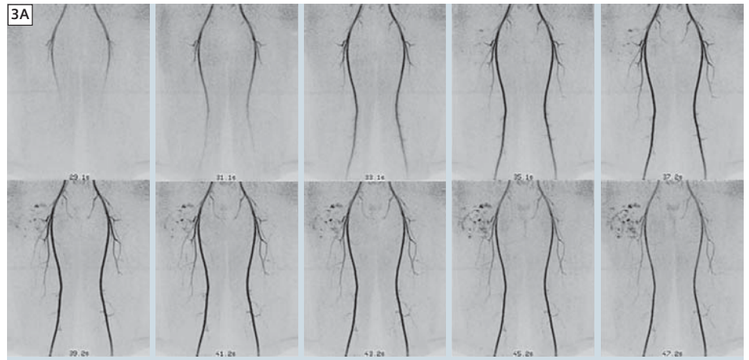

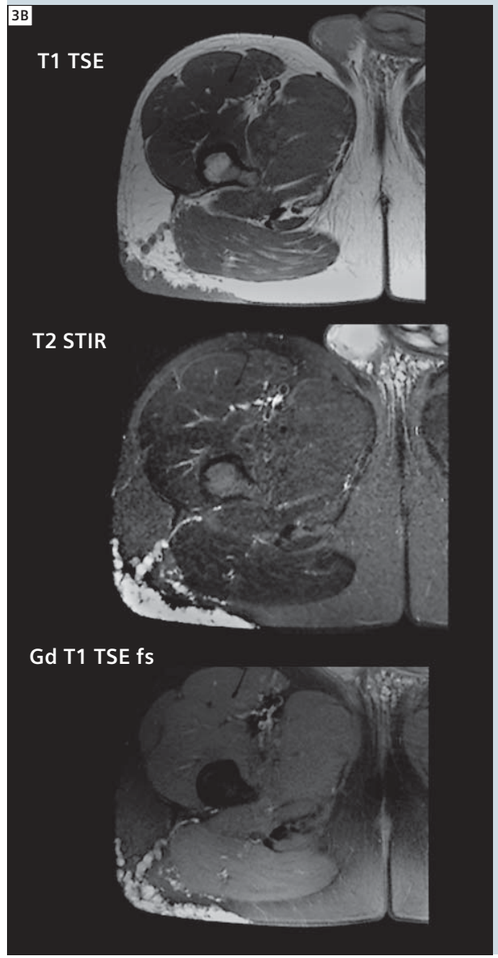

3 Ten consecutive coronal time-resolved inverted MIP images (2.0 s/frame) in a 25-year-old male patient presenting with a vascular malformation of right upper thigh. An early enhancement of dilated vessels in the subcutaneous layer can be seen. **(3B)** Corresponding morphological images in an axial orientation. T1-weighted pre- and post-contrast as well as T2-weighted images show multiple dilated vessels in the subcutaneous tissue. No involvement of the right gluteus maximus muscle was found.

relationship to adjacent critical structures. Moreover, TWIST allows highly sensitive and specific discrimination between high-flow and low-flow malformations. Furthermore, time-resolved MRA can also serve as an objective method to quantitatively assess therapeutic outcomes through serial MRI scans (size of treated lesion, signal characteristics).

Conclusion

Vascular malformations are complex lesions with a variety of clinical manifestations. Time-resolved MRA combined with parallel imaging and echo sharing schemes represents a reasonable alternative to more invasive DSA for the evaluation of VMs. Therefore, time-resolved MRA can play an important role in categorizing these lesions and determining their extent in order to correctly guide treatment.

References

1 Mulliken JB, Glowacki J. Hemangiomas and vascular malformations in infants and children: a classification based on endothelial characteristics. Plast Reconstr Surg 1982; 69:412-422.

2 Meyer JS, Hoffer FA, Barnes PD, et al. Biological classification of soft-tissue vascular anomalies: MR correlation. AJR Am J Roentgenol 1991; 157:559-564.

3 van Rijswijk CS, van der LE, van der Woude HJ, et al. Value of dynamic contrast-enhanced MR imaging in diagnosing and classifying peripheral vascular malformations. AJR Am J Roentgenol 2002; 178:1181-1187.

4 Rinker B, Karp NS, Margiotta M, et al. The role of magnetic resonance imaging in the management of vascular malformations of the trunk and extremities. Plast Reconstr Surg 2003; 112:504-510.

Contact
Ulrich Kramer, M.D.
Diagnostic and Interventional Radiology
University Hospital Tübingen
Hoppe-Seyler-Str. 3
72076 Tübingen
Germany
Ulrich.Kramer@med.uni-tuebingen.de

Common Acronyms

AF	Atrial Fibrillation
B_0	Main (constant) magnetic field
B_1	Radio-frequency magnetic field
CA	Contrast Agent
ce	Contrast Enhanced
CMR	Cardiac / Cardiovascular Magnetic Resonance (Imaging)
CNR	Contrast-to-Noise Ratio
CO	Cardiac Output
CP	Circular Polarization
CTA	Computed Tomography Angiography
DCE	Delayed Contrast Enhancement, syn.: DE
DE	Delayed Enhancement, delayed hyperenhancement
DESS	Dual Echo Steady State
DSA	Digital Subtraction Angiography
EPI	Echo Planar Imaging
EDV	End-diastolic Volume
EF	Ejection Fraction
ESV	End-systolic Volume
FA	Flip Angle
FLASH	Fast-Low-Angle-SHot
FLAIR	Fluid Attenuated Inversion Recovery
fMRI	Functional Magnetic Resonance Imaging
FoV	Field of View
GRAPPA	GeneRalized Autocalibrating Partially Parallel Acquisition (parallel imaging technique)
GRE	GRadient Echo
HASTE	Half-Fourier Acquisition Single-shot TurboSE
HLA	Horizontal Long Axis
iPAT	integrated Parallel Acquisition Technique
IR	Inversion Recovery
LCE	Late Contrast Enhancement, syn.: DE
LE	Late Enhancement, syn.: DE
LGE	Late Gadolinium Enhancement, syn.: DE
LVOT	Left-ventricular Outflow Tract
MEDIC	Multi-Echo Data Image Combination
MION	Monocrystalline Iron Oxide Nanoparticles
MIP	Maximum Intensity Projection
MNP	Magnetic (Iron Oxide) Nanoparticles
MPR	Multiplanar Reconstruction/Reformation
MPRI	Myocaridal Perfusion Reserve Index
MRA	Magnetic Resonance Angiography
NATIVE SPACE	For peripheral MR angiography. Images of arteries and veins without contrast agent (native).
PC	Phase Contrast
PD	Proton Density
PSIR	Phase-Sensitive Inversion Recovery
RF	RadioFrequency
RV	Right ventricle
RVOT	Right-ventricular Outflow Tract
SAR	Specific Absorption Rate
SE	Spin-Echo
SENSE	Sensitivity Encoding
SLT	SLice Thickness, syn.: SL
SNR	Signal-to-Noise Ratio
SR	Saturation Recovery
SSFP	Steady-State-Free-Precession
STIR	Short T1 Inversion Recovery
SV	Stroke Volume
T	Tesla
TA	Acquisition Time
TD	Trigger Delay
TE	Echo time
TEE	Transesophageal Echocardiography
TFL	TurboFLASH
TI	Inversion Time
Tim	Total imaging matrix
TimCT	Tim Continuous Table Move
TIRM	Turbo Inversion Recovery Magnitude
TrueFISP	True Fast Imaging and Steady Precession
TR	Repetition Time
TSE	Turbo Spin-Echo
tSENSE	Time-adaptive SENSitivity Encoding (parallel imaging technique)
TTE	Transthoracic Echocardiography
TTP	Time to Peak
TWIST	Time-resolved angiography With Interleaved Stochastic Trajectories
venc	Velocity Encoding
VIBE	Volume Interpolated Breathhold Examination
VLA	Vertical Long Axis
VRT	Volume Rendering Technique
VSD	Ventricular Septal Defect

4D Flow MR Imaging

Alex Barker; Jelena Bock; Ramona Lorenz; Michael Markl

Department of Radiology, Medical Physics, University Hospital Freiburg, Germany

Introduction

Magnetic Resonance Imaging (MRI) techniques provide non-invasive, highly accurate anatomic depictions of the heart and vessels. The intrinsic motion sensitivity of MRI can be used to image vessels with phase contrast (PC) MR-angiography, or to quantify blood flow [1–3].

Traditionally, MR imaging of flow is accomplished using methods that resolve two spatial dimensions (2D) in individual slices [4]. Alternatively, 3D spatial encoding offers the possibility of isotropic high spatial resolution and thus the ability to measure and visualize the temporal evolution of complex flow patterns in a 3D-volume. In this context, ECG synchronized flow-sensitive 3D MRI using 3-directional velocity encoding (also termed 'flow-sensitive 4D MRI', '4D Flow MRI', 'time-resolved 3D velocity mapping' or '4D PC-MRI') can be employed to detect and visualize global and local blood flow characteristics in targeted vascular regions (aorta, cranial arteries, carotid arteries, etc.) [5, 6].

The nature of such datasets (3 spatial dimensions, 3 blood flow velocity directions, and time) points towards the potential of flow-sensitive 4D MRI to provide detailed quantitative flow and vessel wall parameters with complete vascular coverage. A number of recent studies have indicated the potential of flow-sensitive 4D-MRI for the detailed visualization of complex flow patterns associated with healthy and pathologic hemodynamics [7–12].

Over the past few years, flow-sensitive 4D MR imaging has systematically improved to the point that it is possible to reliably acquire comprehensive flow information within reasonable scan times on routine clinical MR systems. However, the subsequent analysis and visualization of complex, three-directional blood flow within a 3D volume is still time consuming, and advanced data processing and 3D visualization tools are necessary.

In this article we report the first experiences with a new software prototype* for analysis of 4D Flow data, developed by Siemens Healthcare in cooperation with the Medical Physics group at the University Hospital Freiburg, Germany. After a brief overview of MR imaging and data analysis methods, we present their application for the evaluation of flow-sensitive 4D MRI in different vascular territories in the human body.

4D Flow MR Imaging

Modern phase contrast MR imaging allows for the simultaneous acquisition of 3D morphology and time-resolved blood flow velocities in 3 directions. Due to the large amount of data collected, the acquisition timing relies on an efficient synchronization with cardiac and respiratory motion. Image acquisition is therefore based on an ECG-synchronized fast gradient echo sequence with short echo and repetition times in the order of TE = 2–4 ms and TR = 5–7 ms. For thoracic and abdominal applications, additional respiration control using navigator gating is necessary to avoid breathing artifacts. A number of recent methodological improvements (parallel imaging, adaptive respiration control with increased efficiency, etc.) allow for the acquisition of flow-sensitive 4D MRI data with reasonable scan times in the order of 10–20 minutes. Ultimately, the total scan time will depend on the heart rate and efficiency of respiration control in the individual patient. Typical imaging parameters providing full spatial and temporal coverage of different cardiovascular regions of interest are summarized in table 1.

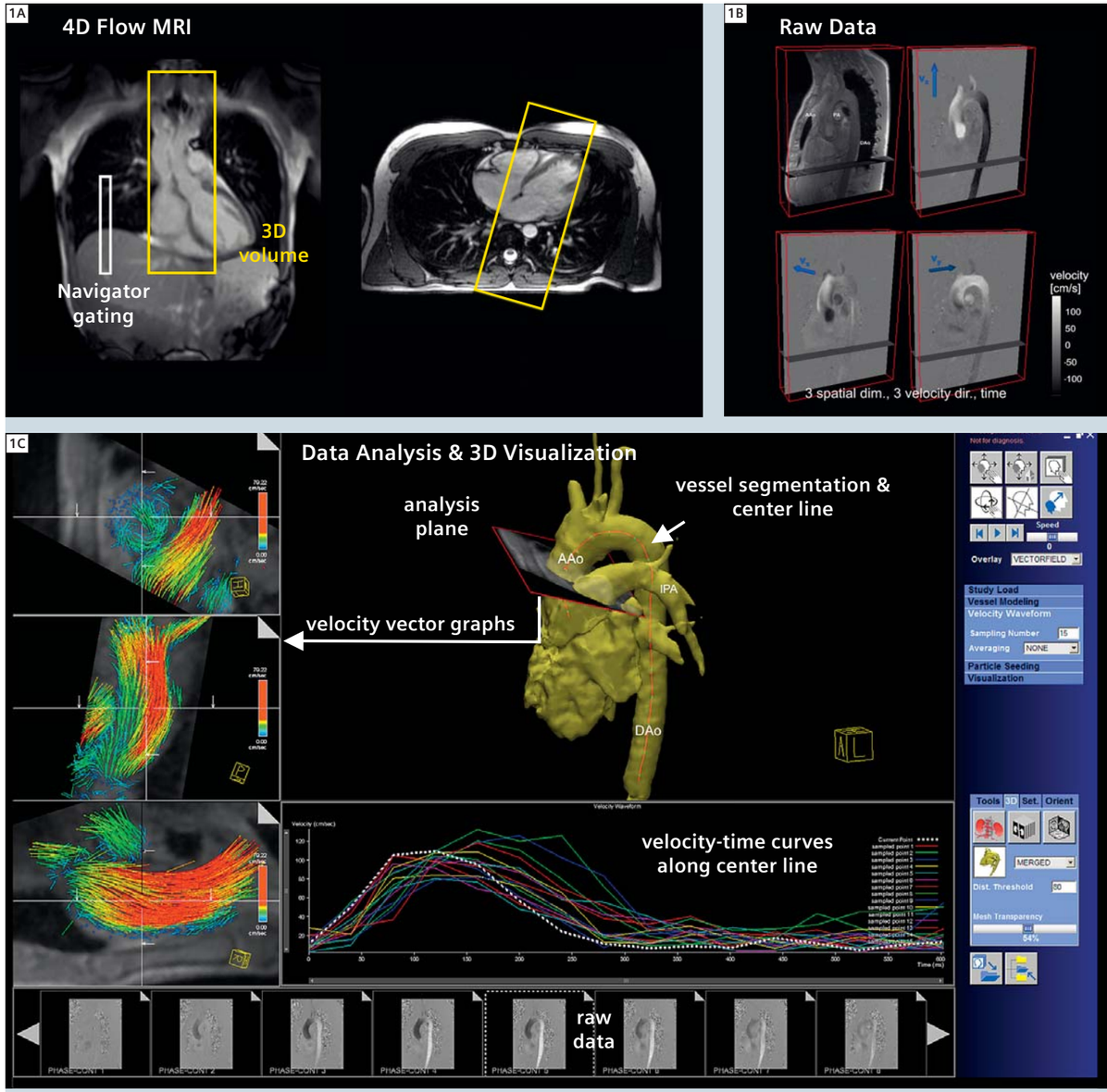

1 Schematic summary of the data acquisition and analysis strategy for flow-sensitive 4D MRI in the thoracic aorta. **A:** For 4D Flow imaging, a sagittal oblique volume covering the entire thoracic aorta is used. Data acquisition is synchronized with the cardiac cycle (ECG gating) and performed during free breathing using adaptive respiration control based on navigator gating of the lung-liver interface. **B:** The 4D Flow raw data, directly after reconstruction consist of the magnitude (top left) and the three sets of velocity encoded phase difference images (v_x, v_y and v_z). These images depict a single sagittal oblique slice at one systolic time point within the acquired 3D volume. Each velocity image represents quantitative velocity components along one encoding direction in which the gray-scale values correspond to the velocity magnitude and direction. **C:** 4D Flow data analysis prototype. 3D flow visualization in the same thoracic aorta is shown in figure 2. AAo: ascending aorta, DAo: descending aorta, lPA: left pulmonary artery.

*Works in Progress. The product is under development and is not commercially available in the U.S. and its future availability cannot be ensured.

Table 1: Typical scan parameters for flow-sensitive 4D MRI in different vascular territories. Velocity sensitivity refers to the maximum blood flow velocity that can be measured without fold-over artifacts (velocity aliasing).

application	spatial resolution	temporal resolution	navigator gating	velocity sensitivity
aorta & pulmonary artery	2.2 mm^3	40 ms	lung-liver interface	100 –150 cm/s
carotid arteries	1.2 mm^3	45 – 50 ms	–	100 cm/s
intracranial arteries	1 mm^3	45 – 50 ms	–	80 cm/s
portal venous system	2.1 mm^3	45 ms	spleen-liver interface	50 cm/s
iliac & femoral arteries	2 mm^3	40 ms	–	80 –100 cm/s

4D Flow analysis and 3D visualization

Flow-sensitive 4D MRI obtains, for each voxel within a 3D-volume and at each measured time point of the cardiac cycle, anatomical and three-directional velocity information. The 4D nature of the data frees the operator from choosing predefined examination planes within the vascular system of interest and offers the opportunity to quantify blood flow at any desired location within the data volume.

The new 4D Flow analysis software was developed to allow for a straightforward and time-efficient analysis of flow characteristics directly following data acquisition. Post-scan, the 4D Flow data can be directly loaded into the software prototype, providing a basic toolbox necessary to produce 3D anatomic and flow visualization. This includes 3D vessel geometry rendering by a combination of thresholding and segmentation, options to semi-automatically or interactively define 2D analysis planes, and automated calculation of vessel center lines. Analysis planes can be manually sized, angulated and used to display regional blood flow velocities as vector fields or to show velocity-time curves along the center line.

Currently implemented features for data analysis and 3D visualization include:

- Direct loading and database storage of 4D Flow raw data.
- Combined vessel lumen thresholding and segmentation to depict 3D vascular geometry/anatomy.
- Interactive 3D data manipulation and 4D (3D + time) viewing.
- Interactive 'point and click' definition of analysis planes and vessel center line calculation.
- Calculation of mean velocity-time curves in analysis planes longitudinally along vessel center line.
- Flow visualization based on time-resolved 3D pathlines originating from multiple and freely selectable emitter planes and locations (including the option to color code according to local absolute blood flow velocity or by vascular origin).
- Planar flow visualization as vector graphs or color coded overlay.

A summary of representative 4D Flow data acquisition and analysis in the thoracic aorta is illustrated in figure 1. The 4D Flow prototype and its different features to display and evaluate raw data, vessel geometry, vessel center line, interactively positioned analysis planes, and velocity-time curves are shown in figure 1C. The 3D flow visualization results, using time-resolved 3D pathlines are depicted in figure 2.

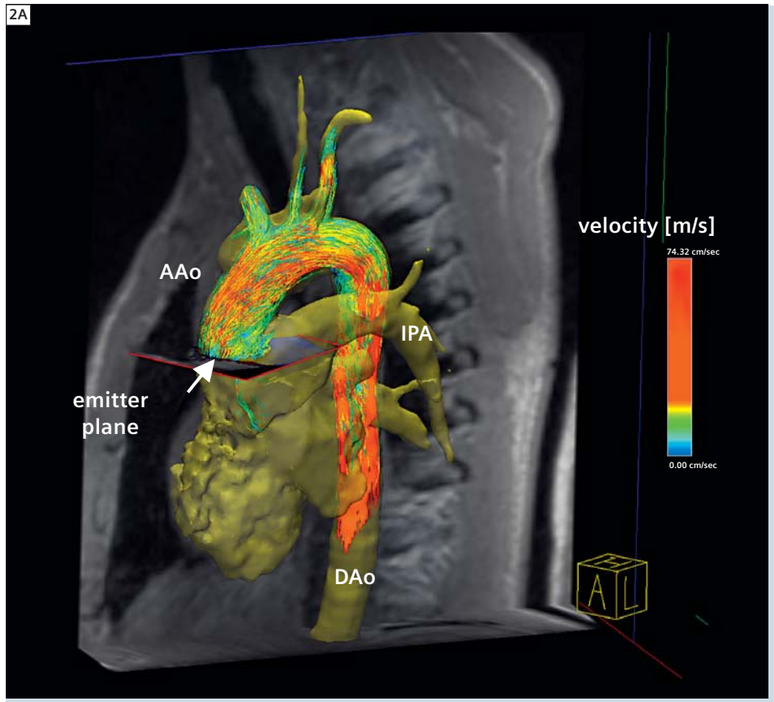

2A Time-resolved 3D pathlines in a normal thoracic aorta during peak systole. **A:** All traces originate from two emitter planes in the ascending aorta and proximal descending aorta (not shown). Color coding reflects the local absolute blood flow velocity.

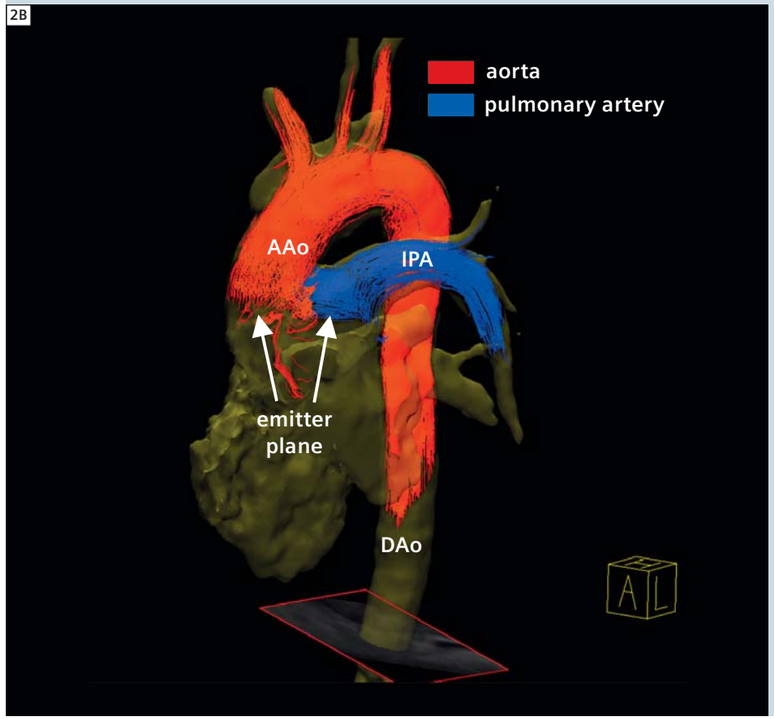

2B **B:** Flow visualization by 3D pathlines in the aorta and pulmonary system. Color coding according to the origin of the traces (red = aorta, blue = pulmonary artery) allows for a clear separation of aortic and pulmonary flow channels which can help understanding complex flow patterns or mixing of flows of different origin. AAo: ascending aorta, DAo: descending aorta, IPA: left pulmonary artery.

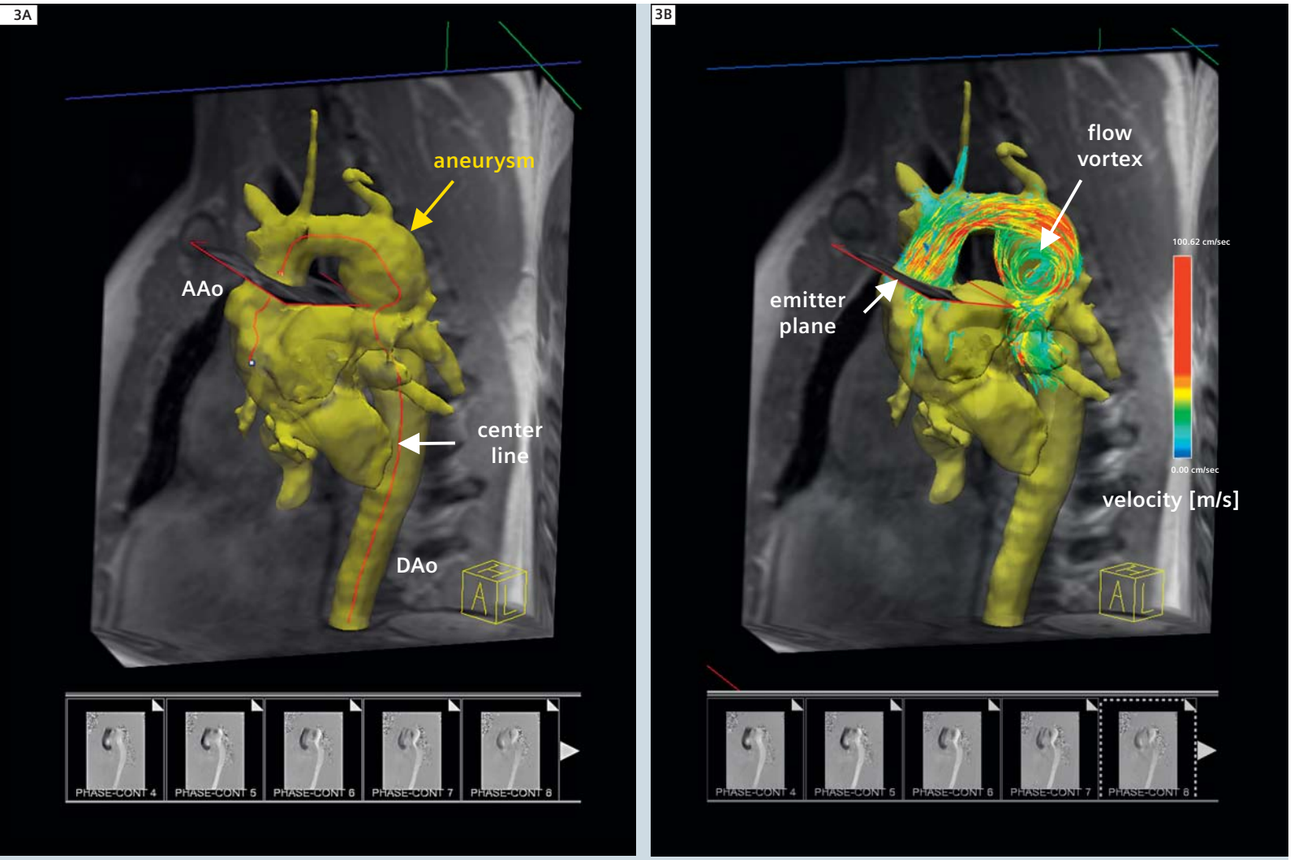

3 3D flow pattern development in the thoracic aorta in a patient with tubular hypoplasia of the aortic arch and an aneurysm of the proximal descending aorta (yellow arrow, diameter = 4.2 cm). 3D pathlines within the segmented aortic lumen clearly illustrate increased flow along the outer aneurysm wall and formation of a pronounced flow vortex within the aneurysm. The possibility to detect flow patterns such as vortex flow or identify regions with increased velocities may help to identify regions with abnormal flow and altered shear forces acting on the vessel wall. It is known from the literature that unfavorable shear forces at the vessel wall can change endothelial function and create areas at risk for vascular remodeling. The identification of such flow patterns may thus help to identify previously not assessable markers for the progression of disease or development of secondary pathologies such as aneurysms or dissections. AAo: ascending aorta, DAo: descending aorta.

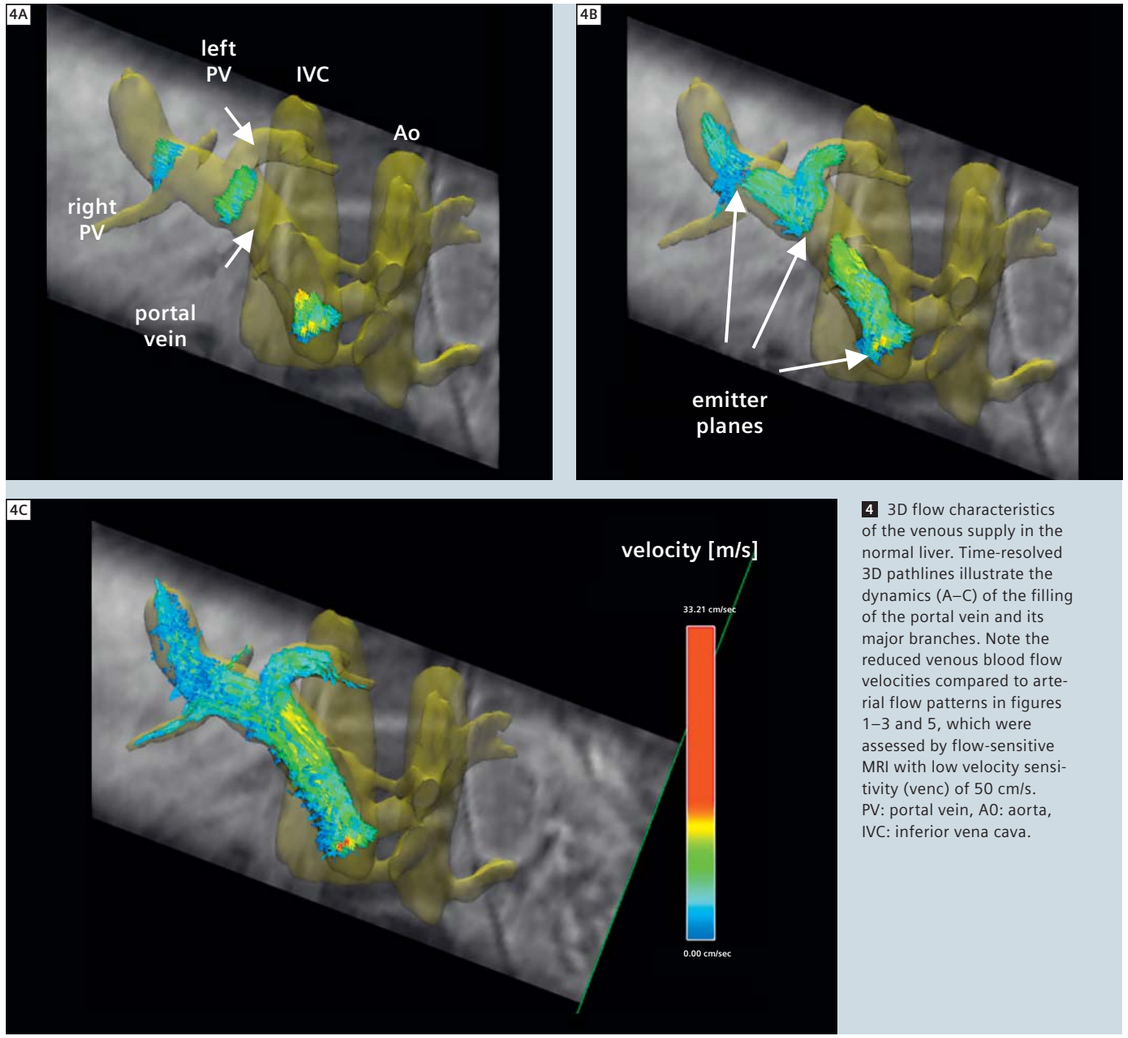

4 3D flow characteristics of the venous supply in the normal liver. Time-resolved 3D pathlines illustrate the dynamics (A–C) of the filling of the portal vein and its major branches. Note the reduced venous blood flow velocities compared to arterial flow patterns in figures 1–3 and 5, which were assessed by flow-sensitive MRI with low velocity sensitivity (venc) of 50 cm/s. PV: portal vein, A0: aorta, IVC: inferior vena cava.

Applications

In the following examples, a number of different vascular territories are presented to illustrate the utility of the new 4D flow analysis software prototype for the comprehensive evaluation of vascular hemodynamics. Figure 3 shows results from the combined visualization of vessel geometry and 3D flow patterns clearly illustrating altered flow patterns and marked vortex flow in a thoracic aortic aneurysm. The dynamics of normal portal venous flow supplying the liver are depicted in figure 4 demonstrating the subsequent filling of the portal vein and its main branches. Figure 5 shows the hemodynamic environment in a carotid bifurcation belonging to a patient with a moderate stenosis of the internal carotid artery. Note that for all patients, the flow sensitive 4D MRI data reflects the true underlying time-resolved blood flow velocity vector field and it is therefore possible to quantify blood flow velocities as shown by the velocity-time curves along the vessel center lines in figures 1 and 5. More details for each case are provided in the legends of figures 3–5.

The current 4D Flow prototype offers a new and time efficient tool to evaluate 4D flow data and has demonstrated its potential for analysis of arterial and venous hemodynamics in different vascular territories. Further improvements of this first software prototype include the implementation of correction algorithms for eddy currents and velocity aliasing as well as improved reporting and presentation functionality. In addition, supplementary refinements regarding flexible quantification of flow parameters (e.g. peak systolic velocities, regurgitant fraction) and derived parameters (e.g. wall shear stress, pressure differences) will enable a comprehensive evaluation of the structural and functional information embedded in 4D flow data.

In summary, the new 4D Flow analysis prototype provides an important first step for the efficient evaluation of vascular hemodynamics – providing a foundation for the adaptation of this technique in the clinical workflow. Further software additions and testing at multiple centers will also provide the opportunity to improve clinical acceptance of flow-sensitive 4D MRI, including the identification of important clinical applications and to streamline future developments.

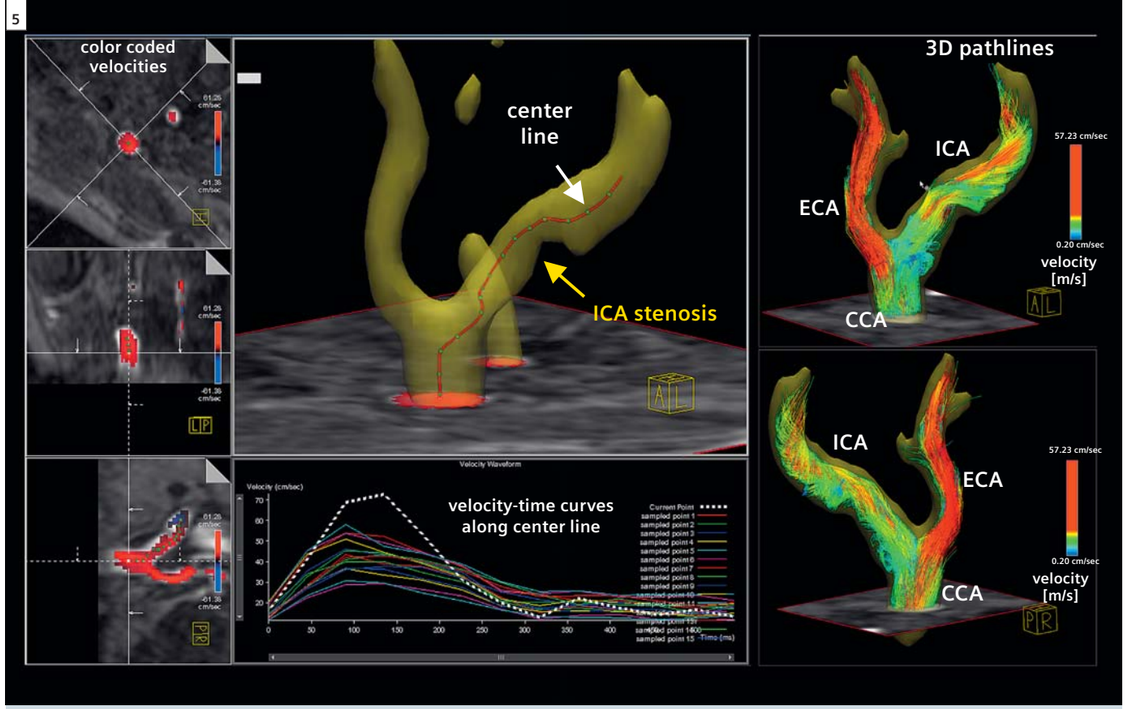

5 Visualization of 3D blood flow characteristics in the carotid bifurcation in a patient with moderate (40%) stenosis of the internal carotid artery (ICA). Thresholding using 3D PC-MR angiography derived form the 4D Flow data and subsequent vessel segmentation allowed for the depiction of the geometry of the carotid bifurcation. The definition of a vessel centerline from the common (CCA) into the internal carotid artery was used to calculate blood flow velocity – time curves in analysis planes along the center line. 3D flow visualization using time-resolved pathlines revealed straight flow through the stenosis and considerably enhanced helix flow within the post-stenotic dilatation. ECA = external carotid artery.

Left to right: Ramona Lorenz, Jelena Bock, Michael Markl, Alex Barker

Contact
PD. Dr. Michael Markl
Department of Radiology, Medical Physics
University Hospital Freiburg, Germany
Phone: +49 761 270 3832
Fax: +49 761 270 3831
michael.markl@uniklinik-freiburg.de

References

1 Firmin DN, Nayler GL, Kilner PJ, Longmore DB. The application of phase shifts in NMR for flow measurement. Magn Reson Med 1990; 14(2):230-241.
2 Dumoulin CL. Phase contrast MR angiography techniques. Magn Reson Imaging Clin N Am 1995;3(3):399-411.
3 Bock J, Frydrychowicz A, Stalder AF, Bley TA, Burkhardt H, Hennig J, Markl M. 4D phase contrast MRI at 3 T: effect of standard and blood-pool contrast agents on SNR, PC-MRA, and blood flow visualization. Magn Reson Med 2010;63(2):330-338.
4 Pelc NJ, Herfkens RJ, Shimakawa A, Enzmann DR. Phase contrast cine magnetic resonance imaging. Magn Reson Q 1991;7(4):229-254.
5 Wigstrom L, Sjoqvist L, Wranne B. Temporally resolved 3D phase-contrast imaging. Magn Reson Med 1996;36(5):800-803.
6 Markl M, Harloff A, Bley TA, Zaitsev M, Jung B, Weigang E, Langer M, Hennig J, Frydrychowicz A. Time-resolved 3D MR velocity mapping at 3T: improved navigator-gated assessment of vascular anatomy and blood flow. J Magn Reson Imaging 2007;25(4):824-831.
7 Frydrychowicz A, Winterer JT, Zaitsev M, Jung B, Hennig J, Langer M, Markl M. Visualization of iliac and proximal femoral artery hemodynamics using time-resolved 3D phase contrast MRI at 3T. J Magn Reson Imaging 2007;25(5):1085-1092.
8 Wetzel S, Meckel S, Frydrychowicz A, Bonati L, Radue EW, Scheffler K, Hennig J, Markl M. In vivo assessment and visualization of intracranial arterial hemodynamics with flow-sensitized 4D MR imaging at 3T. AJNR Am J Neuroradiol 2007;28(3):433-438.
9 Harloff A, Albrecht F, Spreer J, Stalder AF, Bock J, Frydrychowicz A, Schollhorn J, Hetzel A, Schumacher M, Hennig J, Markl M. 3D blood flow characteristics in the carotid artery bifurcation assessed by flow-sensitive 4D MRI at 3T. Magn Reson Med 2009;61(1):65-74.
10 Uribe S, Beerbaum P, Sorensen TS, Rasmusson A, Razavi R, Schaeffter T. Four-dimensional (4D) flow of the whole heart and great vessels using real-time respiratory self-gating. Magn Reson Med 2009;62(4):984-992.
11 Hope MD, Hope TA, Meadows AK, Ordovas KG, Urbania TH, Alley MT, Higgins CB. Bicuspid aortic valve: four-dimensional MR evaluation of ascending aortic systolic flow patterns. Radiology 2010;255(1):53-61.
12 Stankovic Z, Frydrychowicz A, Csatari Z, Panther E, Deibert P, Euringer W, Kreisel W, Russe M, Bauer S, Langer M, Markl M. MR-based visualization and quantification of three-dimensional flow characteristics in the portal venous system. J Magn Reson Imaging 2010;32(2):466-475.

Case Report: Combined Assessment of Haemodynamics and Vessel Architecture in a case of Brain AVM

Jens Fiehler, M.D.

Department of Diagnostic and Interventional Neuroradiology, University Medical Center Hamburg-Eppendorf (UKE), Hamburg, Germany

Patient history

58-year-old male with brain arteriovenous malformation (AVM). Brain imaging was scheduled because of his newly occurring headache probably not related to the AVM.

Sequence details

All images have been acquired using a 3T MAGNETOM Trio and the 8-channel-phased array-head-coil. Along with other sequences, we used a 3D time-resolved echo-shared MR-angiography (TWIST) i.e. 4D-MRA. TWIST was performed using a 3D fast low-angle shot sequence with in-plane image resolution of 2.8 mm x 1.9 mm and slice resolution of 5 mm. Parallel imaging with a GRAPPA (generalized autocalibrating partially parallel acquisitions) factor of 2 applied. Contrast injection was performed by intravenous pump injection of 20 ml contrast agent (MultiHance, Bracco-ALTANA, Konstanz, Germany) at 4 ml/s followed by 20 ml isotonic saline. This technique allowed acquisition of one 3D data set in 0.5 seconds. After TWIST acquisition, a 3D time-of-flight magnetic resonance angiography (TOF-MRA) was obtained with a magnetization transfer saturation pulse, TR 36 ms, TE 6 ms, flip angle 25°, 2 slabs with 32 partitions, image in-plane image resolution of 0.47 mm x 0.47 mm, slice thickness 0.5 mm and a FOV 150 mm x 200 mm.

1 3D maximum intensity projection over time (MIPt).

Imaging findings

Combination of information of haemodynamics based on the voxel-oriented analysis of the temporal intensity curve in TWIST 4D-MRA and anatomical vessel structures in high spatial resolution (TOF-MRA) required the co-registration of both datasets by the home written software tool AnToNIa (Analysis Tool for Neuro Image Data, http://www.uke.de/institute/medizinische-informatik/). A 3D maximum intensity projection over time (MIPt) was created based on the 4D-MRA dataset (Fig. 1). Thereafter, the reso-lution of the 3D MIPt was adapted to the 4D-MRA using a cubic resampling filter. Finally, the transformation field between the two data sets was calculated using an affine 3D-3D registration method with mutual information as similarity measure. Based on the computed transformation field all dynamic characteristics were transferred directly to the TOF-MRA image and color-coded depending on the blood inflow characteristic at the vessel surface (Fig. 2) or in section anatomy (Fig. 3). In an alternative viewing method the inflowing blood can be depicted in a sequential manner (Figure 4 A–D).

Discussion

The short acquisition time allows easy and robust application of TWIST in clinical routine patients. By using the post-processing method as described one can evaluate the complex AVM anatomy from all angles and directions together with inflow information at one time to determine the treatment strategy. The hemodynamic relation of all feeding arteries and draining veins can be assessed in total. In conventional DSA, injections into separate arteries that influence each other are needed, resulting in different series that need to be merged for interpretation. In this particular case we see a temporal AVM that is fed by middle cerebral artery and drained by multiple epicerebral drainage veins. The vein of Trolard is the last draining vein (Fig. 4D). Another advantage of the 4D method is the possibility of view into the AVM Nidus and its intranidal hemodynamics in any required direction. The intranidal flow direction is from lateral to mesial (Fig. 3). The amount of image information is considerable. We needed some time to take advantage of this method. Today we are convinced that it delivers unique information. A TWIST is conducted in all of our AVM patients. We are in the process of further improvement.

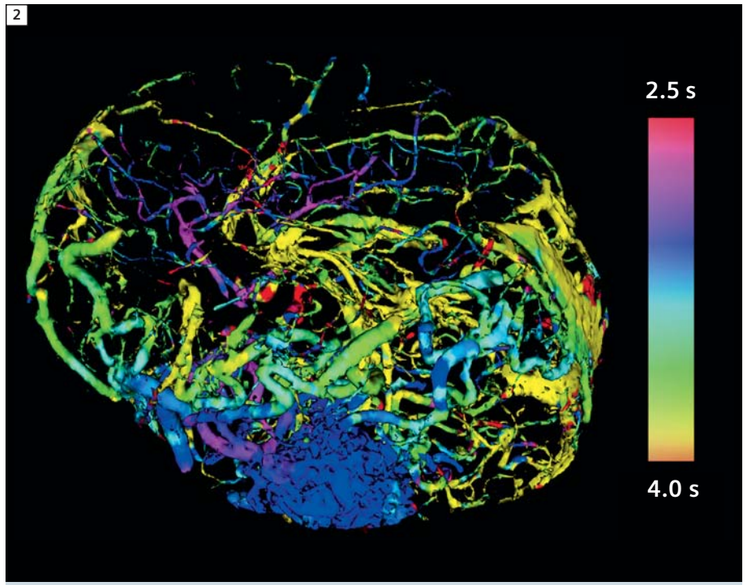

2 MIP projection of the vessels with color-coded information on haemodynamics of the AVM.
3 Transversal reconstruction and overlay of haemodynamic information on TOF MPR.

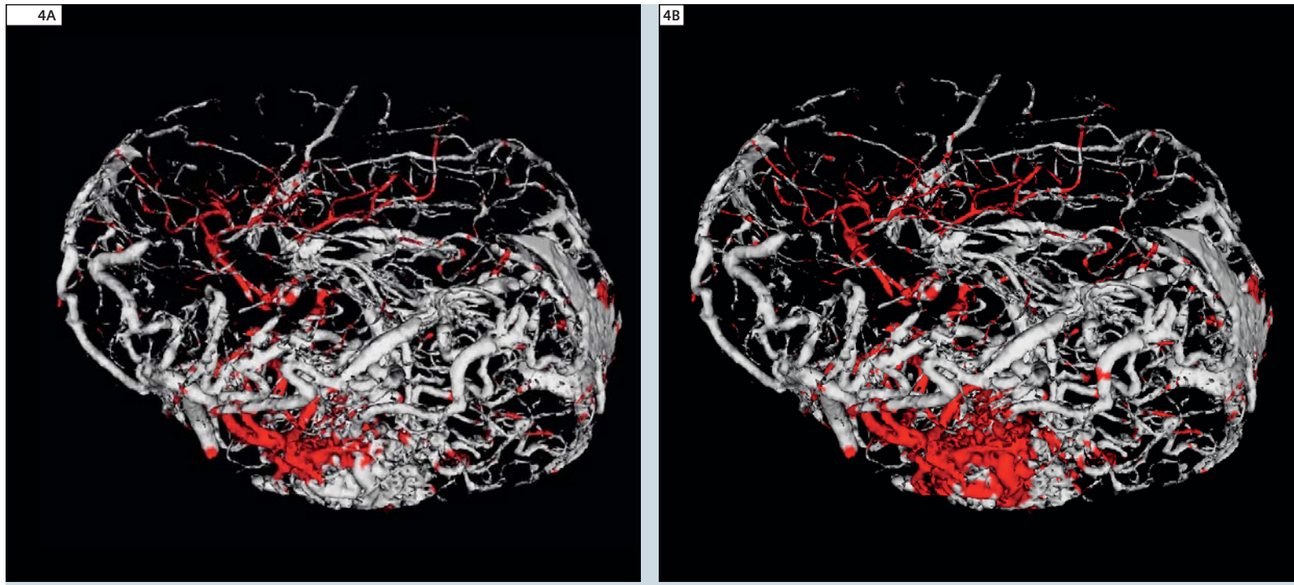

4 Inflowing blood (red color) and its distribution visualized at four different time points (A–D).

Contact
Prof. Jens Fiehler, M.D.
Department of Diagnostic and Interventional Neuroradiology
University Medical Center
Hamburg-Eppendorf (UKE)
Haus Ost 22 (O 22)
Martinistr. 52
20246 Hamburg, Germany
Tel.: +49 40 7410 52746
Fax: +49 40 7410 40114
fiehler@uke.de

Perfusion Imaging and Stroke

Pavlina Polaskova, M.D.[1]; W. Taylor Kimberly, M.D.[2], Ph.D.; A. Gregory Sorensen, M.D.[1], Ona Wu, Ph.D.[1]

[1] *Athinoula A. Martinos Center for Biomedical Imaging, Department of Radiology, Massachusetts General Hospital, Charlestown, MA, USA*
[2] *Massachusetts General Hospital Neuroscience Intensive Care Unit, Harvard Medical School, Charlestown, MA, USA*

Magnetic resonance imaging has become an integral part of patient management and clinical research in stroke. As the majority of stroke patients have an ischemic etiology, assessment of tissue perfusion with perfusion-weighted MR imaging can play a major role in diagnosis, evaluation of therapy, and clinical follow-up.

To date, the only FDA-approved pharmaceutical treatment for acute ischemic stroke is recombinant tissue plasminogen activator (rt-PA) [1]. However, in the US and in other countries only a few percent of patients with acute ischemic stroke are treated by rt-PA, typically because of late arrival to medical care (e.g. they arrive later than the requisite time window of 3 or 4.5 hours) [2, 3]. Hence there remains substantial interest in developing novel stroke therapeutics that could be effective in a wider therapeutic window, or to extend the window for thrombolysis into patient populations with delayed presentation. The recent results of ECASS 3 study demonstrate that thrombolysis can be safely applied as late as 4.5 hours in certain well-characterized patients with a resultant improvement in neurological outcomes [4].

The benefit of thrombolysis appears to gradually diminish over time, which has lead to the maxim "time is brain," and in all cases guidelines suggest treating patients as rapidly as possible. However, it has been proposed that the 3 hour or even the 4.5 hour reperfusion window may be too narrow for certain groups of patients [5–8]. This has gained credence as imaging has revealed that the extent of tissue that eventually undergoes infarction varies substantially among stroke patients, with some patients appearing to have a persistent "ischemic penumbra" that might be salvageable well beyond 3 or 4.5 hours [9–11].

How common is delayed presentation? In the US, the rate of rt-PA administration in acute stroke patients hovers around 5%. Because of the time needed to determine eligibility for thrombolysis, an additional 5% could be candidates for treatment if the window were extended to 6 hours [12]. Strikingly, a further 40% of stroke patients present to the emergency department at time greater than 6 hours but still acutely, suggesting that strategies that could extend treatment even into a small subpopulation could have a significant impact. While there is evidence that a substantial segment of acute stroke patients present later than 6 hours and less than 12, how likely is it that they may benefit from delayed thrombolysis? Accumulating data in the literature combined with our own provide tantalizing evidence that time is much less relevant after 6 hours as compared to before. The heterogeneity of this delayed population however, obscures the potential benefit of thrombolysis that certain subsets might experience. Indeed, ECASS 2 showed that minimally selective strategies applied to patients even less than 6 hours did not result in improved neurological outcome and may have even been harmful. Extending treatment to patients in the 6 to 12 hour category would therefore require careful selection.

Which patients might benefit from delayed treatment? While there are few solid data to answer this question, there are some intriguing clues.

One widely used approach to the identification of salvageable tissue is based on a popular hypothesis: regions of mismatch between diffusion-weighted imaging (DWI) lesions and perfusion-weighted imaging (PWI) lesions found on early stroke imaging, that sometimes go on to infarction, but sometimes do not, represent tissue that has an increased likelihood of salvageability. The basis for this thinking is that since brain parenchyma can undergo a period of hypoperfusion without developing permanent parenchymal injury, perhaps this mismatch region is salvageable. This mismatch region is sometimes therefore called an imaging correlate of the ischemic penumbra. The DWI lesion is thought to represent irreversibly damaged area, termed by some investigators to be representative of the ischemic core. This hypothesis has been tested in the DEFUSE study, a prospective study of 74 patients receiving rt-PA therapy between 3 to 6 hours after symptom onset [13]. Patients with a mismatch had significantly increased odds of favorable clinical outcome if reperfusion was attained, whereas no beneficial effect with reperfusion was observed in patients without. These findings support the idea that the mismatch is a useful concept; other single-center retrospective studies based on both CT and MRI mismatches further support the mismatch hypothesis [14–16]. Remarkably, we have found that as many as 40% of our patients in the 6 to 12 hour time frame still have a persistent penumbra defined by DWI/PWI mismatch. Recent analysis reveals that perfusion imaging used to guide delayed IV thrombolysis is associated with

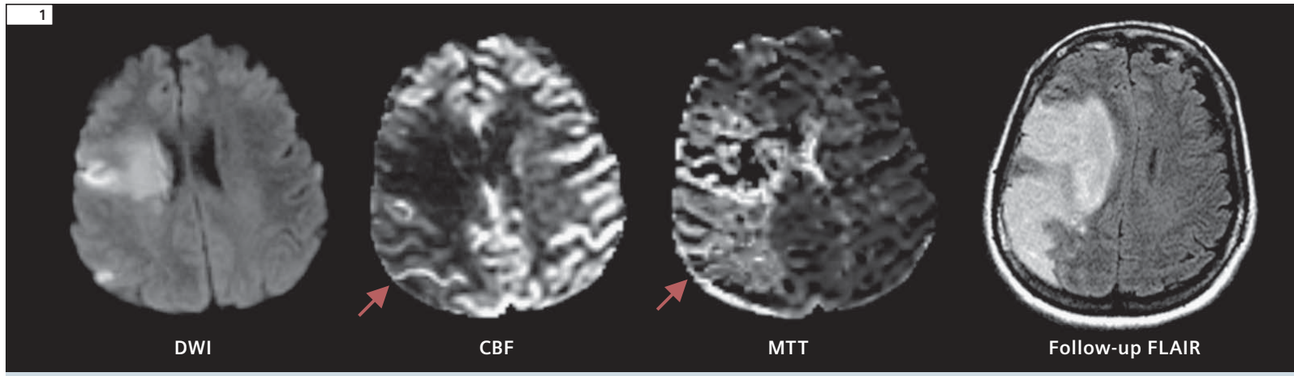

1 Persistent penumbra in 52-year-old male 11 hours post onset of symptoms. Mismatch (red arrows) proceeds to infarction on follow-up FLAIR at 6 days. *Figures reprinted with permission from MRM 50:856-864 (2003).*

increased reperfusion [17]. Interventional approaches have recently demonstrated that good neurological outcomes can be achieved even when revascularization occurs later than 8 hours [18]. Experience in the MERCI/multiMERCI cohort suggests that the time to reperfusion is not adversely associated with outcomes in these delayed patients and that good neurological outcomes are nearly as common early as they are late (~ 40%). Put another way, patients who were reperfused later than 7 hours from the ictus had similar rates of good outcome compared to those with earlier reperfusion [19]. Nevertheless, just over half of these patients did not experience a good outcome and may have been unnecessarily exposed to the risks of the intervention. Similarly, extending thrombolysis into such a delayed population may carry increased risk of hemorrhage. This further emphasizes the importance of characterizing and distinguishing patients who may benefit from delayed treatment from those who would not.

At least two recent trials have investigated the outcome of reperfusion therapy based on PWI/DWI mismatch: EPITHET [20] barely missed its prospectively defined primary endpoint, which was to demonstrate whether patients exhibiting mismatch responded better to late rt-PA therapy than those that did not; DIAS II [21] failed to demonstrate that patients selected using neuroimaging can benefit from reperfusion therapy up to 9 h. While there were methodological issues with both of these trials – particularly with perfusion imaging, which we believe needs to be improved and made less sensitive to delay artifacts – it seems likely that more than DWI/PWI will be needed. While the diffusion abnormality is almost always associated with later infarction, even this is not always the case [22].

Still, the late presence of the DWI/PWI mismatch remains intriguing. We have identified that this mismatch can be highly persistent, lasting for many hours [23], particularly in patients with proximal artery occlusions [24]. But the high variability in tissue and clinical outcome of the treatment based on the mismatch suggests at least two major areas of further research:

- methodological differences in the definition and measurement of the mismatch;
- biological factors playing a role in tissue salvageability.

While the mismatch could be a sign that there is still viable tissue even at late time points – something that PET also has suggested [25, 26] – it also could mean that PWI-based method is unreliable and is actually not useful. Some investigators have suggested that the so-called mismatch might in reality be due to technical limitations that have previously overestimated the size of the penumbra. This leads to the question: Could the persistent penumbra simply be an artifact?

Currently, the measurement of tissue perfusion is based on serial imaging of the concentration of exogenous contrast agent, such as gadolinium-DTPA or endogenous agent, such as magnetically labeled blood [27]. The most common technique is contrast-enhanced dynamic susceptibility (T2*-weighted) technique (DSC), which employs the measurable decrease of signal intensity, as it is seen on a series of rapid images obtained when a bolus of IV contrast agent passes through the brain. This signal intensity decrease can be converted to a concentration-time curve, from which the hemodynamic parameters are then calculated. Cerebral blood flow (CBF), cerebral blood volume (CBV) and mean transit time (MTT), are estimated by deconvolving the change in tissue concentration over the first pass of a bolus of contrast agent with an arterial input function (AIF) using standard singular value decomposition (sSVD) [28]. However, flow estimates using sSVD have been shown to be sensitive to tracer arrival delay (such as might occur with carotid stenosis that caused a delay in tracer arrival but not a decrease in flow), and dispersion between the selected AIF and

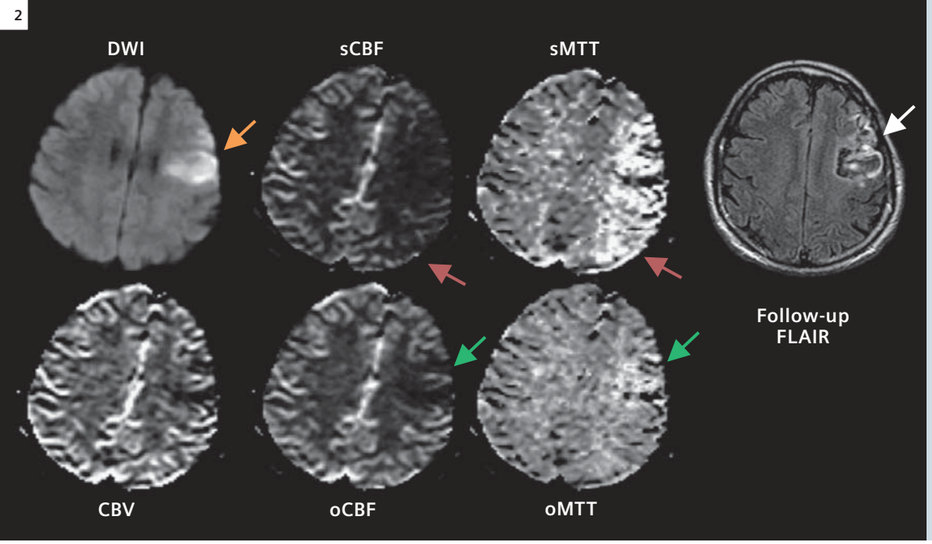

2 Artifactual mismatch due to delay-sensitive CBF calculation in a 62-year-old male imaged 7 h after symptom onset. The diffusion lesion (orange arrow) is similar to the 4 month follow-up FLAIR lesion (white arrow). The standard CBF and MTT maps (sCBF, sMTT) show a large mismatch (red arrows); this mismatch disappears when circular deconvolution methods are used (oCBF, oMTT, green arrows). Therefore the correct assessment is that there is no DWI/PWI mismatch in this patient when PWI is correctly computed. *Figures reprinted with permission from MRM 50:164-174 (2003).*

tissue signals [29–32]. This results to a significant underestimation of CBF and therefore, greater mismatch.

We developed a method to compensate this, called circular deconvolution (oSVD), that uses a block-circulant matrix for deconvolution to reduce sensitivity to tracer arrival differences between chosen AIF and tissue signal. Adding the delay parameter to the method (reflecting the disturbed hemodynamics) provides more accurate estimates of CBF and MTT than standard sSVD. Importantly, the oSVD technique gives results comparable to those of sSVD when there are no differences between the tracer arrival time of the AIF and the tissue signal [32, 33].

Another cause of variability is using "global" arterial input function. It is typically selected manually by a trained specialist as the average of a small number of concentration-time curves from voxels immediately adjacent to a major artery in the contralateral hemisphere and then deconvolved from the concentration-time curves for every voxel of the brain. But, if used on a tissue that has delayed and/or dispersed concentration-time curves, this leads again to an underestimation of the blood flow, thus adding another possible source of misinterpretation.

In theory, both delay and dispersion can be overcome by using the so-called "local AIF" method. In this method, an arterial input function (AIF) is defined for each voxel based on the voxels in the local nearby region of tissue. Moreover, this method is fully automated, because the local AIFs can be selected as a part of a predefined algorithm. First results appear promising, though full validation remains to be carried out. As patients with stroke are likely to have delay and/or dispersion, further improvements in delay and dispersion correction methods remain the aim of ongoing research [34].

We note that even with this improved blood flow calculation methodology, more metabolic information may well be needed to understand the concept of persistent penumbra and to truly identify salvageable tissue. We and other groups have already developed models that incorporated other biological variables, such as stroke location, age and stroke subtype [35–37]. These methods take multiple input parameters and allow the system to create "risk maps" that can be used to describe the probability of infarction of each single voxel of tissue, based on acute imaging. Other metabolic-focused approaches, currently being studied in our laboratory and other laboratories, include:

- brief patient exposure to oxygen, and measurement of the tissue response (by, for example, quantitative BOLD imaging);
- use of pH-weighted MR imaging, and correlating these findings with follow-up tissue outcome,
- measuring levels of lactate in both infarcted tissue and penumbra (using an adiabatic high-resolution spiral CSI sequence) to determine their geographical difference and relation to the tissue viability.

Conclusion

Stroke remains a major public health problem throughout the world, and MRI has already contributed substantially to its management. Further efforts are needed to improve perfusion imaging and beyond in order to optimally reduce morbidity and mortality.

References

1 Tissue plasminogen activator for acute ischemic stroke. The National Institute of Neurological Disorders and Stroke rt-PA Stroke Study Group. *N Engl J Med.* 1995;333:1581-1587.
2 Goldstein LB. Acute ischemic stroke treatment in 2007. *Circulation.* 2007;116:1504-1514.
3 Katzan IL, Hammer MD, Hixson ED, Furlan AJ, Abou-Chebl A, Nadzam DM. Utilization of intravenous tissue plasminogen activator for acute ischemic stroke. *Arch Neurol.* 2004;61:346-350.
4 Hacke W, Kaste M, Bluhmki E, Brozman M, Davalos A, Guidetti D, Larrue V, Lees KR, Medeghri Z, Machnig T, Schneider D, von Kummer R, Wahlgren N, Toni D. Thrombolysis with alteplase 3 to 4.5 hours after acute ischemic stroke. *N Engl J Med.* 2008;359:1317-1329.
5 Ringleb PA, Schellinger PD, Schranz C, Hacke W. Thrombolytic therapy within 3 to 6 hours after onset of ischemic stroke: useful or harmful? *Stroke.* 2002;33:1437-1441.
6 Hacke W, Donnan G, Fieschi C, Kaste M, von Kummer R, Broderick JP, Brott T, Frankel M, Grotta JC, Haley EC, Jr., Kwiatkowski T, Levine SR, Lewandowski C, Lu M, Lyden P, Marler JR, Patel S, Tilley BC, Albers G, Bluhmki E, Wilhelm M, Hamilton S. Association of outcome with early stroke treatment: pooled analysis of ATLANTIS, ECASS, and NINDS rt-PA stroke trials. *Lancet.* 2004;363:768-774.

7 Kent DM, Ruthazer R, Selker HP. Are some patients likely to benefit from recombinant tissue-type plasminogen activator for acute ischemic stroke even beyond 3 hours from symptom onset? *Stroke.* 2003;34:464-467.
8 Kent DM, Selker HP, Ruthazer R, Bluhmki E, Hacke W. Can multivariable risk-benefit profiling be used to select treatment-favorable patients for thrombolysis in stroke in the 3- to 6-hour time window? *Stroke.* 2006;37:2963-2969.
9 Schaefer PW, Ozsunar Y, He J, Hamberg LM, Hunter GJ, Sorensen AG, Koroshetz WJ, Gonzalez RG. Assessing tissue viability with MR diffusion and perfusion imaging. *AJNR Am J Neuroradiol.* 2003;24:436-443.
10 Sorensen AG, Buonanno FS, Gonzalez RG, Schwamm LH, Lev MH, Huang-Hellinger FR, Reese TG, Weisskoff RM, Davis TL, Suwanwela N, Can U, Moreira JA, Copen WA, Look RB, Finklestein SP, Rosen BR, Koroshetz WJ. Hyperacute stroke: evaluation with combined multisection diffusion-weighted and hemodynamically weighted echo-planar MR imaging. *Radiology.* 1996;199:391-401.
11 Sorensen AG, Copen WA, Ostergaard L, Buonanno FS, Gonzalez RG, Rordorf G, Rosen BR, Schwamm LH, Weisskoff RM, Koroshetz WJ. Hyperacute stroke: simultaneous measurement of relative cerebral blood volume, relative cerebral blood flow, and mean tissue transit time. *Radiology.* 1999;210:519-527.
12 Prioritizing interventions to improve rates of thrombolysis for ischemic stroke. *Neurology.* 2005;64:654-659.
13 Albers GW, Thijs VN, Wechsler L, Kemp S, Schlaug G, Skalabrin E, Bammer R, Kakuda W, Lansberg MG, Shuaib A, Coplin W, Hamilton S, Moseley M, Marks MP. Magnetic resonance imaging profiles predict clinical response to early reperfusion: the diffusion and perfusion imaging evaluation for understanding stroke evolution (DEFUSE) study. *Ann Neurol.* 2006;60:508-517.
14 Jansen O, Schellinger P, Fiebach J, Hacke W, Sartor K. Early recanalisation in acute ischaemic stroke saves tissue at risk defined by MRI. *Lancet.* 1999;353:2036-2037
15 Lev MH, Segal AZ, Farkas J, Hossain ST, Putman C, Hunter GJ, Budzik R, Harris GJ, Buonanno FS, Ezzeddine MA, Chang Y, Koroshetz WJ, Gonzalez RG, Schwamm LH. Utility of perfusion-weighted CT imaging in acute middle cerebral artery stroke treated with intra-arterial thrombolysis: prediction of final infarct volume and clinical outcome. *Stroke.* 2001;32:2021-2028.
16 Parsons MW, Barber PA, Chalk J, Darby DG, Rose S, Desmond PM, Gerraty RP, Tress BM, Wright PM, Donnan GA, Davis SM. Diffusion- and perfusion-weighted MRI response to thrombolysis in stroke. *Ann Neurol.* 2002;51:28-37
17 Mishra NK, Albers GW, Davis SM, Donnan GA, Furlan AJ, Hacke W, Lees KR. Mismatch-based delayed thrombolysis: a meta-analysis. *Stroke.* 2010;41:e25-33.
18 Natarajan SK, Snyder KV, Siddiqui AH, Ionita CC, Hopkins LN, Levy EI. Safety and effectiveness of endovascular therapy after 8 hours of acute ischemic stroke onset and wake-up strokes. *Stroke.* 2009;40:3269-3274.
19 Nogueira RG, Liebeskind DS, Sung G, Duckwiler G, Smith WS. Predictors of good clinical outcomes, mortality, and successful revascularization in patients with acute ischemic stroke undergoing thrombectomy: pooled analysis of the Mechanical Embolus Removal in Cerebral Ischemia (MERCI) and Multi MERCI Trials. *Stroke.* 2009;40:3777-3783.
20 Davis SM, Donnan GA, Parsons MW, Levi C, Butcher KS, Peeters A, Barber PA, Bladin C, De Silva DA, Byrnes G, Chalk JB, Fink JN, Kimber TE, Schultz D, Hand PJ, Frayne J, Hankey G, Muir K, Gerraty R, Tress BM, Desmond PM. Effects of alteplase beyond 3 h after stroke in the Echoplanar Imaging Thrombolytic Evaluation Trial (EPITHET): a placebo-controlled randomised trial. *Lancet Neurol.* 2008;7:299-309.
21 Hacke W, Furlan AJ, Al-Rawi Y, Davalos A, Fiebach JB, Gruber F, Kaste M, Lipka LJ, Pedraza S, Ringleb PA, Rowley HA, Schneider D, Schwamm LH, Leal JS, Sohngen M, Teal PA, Wilhelm-Ogunbiyi K, Wintermark M, Warach S. Intravenous desmoteplase in patients with acute ischaemic stroke selected by MRI perfusion-diffusion weighted imaging or perfusion CT (DIAS-2): a prospective, randomised, double-blind, placebo-controlled study. *Lancet Neurol.* 2009;8:141-150.
22 Kidwell CS, Saver JL, Mattiello J, Starkman S, Vinuela F, Duckwiler G, Gobin YP, Jahan R, Vespa P, Villablanca JP, Liebeskind DS, Woods RP, Alger JR. Diffusion-perfusion MRI characterization of post-recanalization hyperperfusion in humans. *Neurology.* 2001;57:2015-2021.
23 Gonzalez RG, Hakimelahi R, Schaefer PW, Roccatagliata L, Sorensen AG, Singhal AB. Stability of large diffusion/perfusion mismatch in anterior circulation strokes for 4 or more hours. *BMC Neurol.* 2010;10:13.
24 Copen WA, Rezai Gharai L, Barak ER, Schwamm LH, Wu O, Kamalian S, Gonzalez RG, Schaefer PW. Existence of the diffusion-perfusion mismatch within 24 hours after onset of acute stroke: dependence on proximal arterial occlusion. *Radiology.* 2009;250:878-886.
25 Marchal G, Beaudouin V, Rioux P, de la Sayette V, Le Doze F, Viader F, Derlon JM, Baron JC. Prolonged persistence of substantial volumes of potentially viable brain tissue after stroke: a correlative PET-CT study with voxel-based data analysis. *Stroke.* 1996;27:599-606.
26 Baron JC, Moseley ME. For how long is brain tissue salvageable? Imaging-based evidence. *J Stroke Cerebrovasc Dis.* 2000;9:15-20.
27 Rosen BR, Belliveau JW, Vevea JM, Brady TJ. Perfusion imaging with NMR contrast agents. *Magn Reson Med.* 1990;14:249-265.
28 Ostergaard L, Weisskoff RM, Chesler DA, Gyldensted C, Rosen BR. High resolution measurement of cerebral blood flow using intravascular tracer bolus passages. Part I: Mathematical approach and statistical analysis. *Magn Reson Med.* 1996;36:715-725
29 Ostergaard L, Chesler DA, Weisskoff RM, Sorensen AG, Rosen BR. Modeling cerebral blood flow and flow heterogeneity from magnetic resonance residue data. *J Cereb Blood Flow Metab.* 1999;19:690-699.
30 Calamante F, Gadian DG, Connelly A. Delay and dispersion effects in dynamic susceptibility contrast MRI: simulations using singular value decomposition. *Magn Reson Med.* 2000;44:466-473.
31 Calamante F, Gadian DG, Connelly A. Quantification of perfusion using bolus tracking magnetic resonance imaging in stroke: assumptions, limitations, and potential implications for clinical use. *Stroke.* 2002;33:1146-1151.
32 Wu O, Ostergaard L, Koroshetz WJ, Schwamm LH, O'Donnell J, Schaefer PW, Rosen BR, Weisskoff RM, Sorensen AG. Effects of tracer arrival time on flow estimates in MR perfusion-weighted imaging. *Magn Reson Med.* 2003;50:856-864.
33 Wu O, Ostergaard L, Weisskoff RM, Benner T, Rosen BR, Sorensen AG. Tracer arrival timing-insensitive technique for estimating flow in MR perfusion-weighted imaging using singular value decomposition with a block-circulant deconvolution matrix. *Magn Reson Med.* 2003;50:164-174.
34 Lorenz C, Benner T, Chen PJ, Lopez CJ, Ay H, Zhu MW, Menezes NM, Aronen H, Karonen J, Liu Y, Nuutinen J, Sorensen AG. Automated perfusion-weighted MRI using localized arterial input functions. *J Magn Reson Imaging.* 2006;24:1133-1139.
35 Ay H, Benner T, Arsava EM, Furie KL, Singhal AB, Jensen MB, Ayata C, Towfighi A, Smith EE, Chong JY, Koroshetz WJ, Sorensen AG. A computerized algorithm for etiologic classification of ischemic stroke: the Causative Classification of Stroke System. *Stroke.* 2007;38:2979-2984.
36 Ay H, Koroshetz WJ, Vangel M, Benner T, Melinosky C, Zhu M, Menezes N, Lopez CJ, Sorensen AG. Conversion of ischemic brain tissue into infarction increases with age. *Stroke.* 2005;36:2632-2636.
37 Menezes NM, Ay H, Wang Zhu M, Lopez CJ, Singhal AB, Karonen JO, Aronen HJ, Liu Y, Nuutinen J, Koroshetz WJ, Sorensen AG. The real estate factor: quantifying the impact of infarct location on stroke severity. *Stroke.* 2007;38:194-197.
38 Wu O, Ostergaard L, Weisskoff RM, Benner T, Rosen BR, Sorensen AG. Tracer arrival timing-insensitive technique for estimating flow in MR perfusion-weighted imaging using singular value decomposition with a block-circulant deconvolution matrix. Magn Reson Med. 2003;50(1):164-74.

Contact
Ona Wu, PhD
Athinoula A. Martinos Center
for Biomedical Imaging
149 Thirteenth Street, Suite 2301
Charlestown, Massachusetts 02129
USA
Phone: +1617 643 3873
Fax: +1617 643 3939
ona@nmr.mgh.harvard.edu

Functional Prostate MR Including Dynamic Contrast-Enhanced T1-Weighted Imaging at 1.5 Tesla Without Endorectal Coil.

First Clinical Experiences with a Study Protocol at Multi-Imagem, Brazil

Leonardo Kayat Bittencourt, M.D.; Thomas Doring, MSc; Marcio Bernardes, RT; Emerson Gasparetto, M.D., Ph.D.; Romeu Cortês Domingues, M.D.

CDPI Clínica de Diagnóstico Por Imagem, Multi-Imagem, UFRJ - Federal University of Rio de Janeiro, Rio de Janeiro, Brazil

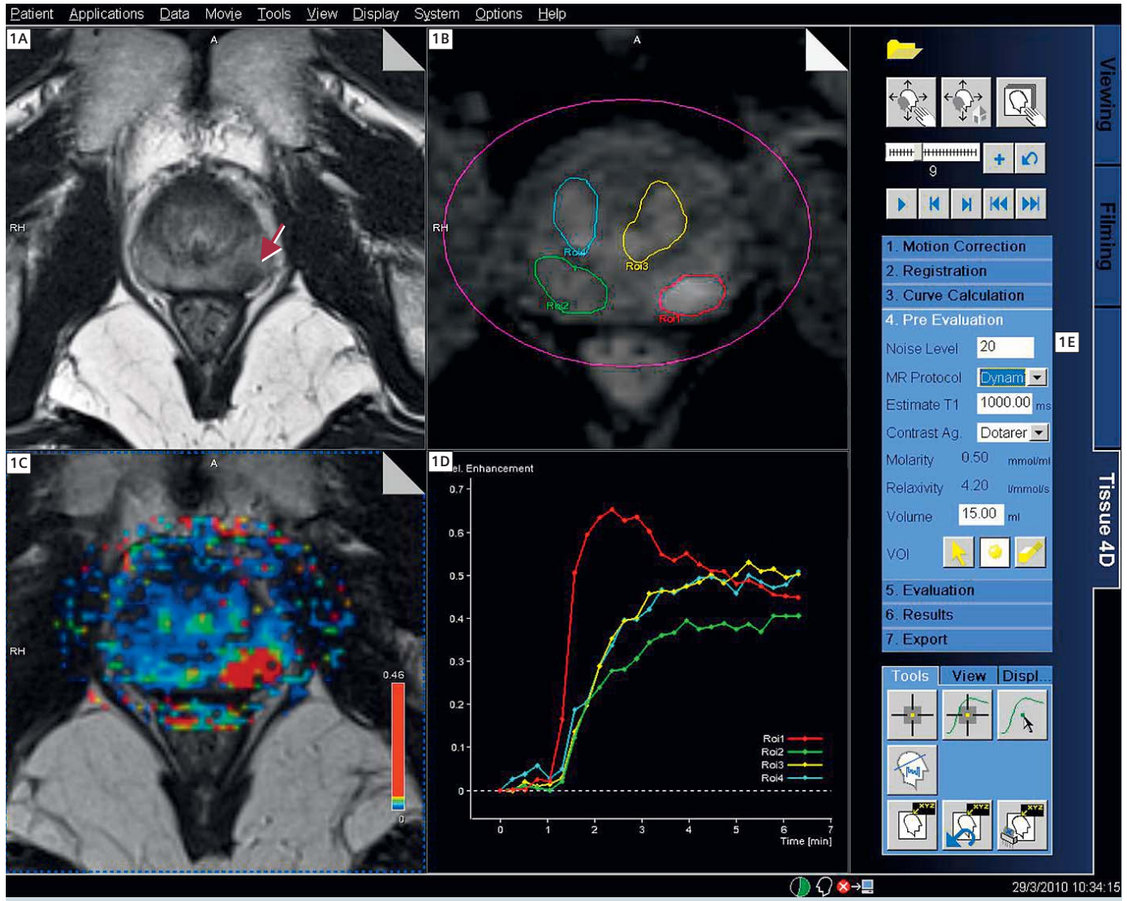

1 *syngo* Tissue 4D screen capture, depicting its four panels, with anatomical (T1w or T2w) images in **1A**, (subtracted) image of dynamic data set in **1B**, parametric maps (K_{trans}, Kep, Ve, iAUC) overlaid on anatomy in **1C**, and relative enhancement curves in **1D**. Note that the suspicious T2w hypointense area in **1A** (arrowhead) corresponds to the red ROI in **1B**, the focally increased K_{trans} area in **1C** and early/intense enhancing curve with washout in **1D**.

Introduction

Reviewing the current literature on prostate MR, most authors rely on the use of 3T scanners that reveal better diagnostic and staging accuracy than the previous studies using older 1.5T and 1.0T machines in the 90's. However, in most countries 1.5T MR scanners are still more widely available than 3T machines. Looking at new developments in coil technology this new generation of 1.5 Tesla superconducting MR scanners potentially provides an acceptable performance on the management of prostate cancer (PCa) patients. Moreover, the continuing improvement of functional sequences, namely diffusion-weighted imaging (DWI) and dynamic contrast enhancement (DCE) T1w imaging and the development of new post-processing tools (i.e., image-fusion and pharmacokinetic maps) could further contribute on the diagnostic and staging accuracy of MRI including 1.5T MR scanners. Based on the literature, multi-modal imaging of the prostate at 1.5 Tesla includes the usage of an endorectal coil. However, in clinical routine the application of such a coil can be restricted by various reasons such as proctitis. However, it should also be taken into account that the procedure of placing an endorectal coil can result in low acceptance of the exam and potentially reduces patient compliance significantly. Therefore it is of high clinical interest to better understand the potential but also the limitations of prostate MRI at 1.5 Tesla without application of an endorectal coil. In this article, we describe in detail our prostate MR protocol and post-processing parameters at 1.5 Tesla without endorectal coil with special focus on DCE T1w imaging, and briefly present the preliminary results, with illustrative cases.

Table 1

Feature	Prostate MR	Histopathology
Unilateral Involvement	3	2
Bilateral Involvement	10	11
Extra-prostatic extension	3	4
Seminal Vesicle extension	1	1
Positive Lymph Nodes	0	0

Materials and methods

This protocol was developed in 2009, as part of an ongoing long-term prostate MR research project. The study was approved by the local Ethics and Research Committee, and all patients signed an informed consent.
Thirteen consecutive patients were submitted to prostate MR examinations, prior to prostatectomy. Patients' age ranged between 51 and 77 years (average 63 years), their PSA levels varying between 3.4 and 42.0 ng/mL (median 8.6 ng/mL). Examinations (table 1) were done on an 18-channel 1.5T scanner (MAGNETOM Avanto, Siemens Healthcare, Erlangen, Germany), with a combination of the 6-channel phased-array surface coil (Body Matrix) combined with up to 6 elements of the integrated spine coil. Prior to the examinations, the patients were given 10 mg of n-methil-scopolamine bromide (Buscopan®, Boehringer Ingelheim, Brazil), in order to attenuate peristalsis. The study protocol consisted of high-resolution T2-weighted turbo spin echo (TSE) sequences in the axial (TR 4750 ms, TE 101 ms, no PAT, FOV (160 x 160) mm^2, matrix (256 x 230) px^2, slice thickness 3 mm, no gap, 3 averages, acquisition time 5:47 min), coronal (TR 3000 ms, TE 101 ms, no PAT, FOV (160 x 160) mm^2, matrix (256 x 230) px^2, slice thickness 3.5 mm, 20% gap, 2 averages, acquisition time 2:15 min) and sagittal (TR 3800 ms, TE 100 ms, no PAT, FOV (170 x 170) mm^2, matrix (320 x 240) px^2, slice thickness 3 mm, 10% gap, 2 averages, acquisition time 3:21 min) planes, high-resolution axial dark fluid T1-weighted sequence (TIRM; TR 2100 ms, TE 20 ms, TI 829.7 ms, PAT factor 2 (*syngo* GRAPPA), FOV (200 x 180) mm^2, matrix (256 x 200) px^2, slice thickness 3 mm, 10% gap, 2 averages, acquisition time 3:09 min), DWI (*syngo* REVEAL) in the axial plane (ep2d_diff; TR 3000 ms, TE 88 ms, b-values 0, 500, 1000 mm/s^2, 3-scan trace, ADC map Inline, noise level set to 0, PAT factor 2 (*syngo* GRAPPA), FOV (200 x 200) mm^2, matrix (150 x 150) px^2, slice thickness 3.5 mm, no gap, 8 averages, acquisition time 2:57 min), thick-slice T2-weighted sequence in the axial plane covering lymph node stages from the renal veins down to the pubic bone (HASTE; TR 700 ms, TE 38 ms, PAT factor 2 (*syngo* GRAPPA), FOV

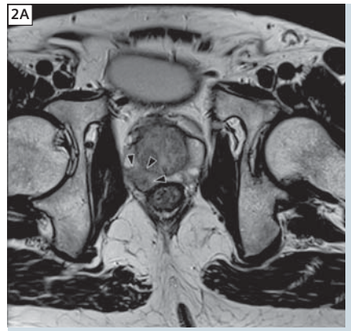

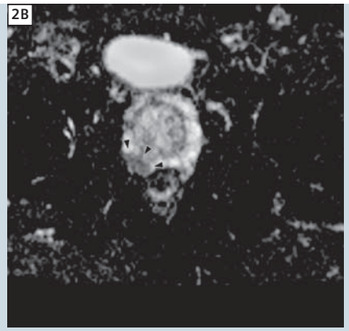

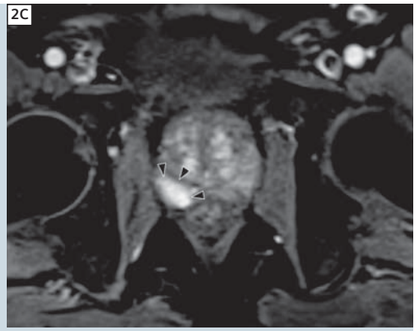

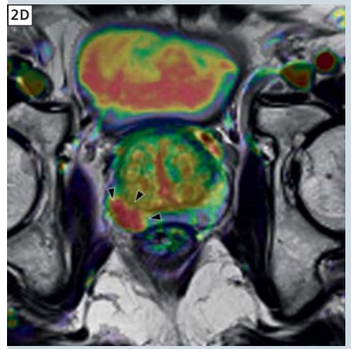

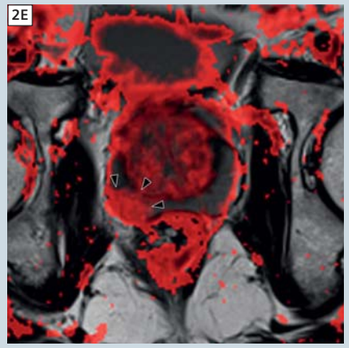

2A–G Prostate cancer with ex-vivo and pathologic correlation.
2A T2-weighted image
2B ADC map
2C Early arterial phase post-gadolinium
2D K_{trans} overlaid on T2w
2E ADC map overlaid on T2w

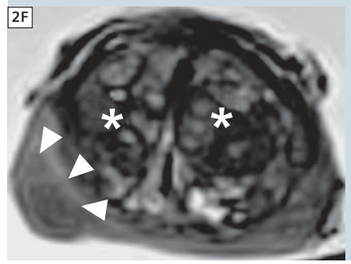

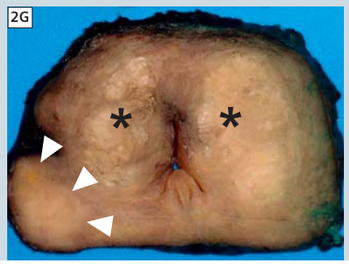

2F Ex-vivo prostatectomy specimen T2w MR
2G Whole-mount processing of a similar section as of MR imaging. The suspicious lesion (arrowheads) on the right middle-third peripheral zone is well depicted in all of the modalities, with good correlation to the pathological specimen.
* = Hyperplasia.

(350 x 317) mm^2, matrix (512 x 440) px^2 (interpolated), slice thickness 5 mm, 100% gap, 1 average, acquisition time 0:30 min), and DCE T1w images acquired with a 3D gradient echo (GRE) sequences (VIBE; TR 4.08 ms, TE 1.43 ms, PAT factor 2 (*syngo* GRAPPA), no fat saturation, FOV (280 x 280) mm^2, matrix (192 x 192) px^2, slice thickness 3 mm, 1 average, 40 measurements, 6.8 seconds per measurement, total acquisition time 4:33 min) (cubital intravenous application of 0.2 mmol/kg of gadolinium-chelate (DOTAREM, Guerbet, Aulnay-sous-Bois, France) on an MR-compatible power injector (Injektron 82 MRT, Medtron, Saarbrücken, Germany) between the second and third measurements). The whole examination took about 30 minutes.
Recently, we also added multi-flip angle volumetric T1w sequences (VIBE, same parameters as above, 1 measurement each, respectively 2°, 5°, 8° and 15° flip angle) prior to contrast injection, in order to estimate the T1 value, so as to enable accurate transfer constant (k_{trans}) calculation on DCE post-processed.
DCE images were post-proccessed using a work-in-progress package of the *syngo* Tissue 4D application. The *syngo* Tissue 4D applications allows pharmacokinetic modeling according to the Tofts-model including parameter calculations, namely transfer constant (k_{trans}), volume constant (Kep), extra-cellular volume of distribution (Ve) and integral area under the curve (iAUC). In addition, parametric color-maps can be generated and fused over MR morphology to allow accurate and fast assessment of the prostate parenchyma, and also to enable accurate measurements of pharmacokinetic parameters on suspected areas (Fig. 1). There is a built-in function to correct for movement between acquisition phases, which we use whenever required. The curve calculation is based on the placement of regions-of-interest (ROIs) (for evaluation of data, four ROIs were evaluated in our study: ROI 1: suspected lesion, ROI 2: contralateral peripheral zone, ROI 3: ipsillateral central gland, ROI 4: contralateral central gland). For calculation of parameters, the software requires input by the user; pre-evaluation parameters used in this study are as follow: noise level: 20, MR protocol: T1 and Dynamic, Contrast agent: Dotarem, volume: variable. The volume-of-interest (VOI) is defined by an elliptical area – drawn by the user – which encompasses the whole prostate volume. The parametric maps are generated from the full VOI, using the Tofts-model. For this, an arterial input function has to be selected; in most of our patients, a "slow" arterial input function has been chosen. K_{trans} and iAUC maps are saved as DICOM series, for further post-processing.
Post-processed images are afterwards overlaid on transverse T2w images, using *syngo* 3D-FUSION® (Siemens Healthcare, Erlangen, Germany), using PET-Rainbow and Descending Red Ramp color look-up tables, respectively for the k_{trans} and the ADC map.
For evaluation of findings within the study setting, one reader (LKB, 5 years of experience, 2 years on prostate MR) evaluated all of the examinations and imaging findings were registered on a dedicated evaluation sheet. Focused on the evaluation of capsular penetration of prostate cancer for planning of radical prostatectomy, suspected lesions were characterized by laterality (left x right x bilateral), presence of local extra-prostatic extension and seminal vesicle involvement. Prostatectomy specimens were submitted to routine histopathological evaluation, except for one, submitted to whole-mount processing.

Results

Prostatectomy showed prostate adenocarcinoma in all 13 cases, with Gleason grades varying between 6 (3+3) and 9 (4+5) (median 6).
In all 13 cases the main tumor focus was correctly identified by MR imaging. The laterality of the lesion was correctly determined by MR in 12 patients (sensitivity: 90%, specificity: 100%), eleven of which

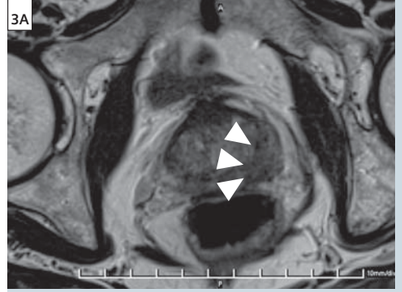

3A–E Extra-prostatic extension.
3A T2w image showing a nodular T2 hypointense area on the left base (arrowheads), focally bulging the capsular contour.

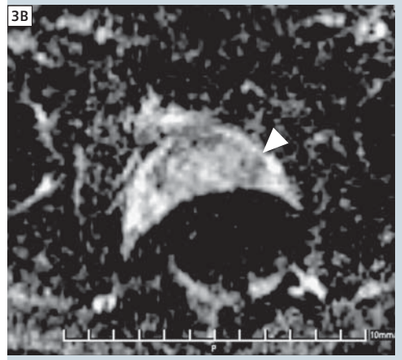

3B On the ADC map, there is restricted diffusion on the same spot, but further anatomical information.

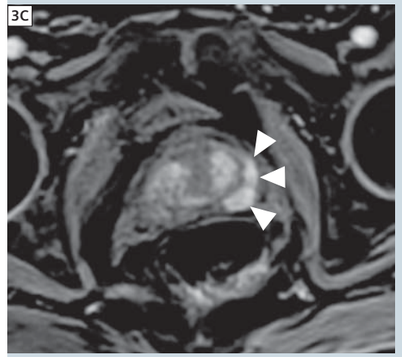

3C Early arterial phase post-gadolinium image, depicting intense and early enhancement on the suspicious area (arrowheads).

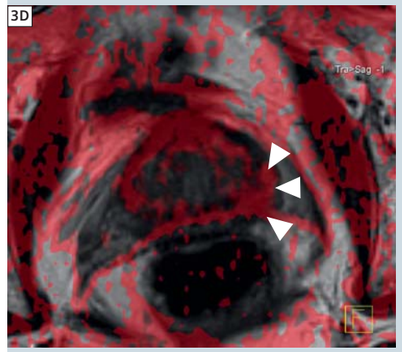

3D ADC map overlaid on T2w image, confirming good correlation with both anatomical and functional findings.

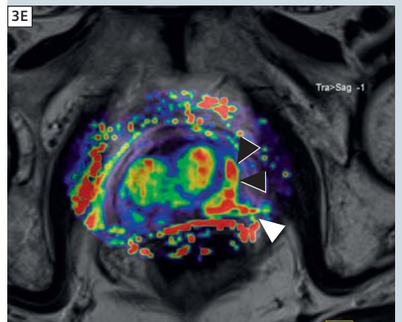

3E K_{trans} map overlaid on T2w image, showing that the focal permeability abnormalities (black arrowheads) extend outside the prostate contour (white arrowhead), strengthening the suspicion for extra-prostatic extension. This was the only sequence that depicted abnormal findings outside of the prostate parenchyma, showing the importance of multimodality imaging on the evaluation of prostate cancer.

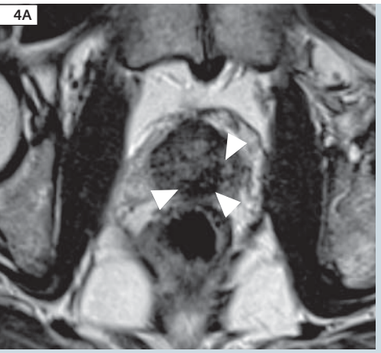

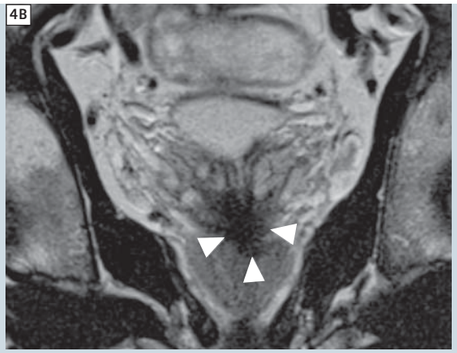

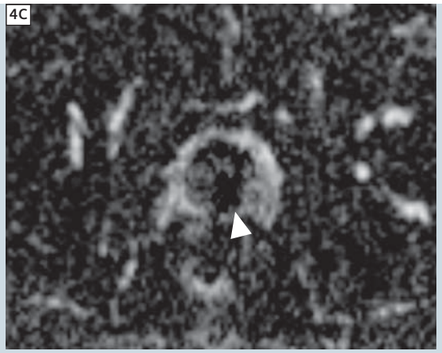

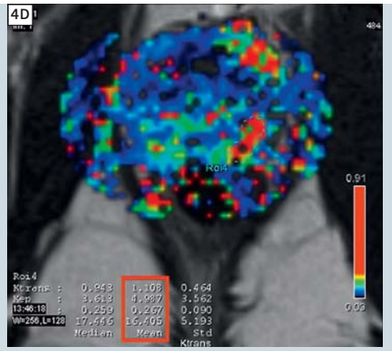

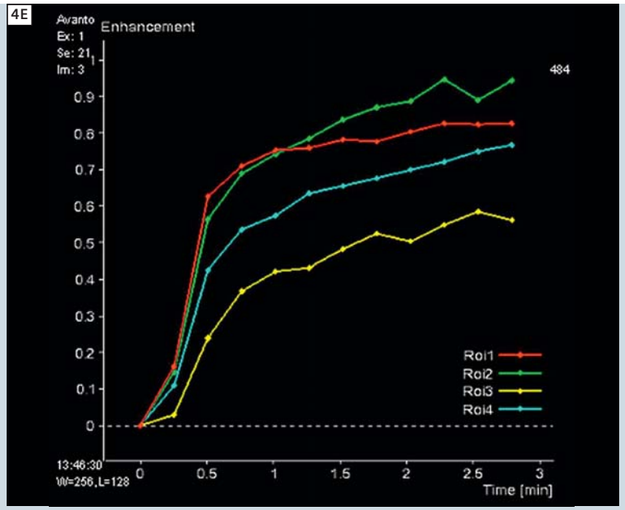

4A–E Seminal vesicle involvement.
4A Axial T2w image, showing a diffusely T2 hypointense prostate parenchyma, which lowers the accuracy for finding focal suspicious areas. There is although an overtly hypointense focus involving the proximal ejaculatory ducts (arrowheads), raising awareness for seminal vesicle extension.

4B Coronal T2w image, nicely showing the suspicious area, with clear involvement of both seminal vesicles.

4C ADC map, showing restricted diffusion on the same area.

4D K_{trans} map overlaid in T2w image, where a focal area of increased permeability (light-blue ROI) is seen, in keeping with the T2 hypointense lesion seen in **4A**, also showing quantitative data (red rectangle).

4E The lesion enhancement curve (red) is the steeper, with tendency to form a plateau rather than to keep on increasing.

had bilateral tumors. There was one false negative, in a patient with bilateral involvement substaged as unilateral tumor by MR.
Four patients had extra-prostatic tumoral extension, three of them being identified by MR imaging (sensitivity: 75%, specificity: 100%).
Only one patient had seminal vesicle tumoral invasion, also seen on MR imaging.
No patient had tumor-positive pelvic lymph nodes, neither was it suspected by MR in any of them.

Discussion

Functional prostate MR imaging, including DWI, DCE, and 3D multi-voxel spectroscopy, is largely turning into the mainstay in prostate cancer detection, staging and follow-up. The results among various institutions bear good to optimal correlation with histopathology, depending on the scanner's field strength (1.5T x 3.0T), the kind of coil employed (surface only x surface + endorectal), and also the gold standard utilized (biopsy x routine histopathology x whole-mount histopathology).
In this context, there's a tendency pointing towards studies on 3T prostate MR, with the combination of surface and endorectal coils, compared with whole-mount histopathology, in order to ally the most recent technology with the highest theoretical spatial resolution achievable. However, this approach creates a potential dilemma for health care providers, public health authorities and general radiology departments, considering that PCa is the most prevalent neoplasm in men, and the availability of 3T scanners worldwide still does not match the demand for diagnosis, staging and follow-up for this condition. Despite the most recent technological advances, an alternative should be pursued for MR imaging of PCa, that allies cost-effectiveness and scanner availability with acceptable diagnostic accuracy, in order to extend the benefits of the technique to the overall population, which is still being managed based on PSA and rectal exam alone.
Also, the endorectal coil (ERC) is another barrier to the acceptance of prostate MR. Although being of undisputedly better performance than surface coil alone on tumor localization, patient refusal due to cultural identity is still a major issue, most notably in Latin and Asian/Arabic countries. It requires specially trained personnel for proper placement, and considerably increases table time, not to mention the deformation produced on the prostate, that compromises radiotherapy planning and follow up studies. Particularly in Brazil, there is also an economical problem, for the ERC, which is disposable and for one use only, is not reimbursed by any of the health insurance companies or the public health system.
Giving those circumstances, and considering that our institutions are localized in a developing country, we initiated a long-term prospective research project aiming to create a prostate MR protocol that is feasible in most of the already worldwide installed 1.5T scanners, without the need of an endorectal coil or specially trained personnel, with optimized table time, and bearing acceptable diagnostic accuracy for relevant staging parameters, to be applied in large populational studies.
We also believe that newer post-processing tools for functional sequences, producing parametric color maps and fusions of functional and anatomic images, may further add to the diagnostic performance and to the communication of results to the referring physicians.
Preliminary results indicate a promising performance of this protocol on presurgical staging of PCa. Further patients will be included, and the upcoming results will be accordingly published.

References

1 Ross R, Harisinghani M. Prostate cancer imaging – what the urologic oncologist needs to know. Radiol Clin North Am 2006; 44:711-722, viii.
2 Somford DM, Futterer JJ, Hambrock T, Barentsz JO. Diffusion and perfusion MR imaging of the prostate. Magn Reson Imaging Clin N Am 2008; 16:685-695, ix.
3 Jung JA, Coakley FV, Vigneron DB, et al. Prostate depiction at endorectal MR spectroscopic imaging: investigation of a standardized evaluation system. Radiology 2004; 233:701-708.
4 Futterer JJ, Heijmink SW, Scheenen TW, et al. Prostate cancer localization with dynamic contrast-enhanced MR imaging and proton MR spectroscopic imaging. Radiology 2006; 241:449-458.
5 Bloch BN, Furman-Haran E, Helbich TH, et al. Prostate cancer: accurate determination of extracapsular extension with high-spatial-resolution dynamic contrast-enhanced and T2-weighted MR imaging – initial results. Radiology 2007; 245:176-185.
6 Weinreb JC, Blume JD, Coakley FV, et al. Prostate cancer: sextant localization at MR imaging and MR spectroscopic imaging before prostatectomy – results of ACRIN prospective multi-institutional clinicopathologic study. Radiology 2009; 251:122-133.
7 Langer DL, van der Kwast TH, Evans AJ, Plotkin A, Trachtenberg J, Wilson BC, Haider MA. Prostate tissue composition and MR measurements: investigating the relationships between ADC, T2, K(trans), v(e), and corresponding histologic features. Radiology. 2010 May;255(2): 485-94.
8 Turkbey B, Pinto PA, Mani H, Bernardo M, Pang Y, McKinney YL, Khurana K, Ravizzini GC, Albert PS, Merino MJ, Choyke PL. Prostate cancer: value of multiparametric MR imaging at 3 T for detection – histopathologic correlation. Radiology. 2010 Apr;255(1):89-99.
9 Groenendaal G, Moman MR, Korporaal JG, van Diest PJ, van Vulpen M, Philippens ME, van der Heide UA. Validation of functional imaging with pathology for tumor delineation in the prostate. Radiother Oncol. 2010 Feb;94(2):145-50.
10 Langer DL, van der Kwast TH, Evans AJ, Trachtenberg J, Wilson BC, Haider MA. Prostate cancer detection with multi-parametric MRI: logistic regression analysis of quantitative T2, diffusion-weighted imaging, and dynamic contrast-enhanced MRI. J Magn Reson Imaging. 2009 Aug;30(2):327-34.
11 Franiel T, Lüdemann L, Rudolph B, Rehbein H, Stephan C, Taupitz M, Beyersdorff D. Prostate MR imaging: tissue characterization with pharmacokinetic volume and blood flow parameters and correlation with histologic parameters. Radiology. 2009 Jul;252(1):101-8.
12 Ren J, Huan Y, Wang H, Ge Y, Chang Y, Yin H, Sun L. Seminal vesicle invasion in prostate cancer: prediction with combined T2-weighted and diffusion-weighted MR imaging. Eur Radiol. 2009 Oct;19(10):2481-6.
13 Fütterer JJ, Barentsz JO, Heijmink SW. Value of 3-T magnetic resonance imaging in local staging of prostate cancer. Top Magn Reson Imaging. 2008 Dec;19(6):285-9.
14 McMahon CJ, Bloch BN, Lenkinski RE, Rofsky NM. Dynamic contrast-enhanced MR imaging in the evaluation of patients with prostate cancer. Magn Reson Imaging Clin N Am. 2009 May;17(2):363-83.

Contact
Thomas Doering
Medical Physicist MRI, MSc
Post-processing Laboratory
CDPI & Multi-imagem
Rio de Janeiro
Brazil
Tel. +55 21 2432 9194
thomas.doring@gmail.com

L. Kayat Bittencourt, M.D.
CDPI & Multi-Imagem
Rio de Janeiro
Brazil
lkayat@gmail.com

Siemens Healthcare Publications

Our publications offer the latest information and background for every healthcare field. From the hospital director to the radiological assistant – here, you can quickly find information relevant to your needs.

Medical Solutions
Innovations and trends in healthcare. The magazine is designed especially for members of hospital management, administration personnel, and heads of medical departments.

eNews
Register for the global Siemens Healthcare Newsletter at www.siemens.com/healthcare-eNews to receive monthly updates on topics that interest you.

AXIOM Innovations
Everything from the worlds of interventional radiology, cardiology, fluoroscopy, and radiography. This semiannual magazine is primarily designed for physicians, physicists, researchers, and medical technical personnel.

MAGNETOM Flash
Everything from the world of magnetic resonance imaging. The magazine presents case reports, technology, product news, and application tips. It is primarily designed for physicians, physicists, and medical technical personnel.

SOMATOM Sessions
Everything from the world of computed tomography. With its innovations, clinical applications, and visions, this semiannual magazine is primarily designed for physicians, physicists, researchers, and medical technical personnel.

For current and past issues and to order the magazines, please visit **www.siemens.com/healthcare-magazine.**

Market your MAGNETOM system

All the tools necessary to market your facility to patients and referring physicians are waiting for you in the **Your MAGNETOM** section on **www.siemens.com/magnetom-world**

Here you will find everything you need from patient pamphlets to advertisements, to trailers and press releases, postcards, posters, event checklists, high-resolution images and much more – ready for immediate use.

MAGNETOM Flash – Imprint

Publisher:
Siemens AG
Medical Solutions
Business Unit Magnetic Resonance,
Karl-Schall-Straße 6, D-91052 Erlangen, Germany

Editor-in-Chief: Dr. Matthias Lichy, M.D. (matthias.lichy@siemens.com)

Associate Editor: Antje Hellwich (antje.hellwich@siemens.com)

Editorial Board: Ph.D.; Okan Ekinci, M.D.; Ignacio Vallines, Ph.D.; Wellesley Were; Milind Dhamankar, M.D.; Michelle Kessler; Gary McNeal; Sunil Kumar, M.D.

Production: Norbert Moser, Siemens AG, Medical Solutions

Layout: independent Medien-Design Widenmayerstrasse 16, D-80538 Munich

Printers: Farbendruck Hofmann, Gewerbestraße 5, D-90579 Langenzenn, Printed in Germany

MAGNETOM Flash is also available on the internet:
www.siemens.com/magnetom-world

MAGNETOM Flash

The Magazine of MR

Issue Number 2/2010
CMR Edition
Not for distribution in the US.

SIEMENS

Please enter your business address

Institution

Department

Function

Title

Name

Street

Postal Code

City

State

Country

MR system used

Please include me in your mailing list for the following Siemens Healthcare customer magazine(s):

☐ Medical Solutions

☐ MAGNETOM Flash

☐ SOMATOM Sessions

☐ AXIOM Innovations

Stay up to date with the latest information Register for:

☐ the monthly e-Newsletter

E-mail

☐ Yes, I consent to the above information being used for future contact regarding product updates and other important news from Siemens.

☐ unsubscribe from info service

Please print clearly!

MAGNETOM Flash

Siemens AG
Medical Solutions
Magnetic Resonance
Antje Hellwich - Marketing
P.O. Box 32 60
D-91050 Erlangen
Germany

→ Visit www.siemens.com/magnetom-world for case reports, clinical methods, application tips, talks and much more clinical information.

SUBSCRIBE NOW!

– and get your free copy of future MAGNETOM Flash! Interesting information from the world of magnetic resonance – gratis to your desk. Send us this postcard, or subscribe online at www.siemens.com/MAGNETOM-World

Global Siemens Headquarters

Siemens AG
Wittelsbacherplatz 2
80333 Muenchen
Germany

Global Siemens Healthcare Headquarters

Siemens AG
Healthcare Sector
Henkestr. 127
91052 Erlangen
Germany
Phone: +49 9131 84-0
www.siemens.com/healthcare

www.siemens.com/healthcare-magazine

Order No. A91MR-1000-75C-7600 | Printed in Germany | CC MR 01000 ZS 101015. | © 10.10, Siemens AG

On account of certain regional limitations of sales rights and service availability, we cannot guarantee that all products included in this brochure are available through the Siemens sales organization worldwide. Availability and packaging may vary by country and is subject to change without prior notice. Some/All of the features and products described herein may not be available in the United States.

The information in this document contains general technical descriptions of specifications and options as well as standard and optional features which do not always have to be present in individual cases.

Siemens reserves the right to modify the design, packaging, specifications and options described herein without prior notice.
Please contact your local Siemens sales representative for the most current information.

Note: Any technical data contained in this document may vary within defined tolerances. Original images always lose a certain amount of detail when reproduced.

Global Business Unit

Siemens AG
Medical Solutions
Magnetic Resonance
Henkestr. 127
DE-91052 Erlangen
Germany
Phone: +49 9131 84-0
www.siemens.com/healthcare

Local Contact Information

In Asia
Siemens Pte Ltd
The Siemens Center
60 MacPherson Road
Singapore 348615
Phone: +65 6490-8096

In Canada
Siemens Canada Limited
Medical Solutions
2185 Derry Road West
Mississauga ON L5N 7A6
Canada
Phone: +1 905 819-5800

Europe/Africa/Middle East
Siemens AG
Medical Solutions
Henkestr. 127
91052 Erlangen
Germany
Phone: +49 9131 84-0

Latin America
Siemens S.A.
Medical Solutions
Avenida de Pte. Julio A. Roca No 516,
Piso 7
C1067ABN Buenos Aires
Argentina
Phone: +54 11 4340-8400

USA:
Siemens Medical Solutions U.S.A., Inc.
51 Valley Stream Parkway
Malvern, PA 19355-1406
USA
Phone: +1-888-826-9702